eXPRESS Polymer Letters Vol.5, No.8 (2011) 661
Available online at www.expresspolymlett.com
DOI: 10.3144/expresspolymlett.2011.64

Editorial corner – a personal view
Is there any chance for polypropylene/clay nanocomposites in injection molding?

P. M. Frontini[1*], *A. S. Pouzada*[2]

[1]Instituto en Ciencia y Tecnología de Materiales (INTEMA), CONICET, Universidad Nacional de Mar del Plata, Juan B. Justo 4302, B7608FDQ, Mar del Plata, Argentina
[2]Institute for Polymers and Composites/I3N, University of Minho, Campus de Azurem, Guimarães, Portugal

The possibility of manufacturing nano-composites materials with tailored properties at low cost has gained much interest. In fact, there is already more than two decades of research on those materials. Particular interest has been paid to clay nano-platelets and their composites with non-polar thermoplastic polyolefin matrixes, namely polypropylene (PP).

Imagine an industrialist and his design team relatively aware of the developments in the research with nano-fillers asking themselves: What can we do with nano-composites and make a net profit up to the 'promises' of the current state of the art? Research announced potential areas of interest for practical applications include mechanical performance, toughness improvement, surface hardening, fire retardancy, or, solvent and permeability reduction. However there remains the problem of how a company could set up the facility for compounding, and guarantee proper dispersion and minimization of health hazards. One should bear in mind that for industrial dissemination conventional equipments should be used and compounding achieved through in-line mixing of virgin resins and nanoclay masterbatches.

Since the seventies polypropylene has been seen as the wonder engineering-commodity material with widespread application in numerous technical applications. Current masterbatches are mainly based on thermoplastic polyolefins and anhydride functionalized PP as a compatibilizer. In principle, filling with a low incorporation level of nanoclay (typically less than 5%), makes PP adequate to applications with engineering requirements. Nevertheless, only well-dispersed and well-exfoliated nanoparticles can lead to the expected improvement of properties. The nanoparticle dispersion and exfoliation is usually assumed to be achieved during masterbatching, but the suppliers of masterbatches request a relatively high price. Tests at the industrial scale are reported with typical processing setup using PP mixed with nanoclay masterbatches. The results showed only minute improvements on stiffness. Conversely, the toughness was affected particularly in weld-line regions, and the surface tribological properties were not improved. Underlining these evidences poor exfoliation was a common feature in moldings obtained using industry achievable processing conditions.

There is an evident interest of bringing the benefits of nanocomposites at the laboratory scale to cost competitive industrial products. However the first available information leaves a number of treads that research could well follow, for example. Which level of exfoliation should be required to viable masterbatches? Is there any scope for hybrid compounding, i.e. combining particulate nanoclays with fibre reinforcements? Are there only a few niches of application for nanocomposites? Have nanofillers any chance of being full exfoliated within non polar matrixes? Do these nanocomposites will require alternative routes of processing? Should novel compatibilizers be developed in order to avoid unavoidable re-agglomeration during injection molding?

*Corresponding author, e-mail: pmfronti@fi.mdp.edu.ar

eXPRESS Polymer Letters Vol.5, No.8 (2011) 662–673
Available online at www.expresspolymlett.com
DOI: 10.3144/expresspolymlett.2011.65

Poly(L-lactide) nanocomposites containing octaglycidylether polyhedral oligomeric silsesquioxane: Preparation, structure and properties

J. Zou[1,2], *X. Chen*[1], *X. B. Jiang*[1], *J. Zhang*[1], *Y. B. Guo*[1], *F. R. Huang*[1*]

[1]China Key Laboratory for Specially Functional Polymeric Materials and Related Technology of the Ministry of Education, School of Materials Science and Engineering, East China University of Science and Technology, Shanghai 200237, PR China
[2]School of Materials Science and Engineering, Jiangsu University of Science and Technology, Zhenjiang, Jiangsu 212003, PR China

Received 13 November 2010; accepted in revised form 25 January 2011

Abstract. Poly(L-lactide)s (PLLA) tethered with octaglycidylether polyhedral oligomeric silsesquioxane (OPOSS) with contents of 0.02–1.00 mol% were successfully prepared by solution ring-opening polymerization of L-lactide in the presence of $Sn(Oct)_2$ catalyst. Fourier transform infrared (FTIR) and proton nuclear magnetic resonance ^{1}H-NMR spectroscopic techniques confirm the formation of secondary hydroxyls due to the reaction between PLLA main chains and OPOSS cages. X-ray analyses prove that the presence of OPOSS does not alter the packing structure of PLLA chain in the crystals but enhances the crystallinity of PLLA hybrids. PLLA/PLLA-OPOSS nanocomposites with PLLA-OPOSS contents of 1–30 wt% were prepared by solution-mixing of the neat PLLA polymer with various contents of the PLLA-OPOSS hybrid with 0.50 mol% OPOSS. It is found that the glass transition temperature of the PLLA/PLLA-OPOSS nanocomposites remains the same as that of pristine PLLA and the thermooxidative stability of the nanocomposites is improved with the PLLA-OPOSS content of 1–20 wt%, as compared to that of the neat PLLA polymer. PLLA/PLLA-OPOSS nanocomposites, except for PLLA/PLLA-OPOSS[1], has higher crystallization rate at 120°C. The nucleation density increases with increase in the content of PLLA-OPOSS.

Keywords: *nanocomposites, poly(L-lactide), octaglycidylether POSS, hybrid PLLA*

1. Introduction

Recently, people have paid much attention to polylactide (PLLA) from annually renewable resources due to its good biodegradability, high mechanical strength, excellent shaping and molding properties [1–4]. However, PLLA exhibits some disadvantages, such as low thermooxidative stability and slow crystallization rate, which greatly limit its application. Therefore, several methods, including blending with other polymers, copolymerization with other monomers, have usually been used to control the properties of PLLA [5–8]. The addition of nanoparticles such as nanoclay and carbon nanotubes into PLLA is also an attractive way to improve the performance of PLLA [9–14].

As for nanoparticles, more and more attention has been paid to polyhedral oligomeric silsesquioxanes (POSS) due to their inorganic-organic hybrid nature in the last decade [15–19]. POSS molecules possess a cage-like siloxane structure with a size ranging from 1 to 3 nm and are surrounded by eight R groups ($RSiO_{1.5}$), where R can be various types of organic groups, one or more of which is reactive or polymerizable [20]. POSS molecules can be easily

*Corresponding author, e-mail: fhuanglab@ecust.edu.cn

incorporated into polymer systems through blending, grafting or copolymerization [15, 16]. For example, several polymers, such as HDPE [21], PP [22], epoxy [23–26], PMMA [27–30], PU [31, 32], PET [33–35] and PC [36], have been blended with POSS. It has been reported that PLLA/POSS nanocomposites have enhanced crystallization rate, improved mechanical properties and accelerated hydrolytic degradation as compared with pristine PLLA [19]. PLLA-POSS hybrids were synthesized via the ring-opening polymerization of L-lactide with 3-hydroxypropylheptaisobutyl POSS. Then PLLA/PLLA-POSS nanocomposites were made by blending PLLA with PLLA-POSS hybrids in solution and had exhibited improved thermal and thermooxidive degradation properties, high crystallization rates and crystallinities [37].

In this work, PLLA-OPOSS hybrids are synthesized by solution ring-opening polymerization of L-lactide with octaglycidylether POSS as an initiator in the presence of a stannous (II) octoate [$Sn(Oct)_2$] catalyst. PLLA-OPOSS hybrids are introduced into neat PLLA to prepare PLLA/PLLA-OPOSS nanocomposites. The structure of the synthesized PLLA-OPOSS hybrids are characterized by Fourier transform infrared spectroscopy (FTIR), ^{1}H nuclear magnetic resonance spectroscopy (^{1}H-NMR), and X-ray diffraction analysis. The thermooxidative stability, isothermal crystallization behavior and the spherulitic morphology of the PLLA/PLLA-OPOSS nanocomposites are investigated by thermogravimetric analysis (TGA), differential scanning calorimetry (DSC), optical polarimetry and polarizing optical microscope, respectively.

2. Experimental

2.1. Materials

L-lactide (99.8%, prepared by our laboratory) was used as the monomer for solution ring-opening polymerization. Octaglycidylether POSS (Product name: OPOSS) was purchased from Hybrid Plastics Inc, USA. $Sn(Oct)_2$ (Sigma-Aldrich, USA) was adopted as a catalyst for the solution ring-opening polymerization of L-lactide. PLLA (trade name 4032D, number-average molecular weight (M_n) $3 \cdot 10^4$ g/mol) was purchased from Nature Works Co. Ltd., USA.

2.2. Synthesis of PLLA-OPOSS hybrids

Octaglycidylether POSS (0.02–1.00 mol%) and L-lactide were dissolved into xylene in a flask and heated to 130°C under an atmosphere of dry nitrogen, and then 0.1 wt% $Sn(Oct)_2$ as catalyst was added into the flask. The mixtures were magnetically stirred at 130°C for 8 h, then precipitated into excess methanol, and filtrated. The overall reaction scheme is shown in Figure 1. The final products were purified by dissolving in chloroform and precipitating in methanol. Finally, the products were dried in vacuo at 50°C for 24 h. The products are named PLLA-OPOSSx hybrids, where the subscript·denotes the molar percentage of OPOSS to L-lactide.

2.3. Preparation of PLLA/PLLA-OPOSS nanocomposites

For the preparation of PLLA/PLLA-OPOSS nanocomposites, the mixture (3 g) of PLLA and PLLA-OPOSS0.50 hybrid was dissolved in chloroform with vigorous stirring. The content of 1–30 wt%

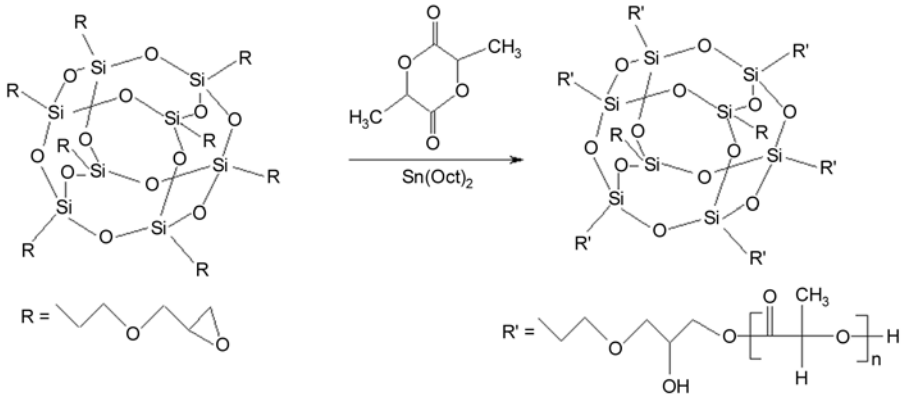

Figure 1. Scheme for synthesis of PLLA-OPOSS hybrids

PLLA-OPOSS$_{0.50}$ hybrids were adopted for the PLLA/PLLA-OPOSS nanocomposites. The mixed solutions were poured into excess methanol, and the precipitates were filtered. Then, the PLLA/PLLA-OPOSS filtrates were dried *in vacuo* at 50°C for 24 h. The nanocomposites are named PLLA/PLLA-OPOSS^y, where y represents the weight percentage of PLLA-OPOSS$_{0.50}$.

2.4. Testing and characterization

The ^{1}H-NMR measurements were carried out on a 400 MHz NMR spectrometer (Bruker AVANCE II, Switzerland) for characterization of chemical structures and composition of the PLLA-OPOSS hybrids. The samples were dissolved in $CDCl_3$ and ^{1}H-NMR spectra were obtained with tetramethylsilane (TMS) as the internal reference.

The FTIR measurements were conducted on a FTS 2000 (DIGILAB, America) at room temperature (25°C). Optical-grade KBr was grounded in a mortar with a pestle, and enough solid sample (1 wt%) was grounded into KBr to make KBr pellets. After the pellets were loaded, a minimum of 16 scans was collected for each sample at a resolution of ±4 cm^{-1}.

The X-ray diffraction analysis was obtained with XRD-6000 (Shimadzu Co., Japan) (Ni-filtered Cu K_α radiation, 40 kV and 200 mA) over the 2θ range of 5–40° at a scanning rate of 4.0°/min.

A thermal gravimetric analyzer (Pyris Diamond Perkin Elmer, America) was used to investigate the thermooxidative stability of the PLLA/PLLA-OPOSS nanocomposites. The samples were heated from room temperature to 600°C at a heating rate of 10°C/min under air atmosphere.

The thermal properties of the PLLA/PLLA-OPOSS nanocomposites were characterized by DSC (DSC 204F1, NETZSCH, Germany). The samples were heated to 220°C at a heating rate of 10°C/min (first run) under nitrogen , held for 3 min, cooled to room temperature at 40°C/min, and then heated to 220°C again at 10°C/min (second run). The glass transition temperature, cold crystallization peak temperature, and melting temperature of neat PLLA and PLLA/PLLA-OPOSS nanocomposites were obtained from the second heating run.

The testing of crystallization rate was investigated by the optical polarimetry (GLY-III) made by Donghua University at Shanghai in China. The samples were melted to press into films between two glass slides at 200°C, subsequently put into a crystallization room, and then the curves of crystallization rate were recorded when the temperature of the crystallization room was constant.

Polarized optical microscopy images of the melt blended samples were obtained by using an XPR-500C (Shanghai Caikang Optical Instrument Co. Ltd., China) polarizing microscope equipped with a video camera and a heat stage. The samples were prepared by melting the blended composites on a hot plate at 200°C for 3 minutes, pressing them between two cover slips, and then rapidly cooling them to 125°C.

3. Results and discussion

3.1. Formation of PLLA-OPOSS hybrids

The FTIR spectra of the octaglycidylether POSS, PLLA-OPOSS$_{0.50}$ hybrids, and the neat PLLA polymer are shown in Figure 2. In the spectrum of octaglycidylether POSS, the stretching vibration bands at 1088 and 906 cm^{-1} are assigned to the Si–O–Si moiety and epoxide groups, respectively. In the spectrum of the neat PLLA, the carbonyl band appears around 1760 cm^{-1} and the hydroxyl stretching vibration band around 3434 cm^{-1}. Under the same condition, it is seen that the band of epoxide groups at 915 cm^{-1} nearly disappears in the spectrum of PLLA-OPOSS, indicating that the reaction between PLLA and OPOSS has successfully happened. Meanwhile, it is interesting to find that the stretching vibration band of hydroxyl shifts to the higher frequency (viz. 3512 cm^{-1}) as compared with that of PLLA (at 3434 cm^{-1}) with the reaction occurring. The results indicate that the reaction

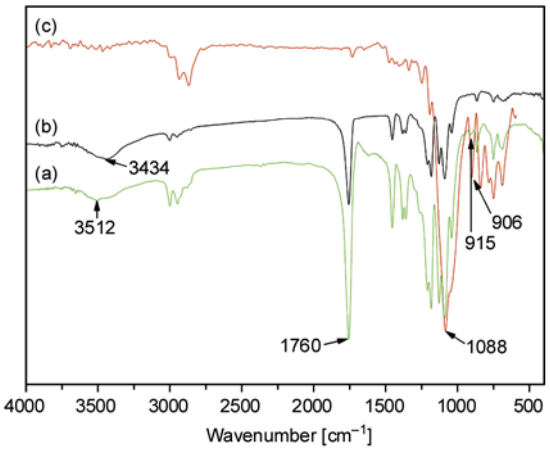

Figure 2. FTIR spectrum of (a) PLLA-OPOSS, (b) PLLA and (c) OPOSS

occurs between PLLA and OPOSS, which results in the formation of secondary alcohol hydroxyls.

In order to further examine the structure and composition of PLLA-OPOSS hybrids, nuclear magnetic resonance spectroscopy (^{1}H-NMR) measurement was performed on OPOSS and PLLA-OPOSS hybrids. The ^{1}H-NMR spectra of OPOSS and PLLA-OPOSS hybrids together with the assignment of the spectra are shown in Figure 3. OPOSS (chloroform-d, ppm): 0.64 (2.01H, Si**C**$\mathbf{H_2}$$CH_2CH_2O$), 2.61 and 2.79 (2.03H, O**C**$\mathbf{H_2}$CH epoxide), 3.15 (1.00H, OCH_2**CH** epoxide), 3.34–3.73 (4.3H, $SiCH_2CH_2$**C**$\mathbf{H_2}$O and $SiCH_2CH_2CH_2$O**C**$\mathbf{H_2}$). PLLA-OPOSS (chloroform-d, ppm): 0.64 (3.5H, Si**C**$\mathbf{H_2}$$CH_2CH_2$–O), 1.49 (3.5H, $SiCH_2$**C**$\mathbf{H_2}$$CH_2$O), 1.50–1.60 (75H, methyl on PLLA), 2.09 (0.75H, OH), 2.61 and 2.80 (2.00H, O**C**$\mathbf{H_2}$CH epoxide), 3.15 (1.00H, OCH_2**CH** epoxide), 3.36–3.75 (8.5H, $SiCH_2CH_2$**C**$\mathbf{H_2}$O, $SiCH_2CH_2CH_2$ O**C**$\mathbf{H_2}$), 4.34–4.38 (1.00H, O**C**$\mathbf{H_2}$ $CH(CH_2)$ OH), 5.15–5.20 (25H, methylidyne on PLLA). The resonance signals which appeared in 0.64, 2.61, 2.80 and 3.36–3.75 ppm are assignable to the protons of glycidylether groups of the OPOSS cages; the resonance signals in 1.50–1.60 and 5.15–5.20 ppm are assignable to the protons of methyl and methylidyne in PLLA, respectively. The integration intensity ratio of the peak for methyl to that for methylidyne in PLLA is 3:1, which corresponds with the structure of PLLA. Moreover, we can note the presence of a characteristic signal of a methylidyne proton in 4.34–4.38 ppm (signal g in Figure 3), which could be ascribed to the reaction product of epoxy of OPOSS and carboxyl of PLLA. Therefore, OPOSS is tethered with PLLA successfully. However, there is some residual methylidyne of OPOSS, which appears at 3.15 ppm (signal e in Figure 3b). In addition, the ratio of integration intensity of peak at

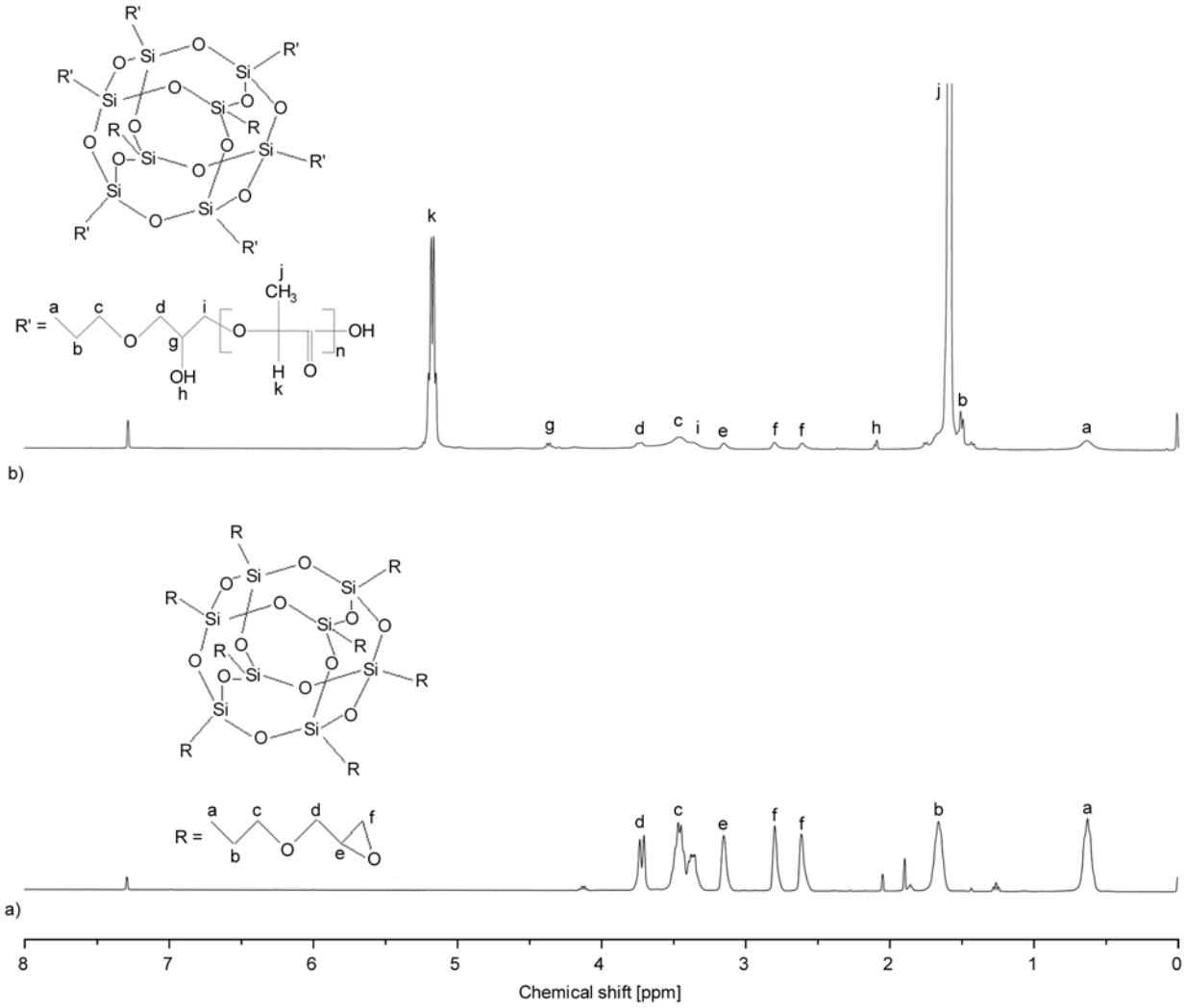

Figure 3. ^{1}H-NMR spectra of (a) OPOSS, (b) PLLA-$OPOSS_{0.50}$ hybrid

0.64 ppm to those of peaks in 4.34–4.38 ppm is 3.5, which is higher than 2. Therefore, not all octaglycidylether groups participate in the reaction with PLLA.

The molecular weight of the PLLA-OPOSS hybrid is determined using ^{1}H-NMR and calculated by the Equation (1):

$$M_{n_{PLLA-OPOSS}} = M_{n_{OPOSS}} + 72 \cdot \frac{\frac{k}{a}}{16} \quad (1)$$

where k and a represent the area of the ^{1}H-NMR signal of PLLA methine hydrogen in 5.15–5.20 ppm and that of OPOSS methylene hydrogen at 0.64 ppm, respectively. The value of 72 is the molecular mass of the repeating units of PLLA [38]. The molecular weight of the PLLA-OPOSS$_{0.50}$ calculated by ^{1}H-NMR is 9178 g/mol.

Figure 4 shows the X-ray diffraction patterns of neat PLLA and PLLA-OPOSS hybrids. All spectra of the PLLA-OPOSS hybrids reveal diffraction peaks at 14.8, 16.8, 19.1, and 22.4°, which are consistent with the peaks of neat PLLA polymer reported by Xu *et al.* [39]. This observation indicates that there is little change in the crystalline structure for the PLLA-OPOSS. Hence, the presence of OPOSS does not alter the packing structure of PLLA chain in the crystals. Moreover, the intensity of the diffraction peaks of PLLA-OPOSS hybrids become stronger than those of neat PLLA, which indicates that the existence of OPOSS may enhance the crystallinity of PLLA. However, the intensity of the diffraction peaks of PLLA decreases with increasing the content of OPOSS, which may be caused by the cage structure of OPOSS which hinders the crystallization.

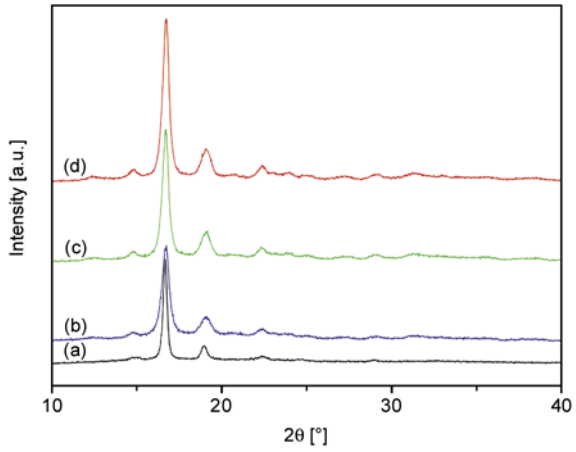

Figure 4. The X-ray diffraction patterns for: (a) neat PLLA and PLLA-OPOSS hybrids of various concentrations (b) 0.50 mol%, (c) 0.10 mol%, (d) 0.02 mol%

3.2. Thermal properties of PLLA/PLLAĪOPOSS nanocomposites

A series of PLLA/PLLA-OPOSS nanocomposites were prepared by solution blending of neat PLLA polymer with 1–30 wt% PLLA-OPOSS$_{0.50}$ hybrids. The TGA curves of the neat PLLA and PLLA/PLLA-OPOSS nanocomposites in air atmosphere are displayed in Figure 5. The thermooxidative decomposition temperatures for 5 and 50% weight loss ($T_{0.05}$ and $T_{0.50}$) are evaluated from the TGA curves, as listed in Table 1. All the samples display similar degradation profiles within the experimental temperature range, indicating that the presence of OPOSS does not significantly alter the degradation mechanism of PLLA matrix. $T_{0.05}$ and $T_{0.50}$ of neat PLLA are about 286 and 346°C, respectively. It is seen that $T_{0.05}$ and $T_{0.50}$ of the PLLA/PLLA-OPOSS nanocomposites with PLLA-OPOSS content of 1–20 wt% are higher than those of neat PLLA and tend to increase with increasing the content of PLLA-OPOSS hybrids. This improvement in the thermooxidative stability could be ascribed to the well-dispersed POSS cubes in nanocomposites and the

Table 1. Thermooxidative degradation temperatures of PLLA/PLLA-OPOSS nanocomposites under air

Sample code	Air condition	
	$T_{0.05}$ [°C]	$T_{0.50}$ [°C]
Neat PLLA	286	346
PLLA/PLLA-OPOSS^1	291	352
PLLA/PLLA-OPOSS^5	299	354
PLLA/PLLA-OPOSS^{10}	305	354
PLLA/PLLA-OPOSS^{20}	306	356
PLLA/PLLA-OPOSS^{30}	283	338

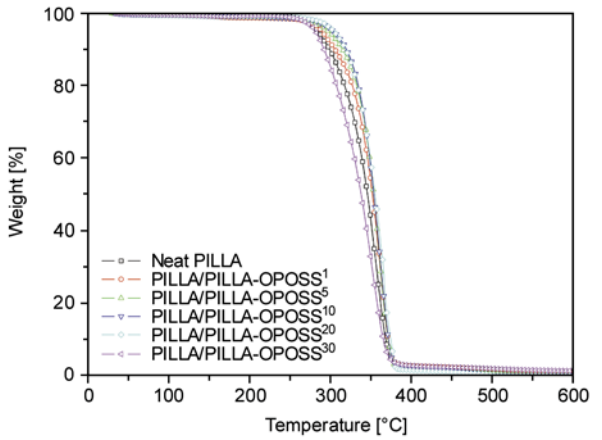

Figure 5. TGA curves of the neat PLLA and PLLA/PLLA-OPOSS nanocomposites test under air

formation barrier of silica layer during the decomposition, which prevents PLLA from further degradation.

However, $T_{0.05}$ and $T_{0.50}$ of PLLA/PLLA-OPOSS$_{0.5}^{30}$ are slightly lower than those of neat PLLA. It is due to the fact that PLLA-OPOSS with low molecular weight compared to the neat PLLA matrix results in low thermooxidative stability of the nanocomposites. In this situation, the lower molecular weight effect of PLLA-OPOSS became dominant over the reinforcing effect of the OPOSS molecules for the nanocomposites with high PLLA-OPOSS content of 30 wt%.

Figure 6 displays the DSC thermograms of the neat PLLA polymer and PLLA/PLLA-OPOSS nanocomposites with various PLLA-OPOSS$_{0.50}$ hybrid content of 1–30 wt%. The cold-crystallization temperatures of PLLA/PLLA-OPOSS nanocomposites shifts to higher temperatures compared to the neat PLLA. Moreover, the crystallization exothermic peak area becomes higher than that of the neat PLLA. This suggested that the crystallization rates of the nanocomposites is higher than the neat PLLA because of the heterogeneous nucleation effect of the OPOSS molecules dispersed uniformly in the PLLA matrix. On the other side, the glass transition temperature of the PLLA/PLLA-OPOSS nanocomposites remains consistent with the neat PLLA, regardless of the PLLA-OPOSS content, as summarized in Table 2. In addition, for all of the neat PLLA and PLLA/PLLA-OPOSS nanocomposites appear two melting peaks, as shown in Figure 6. The low-temperature melting peak results from melting of defective crystalline grains and the high-temperature melting peak due to melting of crystalline grains with relatively perfect structure. The melting temperature (T_m) of the PLLA/PLLA-OPOSS nanocomposites decreases with increasing PLLA-OPOSS hybrid content because of plasticity of the lower molecular weight of the PLLA-OPOSS hybrid in the PLLA matrix. In addition, the melting temperature of the PLLA/PLLA-OPOSS nanocomposites with PLLA-OPOSS hybrid content of 1–10 wt% is higher than that of the neat PLLA due to the cage structure of OPOSS, whereas the low molecular weight of PLLA-OPOSS effect becomes dominant when PLLA-OPOSS hybrid content arrives at the range of 20–30 wt%.

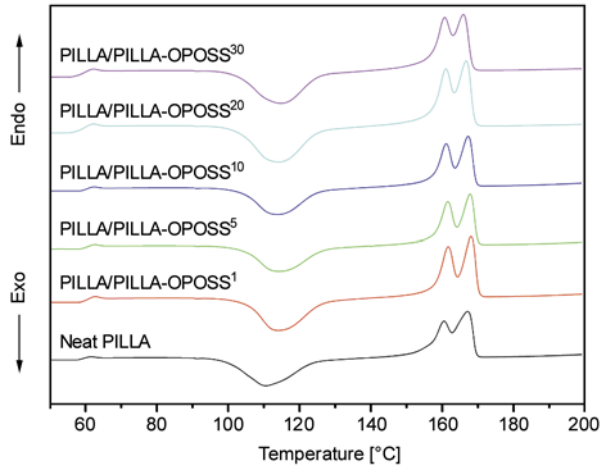

Figure 6. The DSC thermographs(second run)of neat PLLA homopolymer and PLLA/PLLA-OPOSS nanocomposites

3.3. Dynamic isothermal crystallization

In order to understand the effect of the addition of PLLA-OPOSS hybrids on the crystallization rate of PLLA, isothermal crystallization behavior of PLLA/PLLA-OPOSS nanocomposites were investigated by the optical polarimetry (GLY-III) tester. The transmitted light intensity increases with the increasing of crystallinity and finally levels off when crystallization completes. As an index of crystallinity, $(I_t - I_0)/(I_\infty - I_0)$ is used to define the relative light intensity, where I_t and I_0 are the I value at time $t_c = t$ and 0, respectively, I_∞ is the I value when it levels off. Figure 7 shows the typical $(I_t - I_0)/(I_\infty - I_0)$ changes with t_c for PLLA/PLLA-OPOSS^{30} films, where the starting, half, and ending times for overall PLLA/PLLA-OPOSS^{30} crystallization [t_c(S), t_c(1/2), and t_c(E), respectively] are

Table 2. Thermal transition properties (second run) of neat PLLA and PLLA/PLLA-OPOSS nanocomposites

Sample code	T_g [°C]	T_{cc} [°C]	ΔH_{cc} [J/g]	T_m [°C]		ΔH_m [J/g]
				T_{m1}	T_{m2}	
Neat PLLA	59.8	110.5	38.1	160.5	167.2	42.9
PLLA/PLLA-OPOSS^1	60.7	114.0	40.0	161.7	168.2	42.1
PLLA/PLLA-OPOSS^5	60.7	114.0	39.5	161.6	167.8	40.4
PLLA/PLLA-OPOSS^{10}	60.7	113.7	38.1	161.0	167.3	41.2
PLLA/PLLA-OPOSS^{20}	59.5	114.1	38.8	161.0	166.7	42.5
PLLA/PLLA-OPOSS^{30}	59.6	114.8	39.3	160.7	165.9	40.7

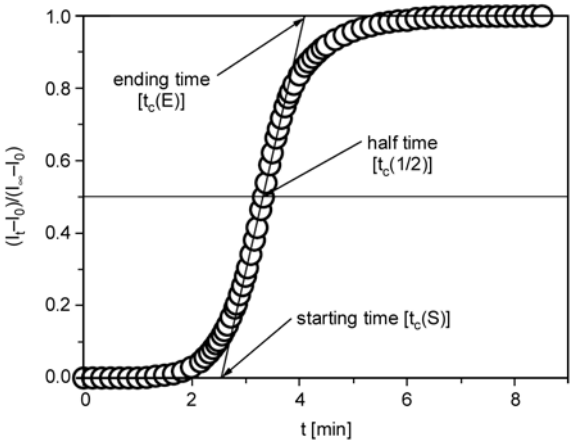

Figure 7. Typical $(I_t - I_0)/(I_\infty - I_0)$ change with for PLLA/PLLA-OPOSS^{30} film at 110°C

defined. Figure 8 plotted the evaluated t_c(S), t_c(1/2), and t_c(E) as a function of T_c. As shown in Figure 8, the t_c(S), t_c(1/2), and t_c(E) of PLLA/PLLA-OPOSS nanocomposites with 1–30 wt% of PLLA-OPOSS$_{0.5}$ were shorter than or close to those of neat PLLA film. The short t_c(S), t_c(1/2), and t_c(E) as observed are caused by PLLA-OPOSS which acts as a heterogeneous nucleation agent for the crystallization of PLLA. Compared with the crystallization temperature at 100, 110, 120, 130°C (Figure 7), the values of t_c(S), t_c(1/2), and t_c(E) for four specimen, had the lowest values at 120°C, except for those for PLLA/PLLA-OPOSS^1. The results indicate that PLLA-OPOSS hybrids accelerate crystallization of PLLA as a heterogeneous nucleation agent with a lower content of PLLA-OPOSS hybrids, However, PLLA-OPOSS hybrids with a higher content hinder segmental motion to restrain crystallization of PLLA.

Isothermal crystallization kinetics traced by light intensity are analyzed with the Avrami theory [40], which is expressed in the Equation (2):

$$1 - \frac{I_t - I_0}{I_\infty - I_0} = \exp(-kt_c^n) \tag{2}$$

where $(I_t - I_0)/(I_\infty - I_0)$ is the percentage of relative crystallization, k the crystallization rate constant, and n the Avrami exponent constant depending on the nucleation and growth mechanism. Equation (2) can be transformed to Equation (3).

$$\ln\left[-\ln\left(1 - \frac{I_t - I_0}{I_\infty - I_0}\right)\right] = \ln k + n\ln t_c \tag{3}$$

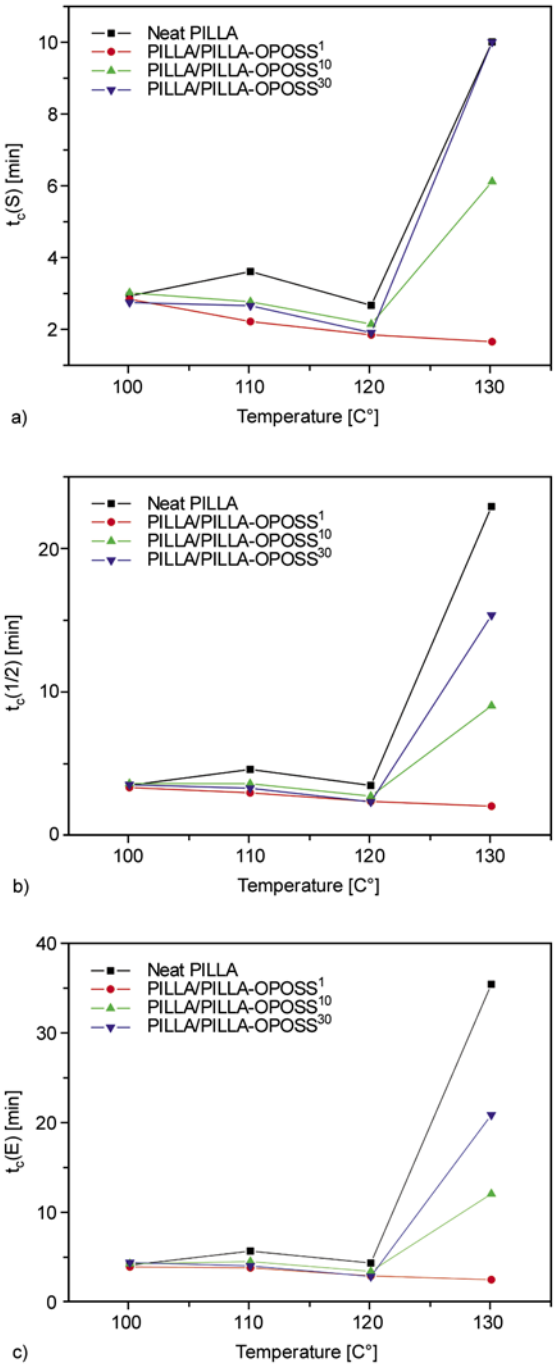

Figure 8. Starting, half, and ending times for neat PLLA and PLLA/PLLA-OPOSS nanocomposites [a) t_c(S), b) t_c(1/2), and c) t_c(E)]

The effects of PLLA-OPOSS content on the plot of $\ln\{-\ln[1 - (I_t - I_0)/(I_\infty - I_0)]\}$ versus $\ln t_c$ could be seen in Figure 8. The overall crystallization rate may be due to the change either in the crystal growth rate or in the nucleation rate. As shown in Figure 9, the curves have a good linear relationship at the beginning, and then exhibit the nonlinear relationship at the end, which may be ascribed to the sec-

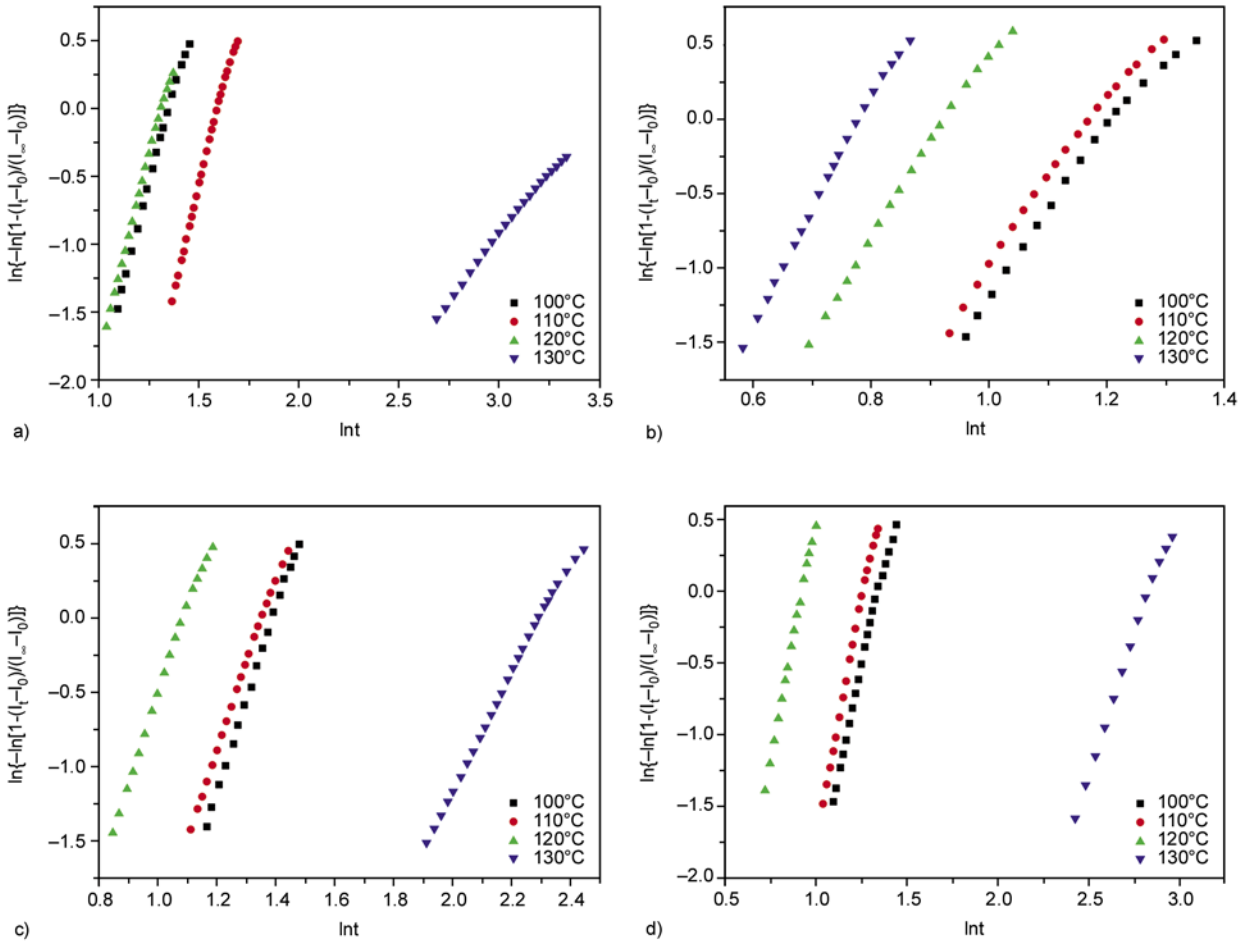

Figure 9. Plots of the degree of crystallinity $\ln\{-\ln[1-(I_t-I_0)/(I_\infty-I_0)]\}$ versus the crystallization time $\ln t_c$ for isothermal crystallization (a) Pure PLLA, (b) PLLA/PLLA-OPOSS 1.0, (c) PLLA/PLLA-OPOSS 10, (d) PLLA/PLLA-OPOSS 30

ondary crystallization. The basically parallel curves are shown in the process of isothermal crystallization at different temperatures, their crystallographic action is similar.

According to Equation (3), when plotting $\ln\{-\ln[1-(I_t-I_0)/(I_\infty-I_0)]\}$ against $\ln t_c$ (Figure 8), the n and k values could be directly obtained from the slope and the natural logarithmic value of the intercept, respectively. From Table 3, it is found that with increasing crystallization temperature the exponent n first increases and then decreases for most of samples. Moreover, it can be observed that the exponent n is found to range from 3.8 to 6.7, which is simlar to those for PLA/nucleating agent systems reported by Liao *et al.* [41] in most cases. It implies that the crystals in the PLLA/PLLA-OPOSS nanocomposites showed heterogeneous nucleation and spherulitic growth [42]. The values of n reported in literatures are related with many ingredients, such as the secondary crystallization, the density of spherulites, nucleation mode and growth mechanism, etc [43].

Table 3. Values of Avrami parameter at various isothermal crystallization temperatures

Samples	T_c [°C]	n	–ln k [min^{-n}]
Neat PLLA	100	5.53	7.50
	110	6.02	9.63
	120	5.75	7.57
	130	3.87	6.53
PLLA/PLLA-OPOSS[1]	100	5.20	6.36
	110	5.39	6.36
	120	6.19	5.76
	130	6.39	5.79
PLLA/PLLA-OPOSS[10]	100	6.10	8.50
	110	5.77	7.83
	120	5.81	6.34
	130	3.87	8.93
PLLA/PLLA-OPOSS[30]	100	5.67	7.64
	110	6.55	8.29
	120	6.72	6.23
	130	3.79	10.75

3.4. Polarized optical microscopy (POM)

The nucleating effect of PLLA-OPOSS hybrids on the crystallization of PLLA is also confirmed by POM. Figure 10 shows polarized optical microscopy images of the crystallization of neat PLLA and PLLA/PLLA-OPOSS nanocomposites. The test samples were prepared by melting the samples on a hot plate at 200°C for 3 minutes, and cooled to 125°C, then maintained for a different crystallization time. The spherulites of PLLA/PLLA-OPOSS nanocomposites are smaller in size and larger in numbers than those of the neat PLLA. As an approximate inclination, the nucleation density increases with increasing of the content of PLLA-OPOSS hybrids. It indicates that PLLA-OPOSS hybrids act as an effective nucleating agent to initiate nucleation and

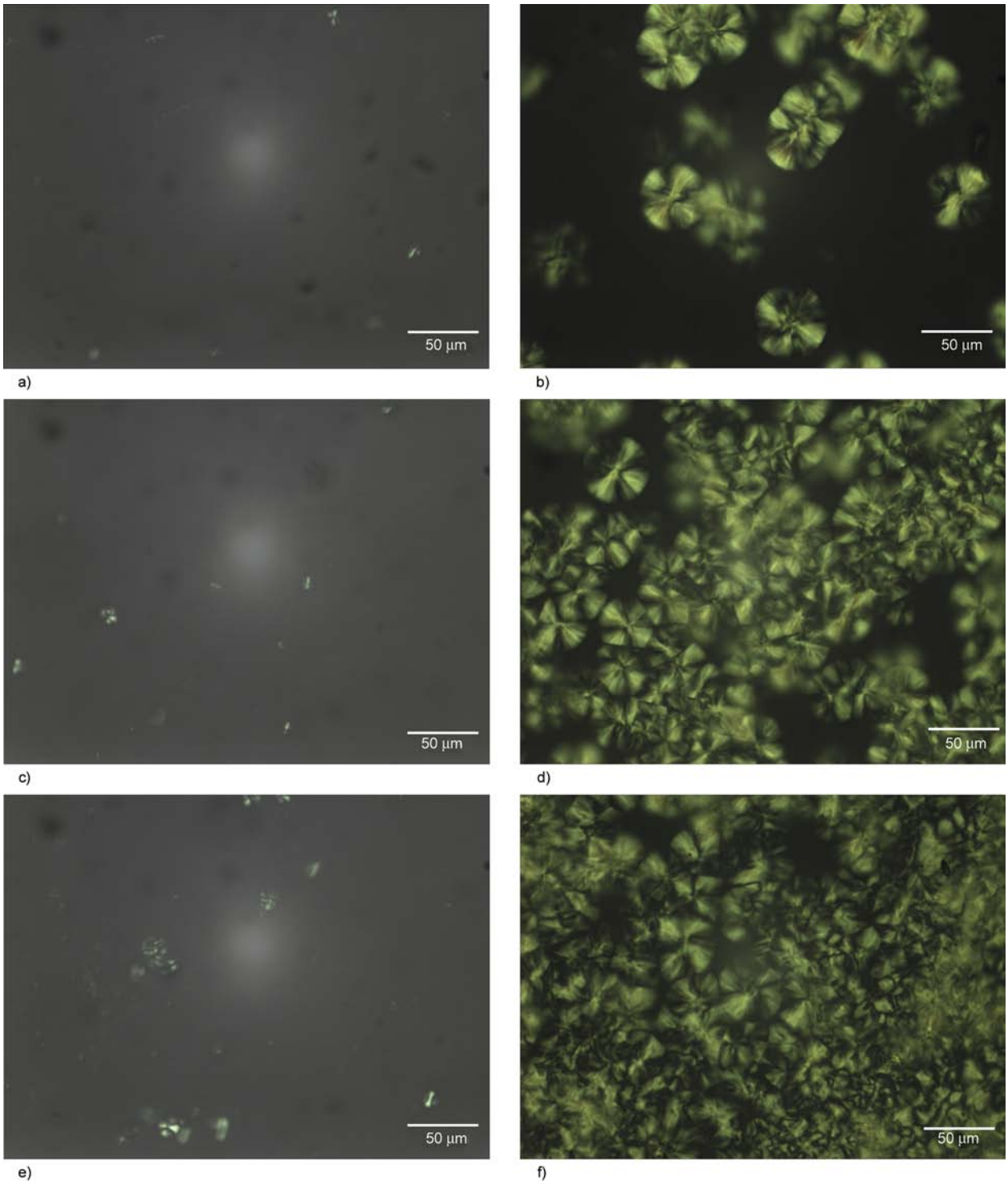

Figure 10. Polarized optical photomicrographs of neat PLLA and PLLA/PLLA-OPOSS nanocomposites at 125°C. Neat PLLA: a) 40 s, b) 5 min; PLLA/PLLA-OPOSS^{10}: c) 40 s, d) 5 min; PLLA/PLLA-OPOSS^{30}: e) 40 s, f) 5 min

increase the nucleation density for PLLA crystallization.

4. Conclusions

In this work, PLLA-OPOSS hybrids were prepared via solution ring-opening polymerization. The formation of secondary hydroxyls due to the reaction between main PLLA chains and OPOSS is evidenced by FTIR and ^{1}H-NMR. X-ray analysis indicates that the presence of OPOSS does not alter the packing structure of PLLA chain in the crystals. The PLLA-OPOSS hybrid with 0.50 mol% OPOSS content is solution-mixed with the neat PLLA polymer to obtain PLLA/PLLA-OPOSS nanocomposites with various PLLA-OPOSS content of 1–30 wt%. It was found that the glass transition temperature of the PLLA/PLLA-OPOSS nanocomposites remained consistent with the neat PLLA and the thermooxidative stability of PLLA/PLLA-OPOSS nanocomposites is improved with the PLLA-OPOSS content of 1–20 wt% compared to the pristine PLLA polymer. PLLA/PLLA-OPOSS nanocomposites have the highest crystallization rate at 120°C, except for PLLA/PLLA-OPOSS[1]. The nucleation density increases with increase in the PLLA-OPOSS content.

Acknowledgements

The work was financially supported by The Key Technology R&D Program of Jiangsu (Project No. BE2010176), Natural science fund for colleges and universities in Jiangsu Province (Project No. 08KJB430004), Scientific and Technological Developing Scheme of Zhenjiang City (Project No. SH2008073).

References

[1] Reed A. M., Gilding D. K.: Biodegradable polymers for use in surgery – Poly(glycolic)/poly(lactic acid) homo and copolymers: 2. *In vitro* degradation. Polymer, **22**, 494–498 (1981). DOI: 10.1016/0032-3861(81)90168-3

[2] Kalb B., Pennings A. J.: General crystallization behaviour of poly(L-lactic acid). Polymer, **21**, 607–612 (1980). DOI: 10.1016/0032-3861(80)90315-8

[3] Marega C., Marigo A., Di Noto V., Zannetti R., Martorana A., Paganetto G.: Structure and crystallization kinetics of poly(L-lactic acid). Die Makromolekulare Chemie, **193**, 1599–1606 (1992). DOI: 10.1002/macp.1992.021930704

[4] Wu D. F., Wu L., Zhang M., Zhao Y. L.: Viscoelasticity and thermal stability of polylactide composites with various functionalized carbon nanotubes. Polymer Degradation and Stability, **93**, 1577–1584 (2008). DOI: 10.1016/j.polymdegradstab.2008.05.001

[5] Ouchi T., Miyazaki H., Arimura H., Tasaka F., Hamada A., Ohya Y.: Synthesis of biodegradable amphiphilic AB-type diblock copolymers of lactide and depsipeptide with pendant reactive groups. Journal of Polymer Science Part A: Polymer Chemistry, **40**, 1218–1225 (2002). DOI: 10.1002/pola.10211

[6] Wang L., Ma W., Gross R. A., McCarthy S. P.: Reactive compatibilization of biodegradable blends of poly (lactic acid) and poly(ε-caprolactone). Polymer Degradation and Stability, **59**, 161–168 (1998). DOI: 10.1016/S0141-3910(97)00196-1

[7] Sarazin P., Favis B. D.: Morphology control in co-continuous poly(L-lactide)/polystyrene blends: A route towards highly structured and interconnected porosity in poly(L-lactide) materials. Biomacromolecules, **4**, 1669–1679 (2003). DOI: 10.1021/bm030034+

[8] Sarazin P., Roy X., Favis B. D.: Controlled preparation and properties of porous poly(L-lactide) obtained from a co-continuous blend of two biodegradable polymers. Biomaterials, **25**, 5965–5978 (2004). DOI: 10.1016/j.biomaterials.2004.01.065

[9] Ray S. S., Yamada K., Okamoto M., Ogami A., Ueda K.: New polylactide/layered silicate nanocomposites. 3. High-performance biodegradable materials. Chemistry of Materials, **15**, 1456–1465 (2003). DOI: 10.1021/cm020953r

[10] Paul M-A., Delcourt C., Alexandre M., Degée P., Monteverde F., Rulmont A., Dubois P.: (Plasticized) polylactide/(organo-)clay nanocomposites by in situ intercalative polymerization. Macromolecular Chemistry and Physics, **206**, 484–498 (2005). DOI: 10.1002/macp.200400324

[11] Chen G-X., Kim H-S., Park B. H., Yoon J-S.: Controlled functionalization of multiwalled carbon nanotubes with various molecular-weight poly(L-lactic acid). The Journal of Physical Chemistry B, **109**, 22237–22243 (2005). DOI: 10.1021/jp054768n

[12] Jiang L., Zhang J. W., Wolcott M. P.: Comparison of polylactide/nano-sized calcium carbonate and polylactide/montmorillonite composites: Reinforcing effects and toughening mechanisms. Polymer, **48**, 7632–7644 (2007). DOI: 10.1016/j.polymer.2007.11.001

[13] Singh S., Ray S. S.: Polylactide based nanostructured biomaterials and their applications. Journal of Nanoscience and Nanotechnology, **7**, 2596–2615 (2007). DOI: 10.1166/jnn.2007.909

[14] Yoon J. T., Jeong Y. G., Lee S. C., Min B. G.: Influences of poly(lactic acid)-grafted carbon nanotube on thermal, mechanical, and electrical properties of poly(lactic acid). Polymers for Advanced Technologies, **20**, 631–638 (2009).
DOI: 10.1002/pat.1312

[15] Lichtenhan J. D., Vu N. Q., Carter J. A., Gilman L. W., Feher F. J.: Silsesquioxane-siloxane copolymers from polyhedral silsesquioxanes. Macromolecules, **26**, 2141–2142 (1993).
DOI: 10.1021/ma00060a053

[16] Shockey E., Jones P. F., Chaffee K. P., Lichtenhan J. D.: Thermal behavior of polyhedral oligosilsesquioxane (POSS)/siloxane copolymers. Polymer Preprints, **36**, 391–392 (1995).

[17] Kannan R., Salacinski H., Butler P., Seifalian A.: Polyhedral oligomeric silsesquioxane nanocomposites: the next generation material for biomedical applications. Accounts of Chemical Research, **38**, 879–884 (2005).
DOI: 10.1021/ar050055b

[18] Harrison P.: Silicate cages: Precursors to new materials. Journal of Organometallic Chemistry, **542**, 141–183 (1997).
DOI: 10.1016/S0022-328X(96)06821-0

[19] Qiu Z. B., Pan H.: Preparation, crystallization and hydrolytic degradation of biodegradable poly(l-lactide)/polyhedral oligomeric silsesquioxanes nanocomposite. Composites Science and Technology, **70**, 1089–1094 (2010).
DOI: 10.1016/j.compscitech.2009.11.001

[20] Liu Y. H., Zeng K., Zheng S. X.: Organic-inorganic hybrid nanocomposites involving novolac resin and polyhedral oligomeric silsesquioxane. Reactive and Functional Polymers, **67**, 627–635 (2007).
DOI: 10.1016/j.reactfunctpolym.2007.04.002

[21] Joshi M., Butola B. S., Simon G., Kukaleva N.: Rheological and viscoelastic behavior of HDPE/octamethyl-POSS nanocomposites. Macromolecules, **39**, 1839–1849 (2006).
DOI: 10.1021/ma051357w

[22] Fina A., Tabuani D., Frache A., Camino G.: Polypropylene–polyhedral oligomeric silsesquioxanes (POSS) nanocomposites. Polymer, **46**, 7855–7866 (2005).
DOI: 10.1016/j.polymer.2005.06.121

[23] Ni Y., Zheng S., Nie K.: Morphology and thermal properties of inorganic–organic hybrids involving epoxy resin and polyhedral oligomeric silsesquioxanes. Polymer, **45**, 5557–5568 (2004).
DOI: 10.1016/j.polymer.2004.06.008

[24] Liu Y., Zheng S., Nie K.: Epoxy nanocomposites with octa(propylglycidyl ether) polyhedral oligomeric silsesquioxane. Polymer, **46**, 12016–12025 (2005).
DOI: 10.1016/j.polymer.2005.09.056

[25] Ni Y., Zheng S. X.: Epoxy resin containing octamaleimidophenyl polyhedral oligomeric silsesquioxane. Macromolecular Chemistry and Physics, **206**, 2075–2083 (2005).
DOI: 10.1002/macp.200500267

[26] Liu H. Z., Zheng S. X., Nie K. M.: Morphology and thermomechanical properties of organic–inorganic hybrid composites involving epoxy resin and an incompletely condensed polyhedral oligomeric silsesquioxane. Macromolecules, **38**, 5088–5097 (2005).
DOI: 10.1021/ma0504318

[27] Zhang W. H., Fu B. X., Seo Y., Schrag E., Hsiao B., Mather P. T., Yang N-L., Xu D., Ade H., Rafailovich M., Sokolov J.: Effect of methyl methacrylate/polyhedral oligomeric silsesquioxane random copolymers in compatibilization of polystyrene and poly(methyl methacrylate) blends. Macromolecules, **35**, 8029–8038 (2002).
DOI: 10.1021/ma020725i

[28] Kopesky E. T., Haddad T. S., McKinley G. H., Cohen R. E.: Miscibility and viscoelastic properties of acrylic polyhedral oligomeric silsesquioxane–poly(methyl methacrylate) blends. Polymer, **46**, 4743–4752 (2005).
DOI: 10.1016/j.polymer.2005.04.001

[29] Kopesky E. T., McKinley G. H., Cohen R. E.: Toughened poly(methyl methacrylate) nanocomposites by incorporating polyhedral oligomeric silsesquioxanes. Polymer, **47**, 299–309 (2006).
DOI: 10.1016/j.polymer.2005.10.143

[30] Huang C-F., Kuo S-W., Lin F-L., Huang W-J., Wang C-F., Chen W-Y., Chang F-C.: Influence of PMMA-chain-end tethered polyhedral oligomeric silsesquioxanes on the miscibility and specific interaction with phenolic blends. Macromolecules, **39**, 300–308 (2006).
DOI: 10.1021/ma051923n

[31] Liu H., Zheng S.: Polyurethane networks nanoreinforced by polyhedral oligomeric silsesquioxane. Macromolecular Rapid Communications, **26**, 196–200 (2005).
DOI: 10.1002/marc.200400465

[32] Turri S., Levi M.: Structure, dynamic properties, and surface behavior of nanostructured ionomeric polyurethanes from reactive polyhedral oligomeric silsesquioxanes. Macromolecules, **38**, 5569–5574 (2005).
DOI: 10.1021/ma047304g

[33] Yoon K. H., Polk M. B., Park J. H., Min B. G., Schiraldi D. A.: Properties of poly(ethylene terephthalate) containing epoxy-functionalized polyhedral oligomeric silsesquioxane. Polymer International, **54**, 47–53 (2005).
DOI: 10.1002/pi.1661

[34] Zeng J., Kumar S., Iyer S., Schiraldi D. A., Gonzalez R. I.: Reinforcement of poly(ethylene terephthalate) fibers with polyhedral oligomeric silsesquioxanes (POSS). High Performance Polymers, **17**, 403–424 (2005).
DOI: 10.1177/0954008305055562

[35] Kim J. K., Yoon K. H., Bang D. S., Park Y-B., Kim H-U., Bang Y-H.: Morphology and rheological behaviors of poly(ethylene terephthalate) nanocomposites containing polyhedral oligomeric silsesquioxanes. Journal of Applied Polymer Science, **107**, 272–279 (2008).
DOI: 10.1002/app.27038

[36] Zhao Y., Schiraldi D. A.: Thermal and mechanical properties of polyhedral oligomeric silsesquioxane (POSS)/polycarbonate composites. Polymer, **46**, 11640–11647 (2005).
DOI: 10.1016/j.polymer.2005.09.070

[37] Lee J. H., Jeong Y. G.: Preparation and characterization of nanocomposites based on polylactides tethered with polyhedral oligomeric silsesquioxane. Journal of Applied Polymer Science, **115**, 1039–1046 (2009).
DOI: 10.1002/app.31076

[38] Ho C-H., Jang G-W., Lee Y-D.: Crystallization of poly(L-lactide-dimethyl siloxane-L-lactide) triblock copolymers and its effect on morphology of microphase separation. Polymer, **51**, 1639–1647 (2010).
DOI: 10.1016/j.polymer.2009.11.030

[39] Xu H., Teng C., Yu M.: Improvements of thermal property and crystallization behavior of PLLA based multiblock copolymer by forming stereocomplex with PDLA oligomer. Polymer, **47**, 3922–3928 (2006).
DOI: 10.1016/j.polymer.2006.03.090

[40] Brochu S., Prud'homme R. E., Barakat I., Jerome R.: Stereocomplexation and morphology of polylactides. Macromolecules, **28**, 5230–5239 (1995).
DOI: 10.1021/ma00119a010

[41] Liao R. G., Yang B., Yu W., Zhou C.: Isothermal cold crystallization kinetics of polylactide/nucleating agents. Journal of Applied Polymer Science, **104**, 310–317 (2007).
DOI: 10.1002/app.25733

[42] Kolstad J. J.: Crystallization kinetics of poly(L-lactide-*co*-*meso*-lactide). Journal of Applied Polymer Science, **62**, 1079–1091 (1996).
DOI: 10.1002/(SICI)1097-4628(19961114)62:7<1079::AID-APP14>3.0.CO;2-1

[43] Ikada Y., Jamshidi K., Tsuji H., Hyon S. H.: Stereocomplex formation between enantiomeric poly(lactides). Macromolecules, **20**, 904–909 (1987).
DOI: 10.1021/ma00170a034

eXPRESS Polymer Letters Vol.5, No.8 (2011) 674–684
Available online at www.expresspolymlett.com
DOI: 10.3144/expresspolymlett.2011.66

Temperature window effect and its application in extrusion of ultrahigh molecular weight polyethylene

L. M. Fang[1,2*], *P. Gao*[3], *X. W. Cao*[2]

[1]Biomedical Engineering Institute, South China University of Technology, Guangzhou 510640, China
[2]Key Laboratory of Polymer Processing Engineering, Ministry of Education, South China University of Technology, Guangzhou 510640, China
[3]Department of Chemical and Biomolecular Engineering, The Hong Kong University of Science and Technology, Clear Water Bay, Kowloon, Hong Kong

Received 9 December 2010; accepted in revised form 31 January 2011

Abstract. Ultrahigh molecular weight polyethylene (UHMWPE) was ram extruded using a temperature window effect. The extrusion pressure abruptly drops at a very narrow extrusion temperature window which is about 10°C higher than the theoretical melting point of orthorhombic polyethylene crystals under quiescent and equilibrium states. The correlation between extrusion pressure and parameters such as extrusion temperature, annealing condition, thermal history, piston velocity, *L*/*D* ratio of the die, and molecular weight of UHMWPE, was studied. The temperature window increases with molecular weight and is unaffected by thermal history and annealing. The stable extrusion pressure and the critical piston velocity decrease with the rise in the extrusion temperature. The flow resistance reversely depends on the *L*/*D* ratio of the die. This phenomenon is attributed to an extensional flow-induced chain alignment along the streamline, which results in the formation of a metastable mesophase with higher chain mobility.

Keywords: *biocompatible polymers, processing technologies, temperature window, UHMWPE*

1. Introduction

Ultrahigh molecular weight polyethylene (UHMWPE) exhibits extraordinary properties, such as wear and impact resistance, which make the material ideal for application as joint prostheses and bullet-proof vests [1, 2]. However, its extremely high melt viscosity makes processing via conventional techniques, such as screw extrusion or injection molding, difficult [3].

Problems that are commonly encountered in processing UHMWPEs include die blockage, melt fracture, wall slippage, and a small processing temperature window. Processing UHMWPE, therefore, requires a proper combination of temperature, pressure, and sufficient time to achieve complete plastification. Inadequate control of the process can lead to fusion defects stemming from the memory of the powder morphology [1, 4]. Currently, UHMWPE resin is consolidated mainly by compression molding or ram extrusion [3]. Compression molding progresses slowly and involves costly equipment, whereas ram extrusion is relatively cheap. However, some unconsolidated regions in the center of the material may occur. Considerable efforts have been devoted to developing better methods for UHMWPE processing.

Since the discovery of the extended-chain hexagonal crystal phase of polyethylene in the 1960s [5, 6], the enhanced chain mobility of this phase has elicited numerous theoretical and experimental investigations. However, the extremely high pressure (>360 MPa) and temperature (>230°C) associ-

*Corresponding author, e-mail: lmfang@scut.edu.cn

ated with the formation of hexagonal crystals make processing in this phase almost impossible. The crystallization of chain segments immediately after synthesis reduces the likelihood of entanglement formation and favors more extended chain conformations; thus, nascent reactor powders have been suggested to possess low degrees of entanglement [7, 8]. Because of this, solid-state extrusion or cold extrusion was developed. However, the extrudate needs to be drawn into fibers or films after cold extrusion [9].

In 1990, Waddon and Keller [10] observed a strange phenomenon during capillary rheological tests of medium high molecular weight polyethylene (MHMWPE). In a narrow temperature interval (150–152°C), a minimum melt flow resistance was discovered. Keller and his associates called this phenomenon 'temperature window effect' and systematically investigated it in a series of papers [11–13] and in a review [14]. Keller and coworkers [15–22], Cheng [23] and Somani *et al.* [25] independently or collaboratively studied the mechanisms of unexpected melt flow behavior, and attributed reduced flow resistance to the transient mobile hexagonal mesophase by flow-induced chain alignment critical to strain rate and molecular weight. This hypothesis was confirmed by the observation of the orthorhombic transformation to the hexagonal phase through in situ wide angle X-ray diffraction [25–27].

These new findings have potential significance for polymer processing at low pressures. However, the window effect is strongly dependent on molecular weight. Kolnaar and Keller [11] defined molecular weight dependence within the range of $1.3 \cdot 10^5$ to $1.0 \cdot 10^6$ g/mol. To process UHMWPE in the temperature window, Narh and Keller [28] dissolved nascent UHMWPE in a solvent, extruded the dried gel, and obtained a pronounced pressure minimum at which a smooth extrudate was observed. However, a large amount of toxic solvent, usually decalin or xylene, is employed in this process. A solution-free route is preferred. Rastogi *et al.* [27] studied the orthorhombic-hexagonal phase transition of solution-crystallized UHMWPE by *in situ* small-angle X-ray scattering at pressures of 160 and 180 MPa during heating or cooling. The experiments revealed that the location of the triple point in the pressure-temperature phase diagram of polyethylene depended on crystal dimensions, that is, fold length. Based on the results, a UHMWPE sheet was compression-molded in the hexagonal phase at 120 MPa and 205°C, and then subsequently melted and recrystallized isobarically. The fusion defects substantially decreased, but the processing pressure and temperature were still excessively high.

Previous studies have indicated that the temperature window effect depends on hexagonal phase stability, which in turn, depends on the alignment of polymer chains [15–17, 22, 29]. Compared with MHMWPE, UHMWPE chains are much longer. Accordingly, disentanglement and alignment of UHMWPE chains are much more difficult. Therefore, the key is to induce the mobile hexagonal phase by an elongational flow field and then maintain its stability. The aim of this paper is to study influences of various factors, including extrusion temperature, annealing condition, thermal history, piston velocity, *L*/*D* ratio of the die, and molecular weight of UHMWPE, on the temperature window effect, mainly from the processing viewpoint.

2. Experimental

2.1. Materials and equipment

Three UHMWPE resins were used. M-II and M-III, with molecular weights (M_w) 2.5 and 3.5 million g/mol, respectively, were purchased from Beijing Eastern Petrochemical Co., Ltd (Beijing, China). GUR 1050, with an M_w of 4.9 million g/mol, was supplied by Ticona (Celanese Co., Ltd., Singapore). A high pressure capillary rheometer (Rheologic 5000-Twin, CEAST S.P.A., Pianezza, Italy) was used to process UHMWPE rods. The barrel length and diameter are 300 and 15 mm, respectively. The temperature was controlled in the range of 50–450°C with an accuracy of 0.5°C. The working ranges of the force transducer, pressure transducer, and piston velocity were 5–40 kN, 3.5–200 MPa, and 0.01–1000 mm/min, respectively. VisualRHEO software (CEAST S.P.A., Pianezza, Italy) was used to control the extrusion process and analyze the processing parameters.

Convergent cylindrical dies with an entrance angle of 90°, length/diameter *(L*/*D*) ratio of 10:5, 15:5, and 18:5 [mm/mm], and total length of 40 mm were designed (Figure 1). A part of the screw was machined to the bottom of the self-made hardened stainless steel die, and a bolt was used to prevent the powder from leaking during charging.

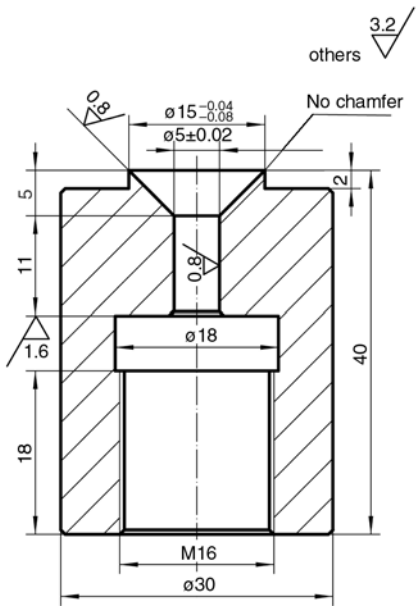

Figure 1. Typical design drawing of the extrusion die (*L*/*D* ratio: 10:5, mm/mm)

2.2. Extrusion procedures

The extrusion steps are listed as follows: 1) The entire system, including the piston, barrel, and die, was carefully cleaned because surface quality influences extrusion pressure. 2) The system was setup with proper alignment and tight contact of parts to reduce friction and ensure that the melt is not expelled from the gap. 3) The barrel was intermittently charged with powder and then compressed to obtain densely packed particles. 4) Gas/moisture trapped in the nodular pores was released by degassing at 120°C. 5) The resin was melted at a given temperature and pressure at specific periods (30, 60, and 90 min). 6) The melt was cooled to the extrusion temperature window. 7) The temperature was conditioned for about 15 min to reach equilibrium and avoid the temperature gradient between the wall and the center. 8) The block was uninstalled and the extrusion carried out at a preset piston velocity.

Majority of the experiments consisted of measuring pressure (p) as a function of temperature (T) at a constant piston velocity (v). Pressure traces were recorded as a function of time at a fixed piston velocity while the barrel temperature was kept constant. Various parameters, including extrusion temperature, annealing process, thermal history, piston velocity, L/D ratio of the die, and molecular weight, were investigated during UHMWPE processing via the metastable phase.

3. Results and discussion

3.1. Effects of temperature

The resin (M II) was melted at 200°C for 1 h under 45 MPa; the temperature was then decreased to 145°C and the pressure was decreased to around 2 MPa. After being conditioned for 15 min, the melt was extruded at a speed of 0.035 mm/s. Pressure traces were recorded as a function of time (Figure 2). Figure 2 indicates that extrusion pressure linearly increases with extrusion time, and then abruptly decreases after 50–160 seconds in the temperature range of 154–157°C. This temperature range is defined as the temperature window and the phenomenon is called the temperature window effect [10]. If extrusion temperature is below this window, the pressure continuously increases to the maximum working range of the transducer; thus, the rod cannot be extruded. If the extrusion temperature is higher than the window, pressure begins to fluctuate and the rod becomes distorted. Higher tem-

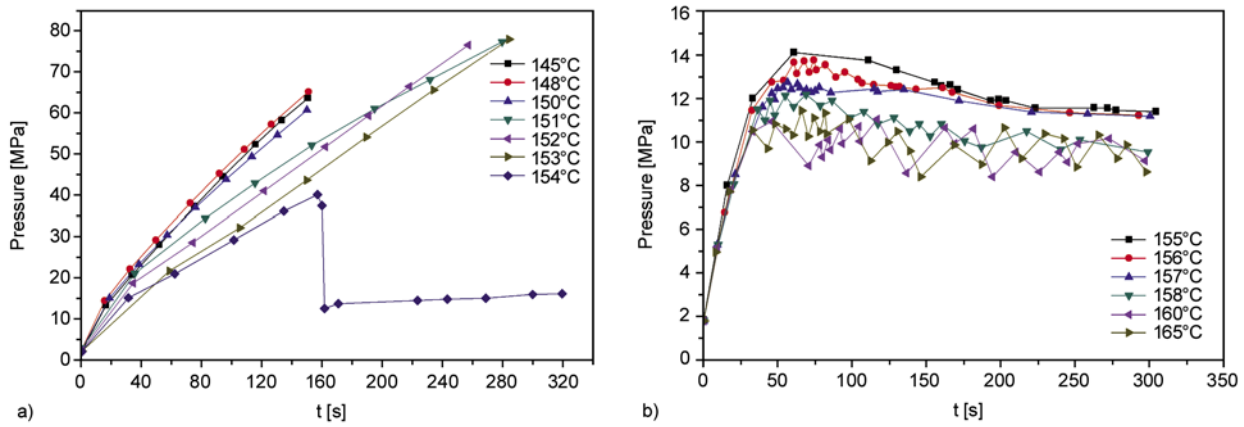

Figure 2. Time evolution of extrusion pressure at different extrusion temperatures ($M_w = 3.5 \cdot 10^6$ g/mol; L/D = 10:5, mm/mm; v = 0.035 mm/s)

perature brings about more severe fluctuation, implying that the stable extrusion of the material can only be performed within the narrow temperature window.

Below the temperature window, the UHMWPE melt exhibits elastic behavior. Flow activation energy is too high to generate flow of the entangled melt, causing the extrusion pressure increases with the extrusion time. The work done by the compression of the piston is stored in the melt. With the increase of extrusion temperature, the chain mobility in UHMWPE melt is enhanced, leading to the decrease of extrusion pressure.

When the extrusion temperature is increased to 154°C, the melt is compressed at the initial stage and flows like rubber for about 150 s. The melt flows from the entry of the convergent die (~5.0 mm) and enters the 'capillary'. The extent of chain extension differs from the center to the wall. The elastic energy stored in the melt during flow in the convergent entry of the die is released abruptly when the melt enters the capillary, thereby reducing extrusion pressure. The melt flows steadily at a constant extrusion speed – a phenomenon that can be explained from two aspects: (1) chain mobility is enhanced at temperatures 10°C higher than the theoretical equilibrium melting point of orthorhombic polyethylene crystals [30]; and (2) chains are extended at the orifice and aligned along the flow direction, producing a chain-extended structure similar to the hexagonal crystal phase [26]. This is the so-called elongational flow-induced crystallization [11]. With the increase in extrusion temperature, the flow activation energy declines, and the amplitude of the pressure drop is of lower magnitude. However, in all the experiments, the pressure stabilizes at around 12 MPa in the temperature window 154–157°C, yielding an extrudate with a smooth surface (Figure 3a).

After the temperature is increased to 158°C, extrusion becomes unstable immediately after the initial stage. The extended chain structure induced by elongational flow is a non-equilibrium state, and this transient phase is metastable in a narrow temperature range under shear [14]. Non-equilibrium-extended chains transform into entangled chains, achieving an equilibrium state. Chain entanglement in the melt becomes severe at high temperature, and critical shear rate is very small, resulting in melt fracture (Figure 3b). With the increase in extrusion temperature, the pressure fluctuation becomes violent, and the extrudate surface becomes severely distorted, as revealed by the fluctuation amplitude and frequency.

Further increasing the temperature to above 200°C, which is the temperature range for traditional ram extrusion, makes for successful processing. However, the extrusion speed is slower and the extrusion pressure is much higher compared with those in the temperature window 154–157°C [1].

3.2. Effects of annealing process

Kolnaar and Keller [11] reported that the resin should be annealed sufficiently to erase the nascent structure before extrusion in the temperature window. To study the influence of annealing process on the temperature window effect during the extrusion of UHMWPE, we melted the resin at different temperatures (180 or 200°C) for certain time periods

Figure 3. Photos of rods extruded at different temperatures (M_w = 3.5·10^6 g/mol; L/D = 10:5, mm/mm; v = 0.035 mm/s). a) In the temperature window (T = 154°C); b) above the temperature window (T = 165°C)

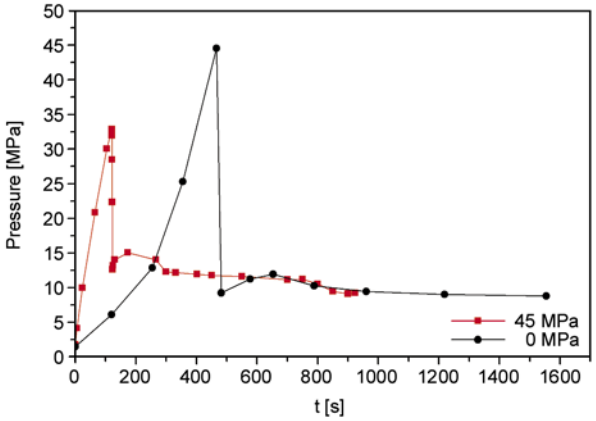

Figure 4. Time evolution of extrusion pressure profile under different annealing pressures during annealing at 200°C for 1 h (M_w = 3.5·10^6 g/mol; L/D = 10:5, mm/mm; v = 0.035 mm/s; T = 154°C)

(30, 60, or 90 min) under pressure (45 or 0 MPa). The melt temperature was then decreased to the temperature window and conditioned for 15 min. The extrusion pressure evolution with time was recorded during extrusion at a piston velocity of 0.035 mm/s.

Figure 4 shows the effect of annealing pressure on the extrusion pressure. After being extruded for about 130 s, the extrusion pressure drops for the melt annealed under pressure, whereas the pressure drop delays to over 450 s for the melt annealed without pressure. Annealing under pressure also decreases the maximum extrusion pressure by more than 10 MPa. This behavior indicates that the melt is loosely packed when annealed without pressure, but well-compacted under high pressure. This also explains the linear increase in the extrusion pressure during the initial stage in Figure 2. However, the temperature window effect always occurs whether annealing pressure is applied or not. The temperature window effect does not depend on the annealing process because the extrusion pressure always exhibits a linear increase with time in the initial stage and abruptly decreases at a maximum value, finally reaching a stable value. The only difference is the starting time of the temperature window effect and the strength of the pressure drop. Annealing under higher temperature, greater pressure, and longer time leads to a faster and larger extrusion pressure drop.

3.3. Effects of heating/cooling reversibility

To study the reversibility of the temperature window effect, we extruded UHMWPE during heating and cooling (145↔175°C). UHMWPE was heated to 175°C and conditioned for 15 min before extrusion at a constant piston velocity to obtain the extrusion pressure. The extrusion pressure fluctuated with time; thus, the average pressure was recorded and the amplitudes were represented by arrows in Figure 5. The melt was cooled to a preset temperature and the process was repeated. A stable extrusion pressure was recorded in the temperature window (154–157°C). Further cooling below the temperature window linearly increased the extrusion pressure with time; thus, the pressure at a given time after extrusion was used. The melt was then heated and the same extrusion and data recording procedures as those conducted in the cooling process were repeated. Finally, the extrusion pressure was plotted with temperature, depicted in Figure 5.

The temperature window effect appears during both cooling and heating processes. The temperature window range and the minimum pressure do not depend on cooling or heating. However, the extrusion pressure initially decreases and then increases

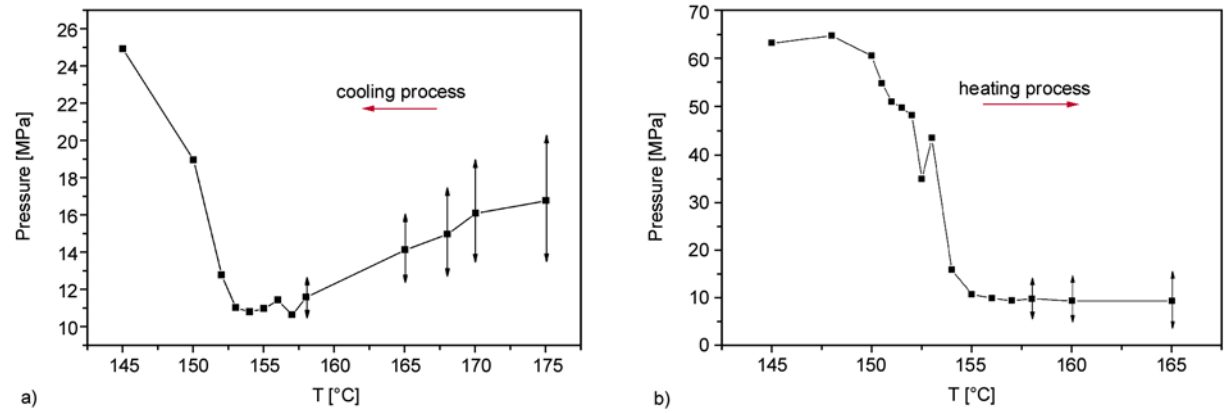

Figure 5. Extrusion pressure profile with extrusion temperature during a) cooling and b) heating (M_w =3.5·10^6 g/mol; L/D = 10:5, mm/mm; v = 0.035 mm/s)

with temperature upon cooling (Figure 5a), whereas it constantly decreases upon heating (Figure 5b). When extruded below the temperature window, the extrusion pressure during the heating process is higher than that during the cooling process at the same temperature. When extruded above the temperature window, the extrusion pressure during heating is lower than that during the cooling process at the same temperature. All these behaviors indicate that the most critical step in extrusion is to induce the temperature window effect, which depends on the stability of the oriented chain structure. The extrusion is a process to induce the chain orientation, while the temperature affects the stability of the oriented chain structure. The two factors combined together determine whether the temperature window effect happens or not. The extrusion pressure should be sufficiently high to induce the chain orientation, particularly during the heating process. The chain relaxation time is very long, so the oriented chain structure is maintained to some extent after the temperature window effect happens, leading to a relatively lower extrusion pressure. Therefore, the extrusion pressure at the same temperature is reversed during the cooling and heating processes. Kolnaar and Keller [11] reported that the window effect arises both upon heating and cooling in extruding MHMWPEs. However, the occurrence of the effect on cooling was erratic in their experiments. The window effect always appears upon heating but does not always appear upon cooling. Furthermore, if it does appear upon cooling, it is not always at the same strength [11]. This was eventually traced to a structure 'memory' effect [11], which implies that some structure formation can be induced more reliably in the heating than in the cooling process of a thermal cycle; once introduced, it can leave a structure memory in the melt state. Different from the extrusion of MHMWPE, the window effect always occurs both upon heating and cooling during UHMWPE extrusion. One possible reason is that the chain relaxation time of the UHMWPE chains is much longer so that the chain alignment induced by elongational flow can at least be partially maintained. In the second heating or cooling cycle, these well-aligned chains can re-induce the temperature window effect.

3.4. Effects of piston velocity

After being melted at high temperature, the UHMWPE melt was cooled to the temperature window. The temperature was kept constant, and the melt was extruded at a constant speed. After occurrence of the temperature window effect, the trace of extrusion pressure with time was recorded. The piston velocity was increased stepwise, and the corresponding pressure evolution with time was recorded. The temperature was increased, and the process was repeated to observe the extrusion pressure traces with time (Figure 6a–d). The final equilibrium pressure was recorded in stable extrusion, whereas average pressure was calculated in fluctuation. The variations in the extrusion pressure with piston velocity under different temperatures were plotted, and depicted in Figure 6e.

Figures 6a–d show that the extrusion pressure is stable below a critical piston velocity. Outside this setting, it fluctuates with time. Higher piston velocity generates more severe fluctuation. The critical piston velocities decrease with the extrusion temperature, which are 0.20, 0.10, 0.05, and 0.05 mm/s at extrusion temperatures of 154, 155, 156, and 157°C, respectively. Figure 6e reveals the effects of piston velocity and extrusion temperature on extrusion pressure. Apparently, the extrusion pressure decreases with an increase in piston velocity and extrusion temperature. The extrusion pressure at 154°C is inconsistent with the trend possibly because of experimental errors.

The UHMWPE chains are aligned along the flow direction in the die during extrusion, and alignment becomes exceedingly complete with the increase in piston velocity, decreasing flow resistance. When the speed reaches a critical value, the wall slip and wall stick take place alternately. Thus, the extrudate is significantly distorted because of the melt fracture. With the increase in temperature in the temperature window, the thermal motion of the chains increases, which is favorable to the extension and alignment of the chains. This increase in the thermal motion of the chains decreases the extrusion pressure. At the same time, the stability maintaining the alignment of extended chains decreases; hence, the range of piston velocity for steady extrusion becomes narrow.

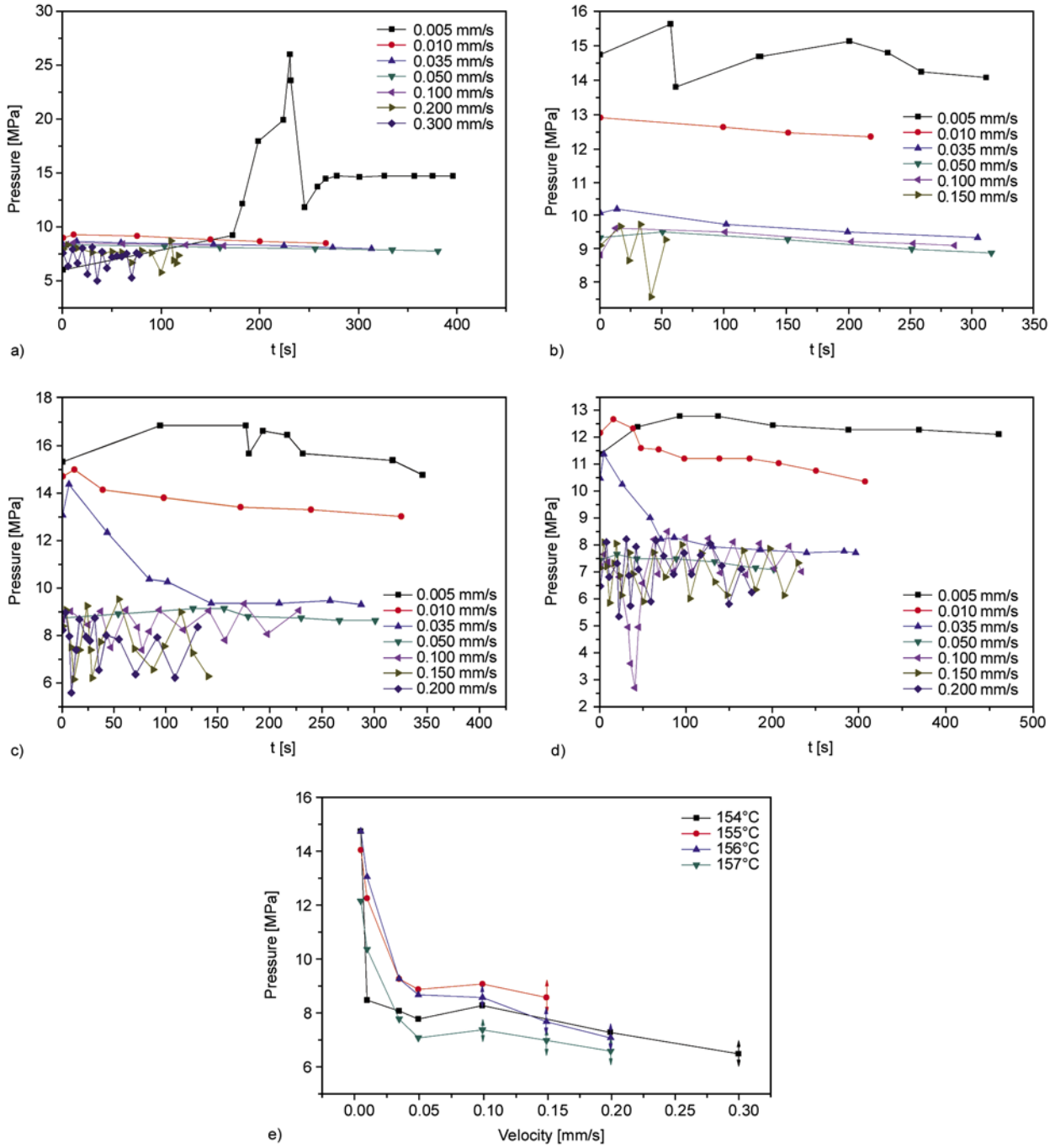

Figure 6. Extrusion pressure traces with time (a) $T = 154$°C; b) $T = 155$°C; c) $T = 156$°C; d) $T = 157$°C) and velocity e) ($M_w = 3.5 \cdot 10^0$ g/mol; $L/D = 10{:}5$, mm/mm)

3.5. Effects of *L*/*D* ratio of the die

After being melted sufficiently, the UHMWPE melt was cooled and maintained at a preset temperature. The melt was extruded at a constant piston velocity, and the stable extrusion pressure was recorded. In unstable extrusion, the average pressure was calculated, and the fluctuation amplitude of pressure was represented by double arrows in Figure 7. With further decrease in temperature, the extrusion pressure was recorded at a given temperature until the melt could no longer be extruded. The procedure was repeated for the other two dies with different *L*/*D* ratios. The extrusion pressure traces with temperature during extrusion using dies with different *L*/*D* ratios are shown in Figure 7.

Figure 7 clearly reveals that the trend of extrusion pressure with temperature and the range of the temperature window effect do not depend on the *L*/*D*

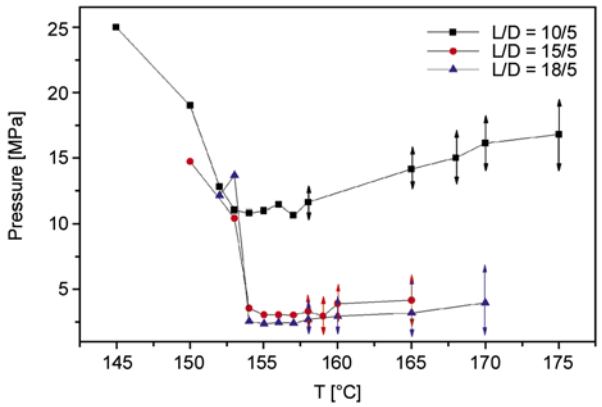

Figure 7. Effects of temperature on the extrusion pressure using extrusion dies with different L/D ratios ($M_w = 3.5 \cdot 10^6$ g/mol; $v = 0.035$ mm/s)

ratio of the die. In addition, the pressure decreases with the increase in L/D ratio at the same temperature. The temperature window effect is attributed to the chain alignment at the convergent die entrance by elongational flow, indicating that the formation of a chain-extended structure and the stability of this structure are key factors. The die entry geometry and angle are unchanged. Accordingly, the elongational flow field at the entrance is also unchanged. Thus, the temperature window effect is not affected by L/D ratio. The strength of pressure drop increases with L/D ratio because of the relaxation of the chains in the capillary. The long chains are extended more sufficiently with the increase in capillary length, thereby generating a larger pressure drop.

3.6. Effects of molecular weight

We extruded three UHMWPE resins to study the effect of molecular weight on the temperature window effect. The extrusion pressure versus extrusion temperature traces for different molecular weights are shown in Figure 8.

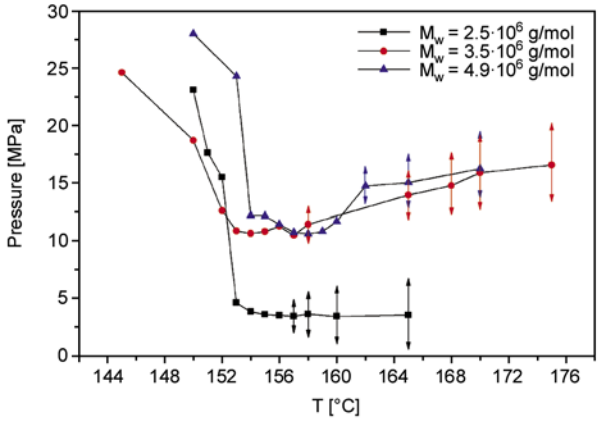

Figure 8. Effects of molecular weight on extrusion pressure at different extrusion temperatures (L/D = 10:5, mm/mm; $v = 0.035$ mm/s)

The three types of UHMWPE all exhibit the temperature window effect during extrusion. Below the window, the extrusion pressure increases with time and blockage happens; above the window, the pressure fluctuates. In the window, the pressure significantly drops to a stable value, yielding a smooth extrudate surface. The ranges of the temperature window for UHMWPE with molecular weights of $2.5 \cdot 10^6$, $3.5 \cdot 10^6$, and $4.9 \cdot 10^6$ g/mol are 153–156, 154–157, and 157–160°C, respectively. A quantitative relationship between the molecular weight and the mean temperature (T) of the window effect is obtained by linear fitting of the data, which gives the Equation (1):

$$T \pm 1.5\ [°C] = 1.7 \cdot 10^{-6}\ [°C \cdot mol/g] \cdot M_w\ [g/mol] + 150\ [°C] \quad (1)$$

The onset extrusion temperature required to induce the temperature window effect increases with molecular weight. In fact, the temperature window observed in MHMWPE ($2.8 \cdot 10^5$–$4.0 \cdot 10^5$ g/mol) by Kolnaar and Keller is 151±1°C [14], which also satisfies Equation (1) quite well. With the increase in molecular weight, the chain length increases and chain mobility decreases. The energy needed to activate chain extension and alignment increases; hence the onset temperature employed to induce the temperature window effect rises. In addition, the extrusion pressure in the temperature window also increases with the molecular weight of UHMWPE. This is due to the fact that the chain entanglement density increases with molecular weight, and the shear stress needed to disentangle the long chains during flowing in the die increases accordingly.

3.7. Mechanism analysis

The processability of UHMWPE is determined by the mobility of its macromolecules. In the melt state, long chains are entangled, and chain relaxation is slow. In the crystal state, long chains are folded or extended in an orderly manner with less entanglement. Under equilibrium conditions, the quiescent melting point of nascent UHMWPE is around 142–143°C, very close to the theoretical equilibrium melting point of orthorhombic polyethylene crystals. After erasing the thermal history, the quiescent melting point decreases to 132–135°C

[26]. In the flow state, the elongational flow in the die causes chain extension and induces the formation of extended chain crystals. Therefore, a mixture of melt phase and crystal like phase coexists at temperatures around 10°C higher than the theoretical quiescent melting point. UHMWPE continues to exhibit a solidified behavior with large elasticity, blocking the extrusion at the die entrance.

According to chain dynamics, phase and its behavior are closely related to material properties, and these properties may change significantly during phase transition [23]. There are three types of polyethylene crystal phases, i.e., orthorhombic, hexagonal, and monoclinic [30]. The hexagonal crystal phase has a chain-extended structure and a large laminar thickness, which demonstrates a higher chain mobility than in the other two phases [22]. However, the hexagonal crystal phase exists stably only under high temperature (>230°C) and pressure (>360 MPa) during the equilibrium process [30]. These strict conditions are difficult to satisfy in practical processing. The extremely large size of UHMWPE chains determines its phase transition, which proceeds much more slowly than that in low molecular materials, making the equilibrium stable phases difficult to obtain. Thus, metastable phases may appear during the phase transition process.

The temperature window effect may be due to the formation of a metastable mobile phase induced by the elongational flow [31]. The chains are aligned along the extrusion direction in the die during extrusion and form a metastable structure similar to that of the hexagonal phase of polyethylene. The verification of this metastable phase transition needs specially designed equipment not readily available in our lab. However, many reports on studying the metastable phase transition of polyethylene can be found in literature.

Waddon and Keller [10] observed the metastable hexagonal phase transition in the temperature window of 150±1°C in MHMWPE extrusion ($2.8 \cdot 10^5$ g/mol) by *in situ* XRD. Rastogi *et al.* [27] determined the metastable hexagonal phase transition of UHMWPE ($3 \cdot 10^5$–$5 \cdot 10^5$ g/mol) at around 205°C by in situ XRD investigation with isobaric (160 and 180 MPa) heating. Chen *et al.* [32] examined the metastable phase transition of polyethylene ($7.8 \cdot 10^4$ g/mol) under a transmission electron microscope. All these reports show that the metastable phase transition of polymers can be induced by elongational and shear flow in melts and mechanical deformation in solids at certain temperature and pressure.

The chain dynamics of UHMWPE during extrusion in the temperature window is complicated. From a mechanics point of view, the melt flow resistance, mainly including the stick force at wall and the shear force between chains, depends on the shear rate. When the pressure is high enough to overcome the flow resistance, the melt starts to flow and the chains are oriented along the flow direction. The oriented chain structure leads to significantly reduced flow resistance and its stability depends on the shear rate, or the piston velocity. From a thermodynamic point of view, flow induced chain extension results in the formation of extended-chain crystals; on the other hand, thermally induced chain relaxation results in the melting of crystals. The increased thermal mobility leads to faster relaxation because of entropic forces, which entangles the chains. The stability of the mesophase is, therefore, determined by the competition between external and internal factors.

Temperature is the most important factor in the temperature window effect. It should be high enough to activate chain extension, but sufficiently low to avoid chain entanglement. Therefore, it should be on the borderline between solid and melt. Because viscosity is proportional to the power 3.4 of molecular weight [11], the temperature needed to activate the rheological flow of UHMWPE melt should increase accordingly. This explains the onset temperature required to trigger the window effect increasing with the molecular weight of UHMWPE (Figure 8). Annealing and thermal history do not change the chain structure. Hence, they do not influence the temperature window effect. The piston velocity and L/D ratio mainly affect the chain extension in the die. With the increase in piston velocity and L/D ratio, the chain extension becomes exceedingly complete. However, if the velocity is excessively high, wall slip is prone to happen, especially at higher extrusion temperatures in which the extended chain structure is easily broken to form entanglements. This explains the results in Figure 6 and Figure 7.

4. Conclusions

UHMWPE rods were ram extruded at low temperature and pressure using the temperature window effect. In the narrow temperature window, the extrusion pressure abruptly decreases, and the undistorted extrudates show a smooth surface. This effect is attributed to the formation of a transient mesophase induced by the elongational flow in the convergent capillary die, resulting in the alignment of chains along the flow direction. This phase exhibits an extended chain structure similar to the mobile hexagonal phase at high temperature and pressure under the equilibrium state. However, the phase is metastable and becomes stable under certain conditions. This study explored the factors influencing metastability, such as extrusion temperature, annealing process, thermal history, extrusion speed, L/D ratio of the die, and molecular weight of UHMWPE. The conclusions are summarized as follows:

The temperature window is in the range 153–160°C, and increases with the increase in molecular weight. The effect does not depend on the annealing process and is reversible on either cooling or heating. The extrusion pressure decreases with the increase in extrusion speed and temperature. It begins to fluctuate when the speed is greater than a critical value; the higher the temperature, the smaller the critical value. The effect does not depend on the L/D ratio of capillary die, but the minimal pressure decreases with the increase in L/D ratio. The minimal extrusion pressure in the temperature window increases with the increase in molecular weight.

The proposed method provides a new solution for the difficulties encountered in processing UHMWPE. Compared with other methods, it features no processing aids, no blending polymers, no equipment improvement, along with attractive attributes such as low energy consumption and high productivity.

Acknowledgements

This work was financially supported by the National Natural Science Foundation of China (No. 50803019) and the Guangdong Natural Science Fund (No. 8451064101000727), and partially supported by the Opening Project of The Key Laboratory of Polymer Processing Engineering, Ministry of Education, China.

References

[1] Dumitriu S.: Polymeric biomaterials. Marcel Dekker, New York (2002).

[2] Kelly J. M.: Ultra-high molecular weight polyethylene. Journal of Macromolecular Science Part C: Polymer Reviews, **42**, 355–371 (2002).
DOI: 10.1081/MC-120006452

[3] Kurtz S. M., Muratoglu O. K., Evans M., Edidin A. A.: Advances in the processing, sterilization, and crosslinking of ultra-high molecular weight polyethylene for total joint arthroplasty. Biomaterials, **20**, 1659–1688 (1999).
DOI: 10.1016/S0142-9612(99)00053-8

[4] Olley R. H., Hosier I. L., Bassett D. C., Smith N. G.: On morphology of consolidated UHMWPE resin in hip cups. Biomaterials, **20**, 2037–2046 (1999).
DOI: 10.1016/S0142-9612(99)00107-6

[5] Wunderlich B., Arakawa T.: Polyethylene crystallized from the melt under elevated pressure. Journal of Polymer Science Part A: General Papers, **2**, 3697–3706 (1964).
DOI: 10.1002/pol.1964.100020828

[6] Rees D. V., Bassett D. C.: Origin of extended-chain lamellae in polyethylene. Nature, **219**, 368–370 (1968).
DOI: 10.1038/219368a0

[7] Ivan'kova E. M., Myasnikova L. P., Marikhin V. A., Baulin A. A., Volchek B. Z.: On the memory effect in UHMWPE nascent powders. Journal of Macromolecular Science Part B: Physics, **40**, 813–832 (2001).
DOI: 10.1081/MB-100107563

[8] Egorov V. M., Ivan'kova E. M., Marikhin V. A., Myasnikova L. P., Drews A.: On fine structure of nascent UHMWPE reactor powders. Journal of Macromolecular Science Part B: Physics, **41**, 939–956 (2002).
DOI: 10.1081/MB-120013075

[9] Uehara H., Kanamoto T., Kawaguchi A., Murakami S.: Real-time X-ray diffraction study on two-stage drawing of ultra-high molecular weight polyethylene reactor powder above the static melting temperature. Macromolecules, **29**, 1540–1547 (1996).
DOI: 10.1021/ma951222y

[10] Waddon A. J., Keller A.: A temperature window of extrudability and reduced flow resistance in high-molecular-weight polyethylene; Interpretation in terms of flow-induced mobile hexagonal phase. Journal of Polymer Science Part B: Polymer Physics, **28**, 1063–1073 (1990).
DOI: 10.1002/polb.1990.090280706

[11] Kolnaar J. W. H., Keller A.: A temperature window of reduced flow resistance in polyethylene with implications for melt flow rheology: 1. The basic effect and principal parameters. Polymer, **35**, 3863–3874 (1994).
DOI: 10.1016/0032-3861(94)90269-0

[12] Kolnaar J. W. H., Keller A.: A temperature window of reduced flow resistance in polyethylene with implications for melt flow rheology: 2. Rheological investigations in the extrusion window. Polymer, **36**, 821–836 (1995).
DOI: 10.1016/0032-3861(95)93114-2

[13] Kolnaar J. W. H., Keller A.: A temperature window of reduced flow resistance in polyethylene with implications for melt flow rheology: 3. Implications for flow instabilities and extrudate distortion. Polymer, **38**, 1817–1833 (1997).
DOI: 10.1016/S0032-3861(96)00707-0

[14] Kolnaar J. W. H., Keller A.: A singularity in the melt flow of polyethylene with wider implications for polymer melt flow rheology. Journal of Non-Newtonian Fluid Mechanics, **69**, 71–98 (1997).
DOI: 10.1016/S0377-0257(97)00017-7

[15] Keller A., Hikosaka M., Rastogi S., Toda A., Barham P. J., Goldbeck-Wood G.: An approach to the formation and growth of new phases with application to polymer crystallization: Effect of finite size, metastability, and Ostwald's rule of stages. Journal of Materials Science, **29**, 2579–2604 (1994).
DOI: 10.1007/BF00356806

[16] Keller A., Hikosaka M., Rastogi S., Toda A., Barham P. J., Goldbeck-Wood G., Windle A. H., Thomas E. L., Bassett D. C.: The size factor in phase transitions: Its role in polymer crystal formation and wider implications. Philosophical Transactions of the Royal Society of London, Series A, **348**, 3–17 (1994).
DOI: 10.1098/rsta.1994.0077

[17] Keller A., Hikosaka M., Rastogi S.: The role of metastability in phase transformations: New pointers through polymer mesophases. Physica Scripta, **66**, 243–247 (1996).
DOI: 10.1088/0031-8949/1996/T66/045

[18] Hikosaka M., Rastogi S., Keller A., Kawabata H.: Investigations on the crystallization of polyethylene under high pressure: Role of mobile phases, lamellar thickening growth, phase transformations, and morphology. Journal of Macromolecular Science Part B: Physics, **31**, 87–131 (1992).
DOI: 10.1080/00222349208215459

[19] Hikosaka M., Okada H., Toda A., Rastogi S., Keller A.: Dependence of the lamellar thickness of an extended-chain single crystal of polyethylene on the degree of supercooling and the pressure. Journal of the Chemical Society, Faraday Transactions, **91**, 2573–2579 (1995).
DOI: 10.1039/FT9959102573

[20] Hikosaka M., Amano K., Rastogi S., Keller A.: Lamellar thickening growth of an extended chain single crystal of polyethylene. 1. Pointers to a new crystallization mechanism of polymers. Macromolecules, **30**, 2067–2074 (1997).
DOI: 10.1021/ma960746a

[21] Hikosaka M., Amano K., Rastogi S., Keller A.: Lamellar thickening growth of an extended chain single crystal of polyethylene (II): ΔT dependence of lamellar thickening growth rate and comparison with lamellar thickening. Journal of Materials Science, **35**, 5157–5168 (2000).
DOI: 10.1023/A:1004804420369

[22] Rastogi S., Hikosaka M., Kawabata H., Keller A.: Role of mobile phases in the crystallization of polyethylene. Part 1. Metastability and lateral growth. Macromolecules, **24**, 6384–6391 (1991).
DOI: 10.1021/ma00024a003

[23] Cheng S. Z. D.: Phase transitions in polymers: The role of metastable states. Elsevier, Amsterdam (2008).

[24] Somani R. H., Yang L., Zhu L., Hsiao B. S.: Flow-induced shish-kebab precursor structures in entangled polymer melts. Polymer, **46**, 8587–8623 (2005).
DOI: 10.1016/j.polymer.2005.06.034

[25] van Bilsen H. M. M., Fischer H., Kolnaar J. W. H., Keller A.: A temperature window of reduced flow resistance in polyethylene: In situ WAXS. Macromolecules, **28**, 8523–8527 (1995).
DOI: 10.1021/ma00129a009

[26] Tashiro K., Sasaki S., Kobayashi M.: Structural investigation of orthorhombic-to-hexagonal phase transition in polyethylene crystal: The experimental confirmation of the conformationally disordered structure by X-ray diffraction and infrared/raman spectroscopic measurements. Macromolecules, **29**, 7460–7469 (1996).
DOI: 10.1021/ma960333+

[27] Rastogi S., Kurelec L., Lemstra P. J.: Chain mobility in polymer systems: On the borderline between solid and melt. 2. Crystal size influence in phase transition and sintering of ultrahigh molecular weight polyethylene via the mobile hexagonal phase. Macromolecules, **31**, 5022–5031 (1998).
DOI: 10.1021/ma980261h

[28] Narh K. A., Keller A.: Differences in melt extrusion behaviour between ultra-high molecular weight polyethylene powder and a dried gel. Journal of Materials Science Letters, **10**, 1301–1303 (1991).
DOI: 10.1007/BF00722641

[29] Rastogi S.: Role of metastable phases in polymer crystallization; Early stages of crystal growth. in 'Polymer crystallization: Observations, concepts, and interpretations' (eds. Reiter G., Sommer J-U.) Springer, Berlin, Vol 606, 17–47 (2003).

[30] Hikosaka M., Tsukijima K., Rastogi S., Keller A.: Equilibrium triple point pressure and pressure-temperature phase diagram of polyethylene. Polymer, **33**, 2502–2507 (1992).
DOI: 10.1016/0032-3861(92)91130-T

[31] Chan C-K., Gao P.: A phenomenological model for the viscosity reductions in blends of HMMPE containing a small quantity of thermotropic liquid crystalline copolyester HBA/HQ/SA. Polymer, **46**, 8151–8156 (2005).
DOI: 10.1016/j.polymer.2005.06.095

[32] Chen J-F., Yi L., Zhou Y-C., Zhou E-L.: High resolution transmission electron microscopy studies on nano-sized crystals of polyethylene and polypropylene (in Chinese). Chemical Journal of Chinese, **25**, 966–970 (2004).

eXPRESS Polymer Letters Vol.5, No.8 (2011) 685–697
Available online at www.expresspolymlett.com
DOI: 10.3144/expresspolymlett.2011.67

Time and temperature effects on Poisson's ratio of poly(butylene terephthalate)

S. Pandini[1*], *A. Pegoretti*[2]

[1]Department of Mechanical and Industrial Engineering and INSTM Research Unit, University of Brescia, via Branze 38, 25133, Brescia, Italy
[2]Department of Materials Engineering and Industrial Technologies and INSTM Research Unit, University of Trento, via Mesiano 77, 38123, Trento, Italy

Received 26 November 2010; accepted in revised form 2 February 2011

Abstract. The viscoelastic nature of the Poisson's ratio of a semicrystalline poly (butylene terephthalate) is highlighted by investigating its dependence on time, temperature and strain rate, under two types of loading conditions: i) constant deformation rate tests, in which the transverse strain is measured in tensile ramps at various temperatures and at two strain rates; and ii) constant deformation tests, in which, under a constant axial deformation, the transverse strain is measured as a function of time in isothermal experiments performed at various temperatures. In both testing configurations, axial and transverse deformations are measured by means of a biaxial contact extensometer, and a correction procedure is adopted in order to compensate the lateral penetration of the extensometer knives. Poisson's ratio displays the typical features of a retardation function, increasing with time and temperature, and decreasing with strain rate. This behaviour has been compared to that of simultaneously measured relaxation modulus.

Keywords: *material testing, mechanical properties, viscoelasticity, Poisson's ratio*

1. Introduction

In the infinitesimal deformation of an idealized purely elastic material, Poisson's ratio is a material constant, defined for an uniaxial stress state as the negative ratio between the deformation normal to the loading axis and the axial imposed strain.

For viscoelastic solids, as in the case of polymers, the lateral contraction coupled to the infinitesimal axial extension exhibits a time and temperature dependent behaviour. The Poisson's ratio of viscoelastic materials cannot thus be regarded as a constant parameter, but as a time-dependent material function, deserving a proper description that encompasses the dependence on time, or equivalently on frequency and strain rate, on temperature and on materials mechanical history.

Poisson's ratio of polymeric materials can thus be thought in the framework of linear viscoelasticity as one of the various viscoelastic response functions, but its determination can involve more complexity [1–3]. In fact, relaxation moduli and creep compliances are usually determined in conditions that allow an easy description of a time dependent correlation between stress and strain (i.e. stress relaxation tests, in which the axial strain is kept constant, and creep tests, in which the stress is constant). On the other hand, in the case of Poisson's ratio, a time dependent correlation has to be established between two strains and a stress generating one of them. As it was underlined by theoretical studies [1, 3–4], when investigating Poisson's ratio time dependence, it is of primary importance to provide a proper

*Corresponding author, e-mail: stefano.pandini@ing.unibs.it

definition of Poisson's ratio as a viscoelastic function and a clear indication of its evaluation conditions. The importance of this aspect is often neglected [1], although the obtained results are shown to depend on testing conditions [3].

In spite of the time dependent behaviour of polymers, and due to considerable experimental difficulties, Poisson's ratio of polymeric materials is often assumed as a constant, or, occasionally, defined for values corresponding to glassy and rubbery equilibrium conditions. In both cases its viscoelastic nature is completely neglected [1]. Nevertheless, it was shown that only in few cases the assumption of a constant Poisson's ratio can be reasonably considered valid [2, 4], and that neglecting its time and temperature dependence may lead to predicting models markedly deviating from the experimental observations [5–7]. More detailed information on the viscoelastic behaviour of Poisson's ratio is therefore important not only in principle [8–10], but also for practical reasons. In fact, it would allow us to interconvert material functions [1], to refine computational methods [2], to reduce the number of required experimental parameters to fit analytical models [8], to better estimate the effects of the so called Poisson's strains, originating from misfits in Poisson's ratio of joined materials [1].

So far, only few trials have been attempted to comprehensively measure and describe the viscoelastic nature of Poisson's ratio. In a review article, Tschoegl *et al.* [1] summarize the main results concerning the measurement and the prediction of viscoelastic Poisson's ratio, and also give a critical perspective on the problems regarding its determination.

A viscoelastic Poisson's ratio can be experimentally evaluated following two procedures; a so called 'direct' measurement, which involves the measurement of the transverse and axial deformations of the tested specimen; and a so called 'indirect' measurement, where, on the basis of the linear viscoelasticity, Poisson's ratio is calculated from the measurement of two other material's time dependent parameters. This latter approach has been proven to be a difficult path, since requiring a very accurate and precise knowledge of the time dependence of the starting functions [11].

Direct measurements of Poisson's ratio has been carried out on polymeric materials by different types of experiments, in which the axial deformation was applied through a constant rate loading ramp [12–15], under a constant load (creep) [13, 16–17], under constant strain (stress relaxation) [10, 14, 18], or under sinusoidal loading-unloading (dynamic-mechanical analysis) [19–21]. An accurate measurement of the transverse strains is of crucial importance and various techniques have been employed, such as optical methods (i.e. Moirè interferometry [10, 17–18] and video extensometry [13, 16]), bonded strain gages [19–20] and biaxial contact extensometers [14–15, 21].

Poisson's ratio of polymeric materials is generally reported as increasing with time (Lu *et al.* on poly (methylmethacrylate) (PMMA) [10], di Landro and Pegoraro on poly (etherimide) (PEI) [18]), temperature (Tcharkhtchi on epoxy resins [15]), and strain (Steinberger *et al*. on polypropylene (PP) [13]; Litt and Torp on polycarbonate (PC) [22]). In a work on epoxy resins we have also reported Poisson's ratio as increasing with time, temperature and strain, and decreasing with strain rate [14]. Moreover, a decreasing trend has been reported for the complex Poisson's ratio with frequency under dynamic conditions (Kästner and Pohl on PMMA [23]; Caracciolo and coworkers on poly(vinylchloride) (PVC) [19–20]; Arzoumanidis and Liechti on a neat urethane adhesive (Ashland) [21]; Pritz, by indirect methodology, on rubbery materials and PMMA [24]).

The results are consistent to what predicted by analytical approaches, which describe the viscoelastic Poisson's ratio following an increasing trend with time [2, 4, 8], featuring the typical trend of a retardation process that can be approached as a transverse creep compliance [25]. Nevertheless, in his studies on auxeticity, Lakes depicts a vaster framework and suggests that for structured materials a monotonic dependence of Poisson's ratio cannot be assumed a priori [26].

In the present paper, an experimental investigation of the viscoelastic features of the Poisson's ratio of a semicrystalline material, poly (butylene terephthalate), PBT, is attempted under constant strain rate and constant strain conditions. The measurements are carried out by means of a biaxial contact extensometer and a procedure is proposed in order

to minimize the effects of the extensometer on the measured transverse strains. Aim of the work is to provide a description of the effects of time, strain rate and temperature on the viscoelastic Poisson's ratio.

2. Experimental

2.1. Material and preliminary characterization

Injection moulded PBT dumb-bell specimens (ISO 527 type 1A; gauge length: 80 mm; cross-section: 4×10 mm) were kindly supplied by Radici Novacips SpA (Villa d'Ogna, Bergamo, Italy). All specimens were treated for 3 h at 190°C under vacuum and slowly cooled in the oven in order to release thermal stresses and uniform the thermal history. In order to detect possible anisotropic effects on the mechanical behaviour of the tensile bars, cubic specimens were machined from the dumb-bell central region and tested under compression along the *x*, *y* and *z* axes (i.e. through specimen length, width and thickness, respectively). On an interval of compressive strains ranging up to 0.6 no significant dependence of the mechanical behaviour on the loading directions was detected.

Differential scanning calorimetry (DSC) analyses were carried out by a Mettler DSC-30 calorimeter (Mettler Toledo, Zürich, Switzerland) at a heating rate of 10°C/min in a nitrogen flux of about 100 ml/min. Tests were performed on specimens of about 15 mg machined from the gauge length of the dumb-bell specimens. From DSC measurements a glass transition temperature (T_g) of 47°C, a melting point (T_m) of 220°C and a crystallinity content (X_c) of 38% were determined. The cristallinity percentage was assessed by integrating the normalized area under the melting endothermal peak and rating the heat involved to the reference value of 100% crystalline polymer, corresponding to 145 J/g [27].

Dynamic mechanical thermal analysis (DMTA) experiments were performed by means of an MkII Polymer Laboratories DMTA testing-machine. Tests were carried out under bending mode on rectangular bars (12×5×2 mm) machined from the gauge length of a dumb-bell specimen at the test frequencies of 0.3, 1, 3, 10, 30 Hz.

The region of linear viscoelastic behaviour was evidenced on isochronous stress-strain curves obtained by stress relaxation tests performed at axial strain levels in the range from 0.001 to 0.02. Mechanical tests were performed on PBT dumb-bell specimens by means of an electromechanical testing machine (Instron, model 4502, Instron, Norwood, Massachusetts, USA), controlling the level of strain by an axial extensometer (Instron, model 2640, Instron, Norwood, Massachusetts, USA). The deformation was applied at a constant crosshead speed (corresponding to a strain rate of = 0.003 s^{-1}) and then kept constant for at least 30 min. The tests were performed at 30°C and at 70°C (i.e. below and above the glass transition temperature) in a thermostatic chamber (Instron, model 3199, Instron, Norwood, Massachusetts, USA), permitting a temperature control within ±1°C.

2.2. Viscoelastic Poisson's ratio evaluation

The dependence of Poisson's ratio on time, temperature and strain rate was experimentally evaluated under various testing conditions. In particular, as schematically represented in Figure 1, two different loading histories were investigated: in constant deformation rate (CDR) tests the specimen was subjected to a tensile ramp at a fixed strain rate; in constant deformation tests (REL) a constant tensile axial deformation was applied, such as in stress relaxation tests. In both CDR and REL tests, the input (axial deformation, ε_{AX}) and output (transverse deformation, ε_{TRANS}, and stress, σ) variables were simultaneously recorded as a function of time. The experiments were performed with an Instron 4502 electromechanical testing machine (see above), operating in displacement control. The tests were performed in a thermostatic chamber (see above) at various temperatures between 20 and 100°C.

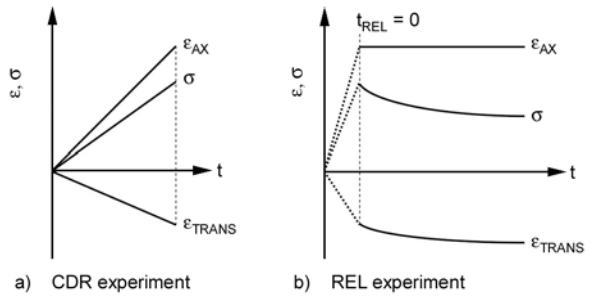

Figure 1. Schematic representation of input (axial deformation, ε_{AX}) and output (stress, σ; transverse deformation, ε_{TRANS}) variables in a) constant deformation rate (CDR) experiments and b) constant deformation (REL) experiments

The axial and transverse deformations were evaluated by means of a biaxial clip-on extensometer (Instron, model 2620-613, Instron, Norwood, Massachusetts, USA) mounted on the specimen, as represented in Figure 2. The extensometer is a self-standing clip-on device, weighing about 300 g, which is symmetrically distributed on the specimen, thanks to the peculiar shape of the device. No other supports are required to sustain the device, since visual inspection during the test has never detected distortion of the specimen at the temperatures explored. In order to assure self-standing and gripping, the extensometer exerts on the lateral sides of the specimen a certain force, quantified by the producer to a nominal value of 22 N [http://www.instron.com/wa/library/StreamFile.aspx?doc=290]. This generates a local transverse stress of about 0.5 MPa, roughly evaluated by dividing the gripping force over the gauge side cross-section defined by the specimen thickness multiplied for the distance between the knives. The value is at least one order of magnitude lower than the lowest axial stress measured in constant deformation experiments, and the effect of this transverse stress is considered to have a minor contribution to the overall stress state with respect to the axial tensile stress, but leads anyway to a continuous penetration of the extensometer knives in the specimen (creep penetration). The transverse displacement measured during the tests originates thus both from the material contraction (ruled by the Poisson's ratio) and from the lateral creep exerted by the extensometer. In order to compensate the data for this undesired effect, the amount of creep penetration of the extensometer was evaluated separately on undeformed specimens as a function of time at various temperatures and then subtracted from the total transverse displacement recorded.

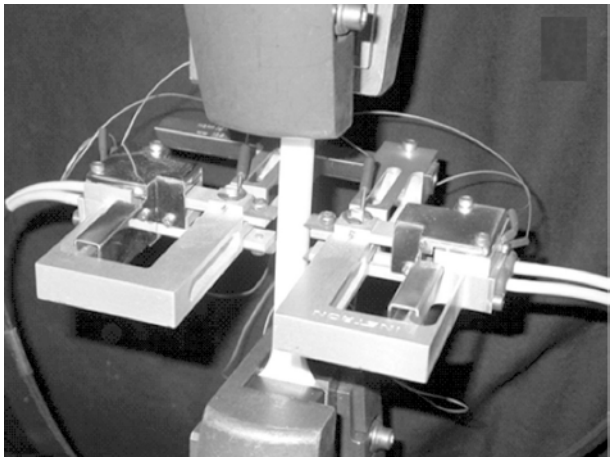

Figure 2. Experimental set-up employed for the Poisson's ratio measurement, in adoption of a clip-on biaxial extensometer (Instron mod. 2620) mounted on a PBT dumb-bell specimen

The longitudinal deformation, ε_{AX}, was evaluated as shown by Equation (1):

$$\varepsilon_{AX} = \frac{\Delta L_{AX}}{L_{AX,0}} \tag{1}$$

where ΔL_{AX} represents the axial displacement measured by the extensometer and $L_{AX,0}$ the longitudinal initial gauge length (12.5 mm).

The transverse deformation, ε_{TRANS}, has been measured across the specimen width, and evaluated as shown by Equation (2):

$$\varepsilon_{TRANS} = \frac{\Delta L_{TRANS} - \Delta L_{PENETRATION}}{L_{TRANS,0}} \tag{2}$$

where, for a given time, ΔL_{TRANS} represents the transverse displacement recorded by the extensometer and $\Delta L_{PENETRATION}$ the extensometer penetration, while $L_{TRANS,0}$ is the specimen initial width.

The transverse deformation was measured across the width of the specimen, since permitting to deal with larger transverse displacement signals with respect to those measured when the transverse deformation measured across the specimen thickness. This testing geometry helps in minimizing the contribution of dimensional defects of the specimens and of the imprecision in the compensation for the transverse extensometer penetration. The Poisson's ratios described in this paper always refer to such testing direction, although, due to the overall material isotropy, it is expected that very similar results could be obtained if lateral contraction would be measured through the thickness.

In constant deformation rate (CDR) tests the specimen was subjected to a tensile loading ramp at a constant strain rate. Aim of the CDR tests is to provide a description of the effects of temperature and strain rate on the Poisson's ratio evaluated at short times and at small axial strains. We will refer to the values measured under these testing conditions as Poisson's ratio, but still bearing in mind the indication of Hilton and Yi [4] and Tschoegl *et al.* [1], who prefer the term lateral contraction ratio over Poisson's ratio, for the data measured in ramp tests. The tests were performed at two crosshead speeds,

corresponding to strain rates of 0.003 and 0.05 s^{-1}, and at various temperatures, in the range between –20 and 100°C, while the maximum strain never exceeded 0.01. The Poisson's ratio values measured under these experimental conditions will be labelled as ν_{CDR}, and calculated by Equation (3) as the negative ratio between the slopes of the transversal deformation and axial deformation curves as function of the applied load, F:

$$\nu_{CDR} = -\frac{\frac{d\varepsilon_{TRANS}}{dF}}{\frac{d\varepsilon_{AX}}{dF}} \quad (3)$$

on the region of linear proportionality between stress and strain. The evaluation takes the advantage of the linear dependence of the axial and transverse deformations on the applied load on an adequately large portion of the axial strain values (i.e. for ε_{AX} at least up to 0.03), and is proposed accordingly with standardized procedures for the evaluation of short-time tensile properties of plastics (ASTM D 638). Further, it has to be remarked that, when force and the two strains can be described by functions linearly increasing with time from a zero value at $t = 0$, the above formula provides results coincident with those that can be obtained by applying Equation (4) proposed by Tschoegl *et al.* [1] for the evaluation of the lateral contraction ratio in constant rate of strain measurements:

$$\nu(t) = \frac{1}{t}\int_0^t \nu_{rate}(u)du \quad (4)$$

where ν_{rate} can be defined by Equation (5):

$$\nu_{rate} = -\frac{\frac{d\varepsilon_{TRANS}}{dt}}{\frac{d\varepsilon_{AX}}{dt}} = -\frac{\frac{d\varepsilon_{TRANS}}{dF}}{\frac{d\varepsilon_{AX}}{dF}} \quad (5)$$

and, for a given strain rate, it displays a constant value on the linear stress *vs*. strain region.

Young's modulus was also measured under the same test conditions.

Constant deformation tests (REL) were performed applying a constant deformation ($\varepsilon_{AX,REL}$) for at least 30 min and measuring the transverse deformation as a function of time. These tests were carried out for two values of the constant axial strain, $\varepsilon_{AX,REL}$ = 0.005 and 0.010, applied at a strain rate of 0.003 s^{-1}, and at various temperatures in the range between 30 and 60°C. The time dependence of Poisson's ratio was assessed by measuring the changes in the specimen width after the axial deformation was applied and maintained constant. This type of test follows the typical methodology of a stress relaxation test, and thus the Poisson's ratio measured in these conditions is labelled as ν_{REL}, and evaluated according to Equation (6):

$$\nu_{REL} = -\frac{\varepsilon_{TRANS}(t)}{\varepsilon_{AX,REL}} \quad (6)$$

where ε_{TRANS} is the time-dependent transverse deformation measured for the applied longitudinal deformation $\varepsilon_{AX,REL}$. Since the axial deformation is constant in time, this type of test configuration permits an easy but rigorous calculation of the viscoelastic Poisson's ratio, thus avoiding the otherwise complicated mathematical treatments required for other deformational histories and involving Laplace transforms between viscoelastic variables [1]. Relaxation modulus was concurrently measured in this part of the test and will be reported as E_{REL}. The results were then plotted as a function of $t_{REL} = t - t_0$, where t represents the test time and t_0 the time at which the constant deformation for the relaxation experiment is applied.

3. Results and discussion

3.1. Preliminary material characterization

Figure 3 reports the traces of the storage modulus (E') and loss factor (tanδ) as a function of temperature at various frequencies. The figure shows a glass transition temperature region between 45 and 70°C, depending on the frequency, as evaluated in

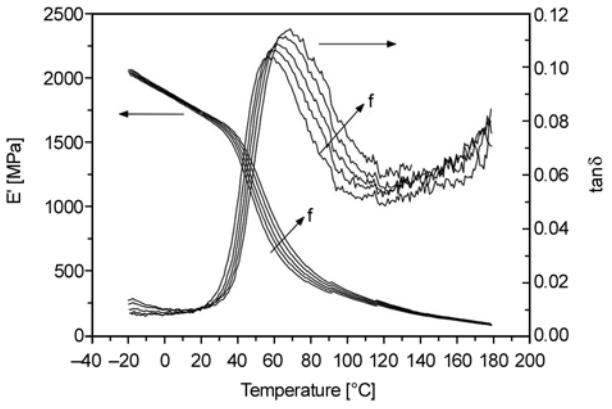

Figure 3. E' and tanδ traces from the DMTA test performed on PBT at various frequencies (f = 0.3, 1, 3, 10, 30 Hz)

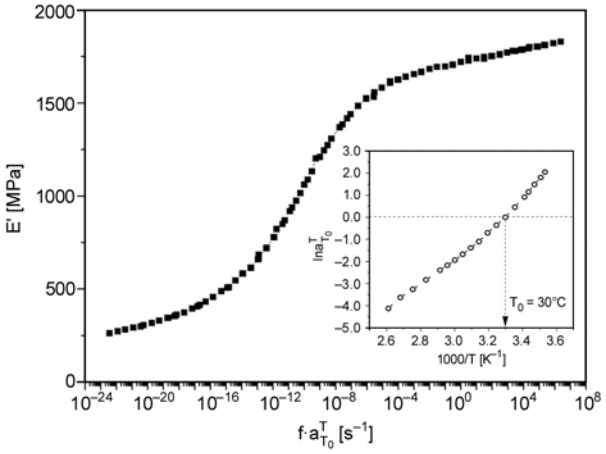

Figure 4. *E′* master curve as a function of reduced frequency at a reference temperature, T_0 = 30°C; insert: shift factors evaluated by best superposition of isothermal *E′ vs*. frequency curves

correspondence to the region where the storage modulus traces present an inflection point and the tanδ traces show their maximum. According to a time-temperature reduction scheme, isothermal *E′ vs*. frequency curves enabled us to build a storage modulus master curve, represented in Figure 4 for a reference temperature T_0 = 30°C. The logarithm of the shift factors, $a_{T_0}^T$, adopted for the master curve construction are presented as an insert in Figure 4, as a function of 1000/T, where T is the absolute temperature. The master curve indicates that the transition zone of the storage modulus spans over a frequency range of 7–8 decades, ranging i.e. from about 10^{-15} Hz up to about 10^{-8} Hz at this reference temperature.

The extent of the linear viscoelastic region was assessed on isochronous stress-strain curves obtained from stress relaxation tests performed at 30 and at 70°C, i.e. below and above the glass transition temperature. The isochronous curves for these two temperatures are reported at various instants in Figure 5a and b, respectively. Independently from time, the curves at 30°C show a linear trend for axial deformations up to 0.01, whereas at higher deformations an evident deviation from linearity can be detected. On the other hand, a clear threshold value for the linear viscoelastic behaviour is more difficult to be identified in the experiments performed at 70°C. Anyway, the results seem to indicate that at this temperature the linear viscoelastic region extends up to an axial strain level between 0.005 and 0.01. In consideration of these results the evaluation of Poisson's ratio in constant deformation experiments was carried out both at an axial strain $\varepsilon_{AX,REL}$ = 0.005 and at $\varepsilon_{AX,REL}$ = 0.01.

3.2. Viscoelastic Poisson's ratio effect and correction of the transverse displacement

Experimental input and output of CDR experiments are reported in Figures 6a and b, as measured in tests performed at a strain rate of 0.003 s^{-1} at some of the investigated temperatures. Figure 6a represents the time evolution of the stress during the tensile ramp test and its well-known dependence on temperature. In Figure 6b the reading of the transverse extensometer is reported in terms of an apparent transverse strain, i.e. the net transverse displacement, ΔL_{TRANS}, divided by the specimen width, named apparent since at this stage it still comprises the contribution due to the extensometer knives penetration. Such a representation of the lateral contraction effects, in which also the overall transverse displacement can be easily deduced (ε_{TRANS} =

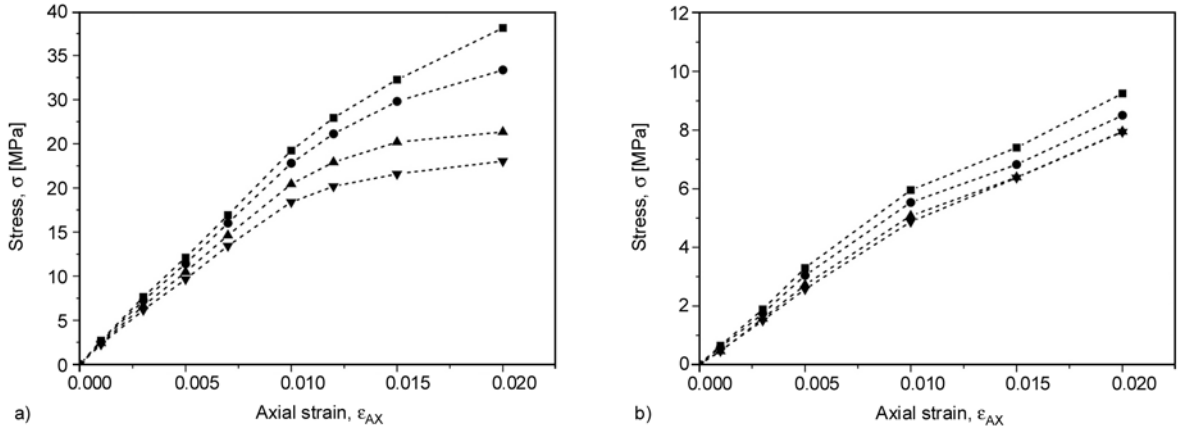

Figure 5. PBT isochronous stress *vs*. strain curves at a) 30°C and b) 70°C for various instants: 10 s (■); 100 s (●); 1000 s (▲); 1 h (▼)

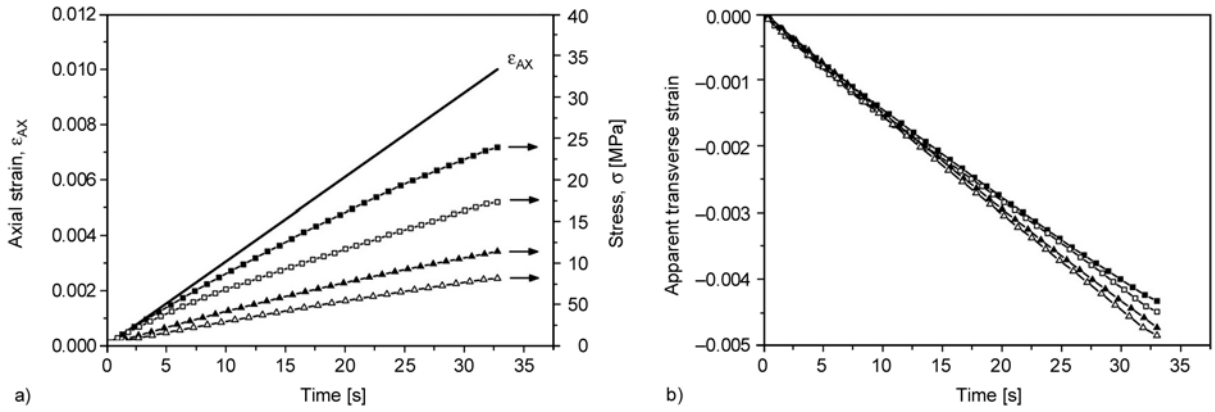

Figure 6. Time evolution of a) axial strain, ε_{AX}, and stress, σ, and b) apparent transverse strain in CDR experiments for an axial strain rate of 0.003 s^{-1} at various temperatures: 20°C (■); 30°C (□); 50°C (▲); 60°C (Δ)

–0.001 corresponds to a transverse contraction of 10 μm), may help the comparison of the transverse displacement data with the data regarding the extensometer penetration, which will be reported later.

The opposite signs exhibited by axial and transverse strains indicate that the application of a tensile deformation leads to lateral contraction of the specimen, and it is shown that at any given instant, and thus at any given axial strain value, a greater lateral contraction is found as the temperature increases. The total transverse displacement measured within this set of tests is between 40 and 50 μm, depending on the test temperature.

The input and output of constant deformation tests are reported in Figures 7a and b in case of an axial deformation ε_{AX} = 0.01 and at various temperatures. These figures show that the stress relaxation is also accompanied by a continuous lateral contraction process. While the stress relaxation displays the well-known dependence on time and temperature, the transverse strain decreases with time and, at any instant, a greater lateral contraction is found for a higher temperature. Within this set of experiments the change in the net transverse displacement signal during the constant axial strain maintenance is about 5 μm at all temperatures, and it is shown that at high temperatures an overlapping of the curves can occur for long times.

In order to correct the value of the transverse displacement for the concomitant lateral creep of the extensometer knives, this latter term was quantitatively estimated in experiments carried out on undeformed specimens. Figure 8 reports some examples of the knives penetration curves. It can be noted that in the time span of CDR tests (i.e. up to 40 s), the lateral penetration is in any case lower than 0.1 μm, and thus very small in comparison with the transverse displacement recorded during the ramp tests; it is therefore believed that the lateral penetration does not practically affect the lateral contraction ratio evaluated in CDR tests. On the other hand, the knives penetration becomes more important for long times, and within 1800 s a maximum penetra-

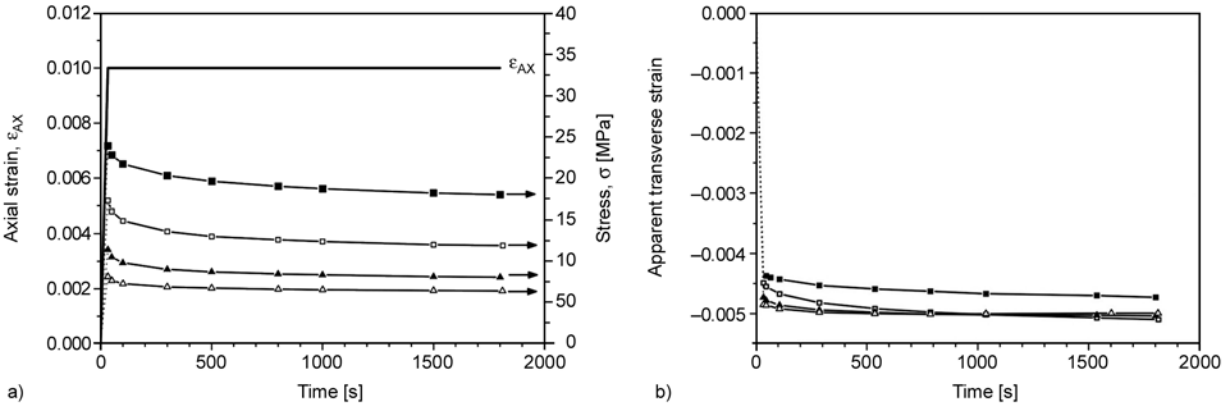

Figure 7. Time evolution of a) axial strain, ε_{AX}, and stress, σ, and b) apparent transverse strain in REL experiments carried out at $\varepsilon_{AX,REL}$ = 0.01 at various temperatures: 20°C (■); 30 °C(□); 50°C (▲); 60°C(Δ)

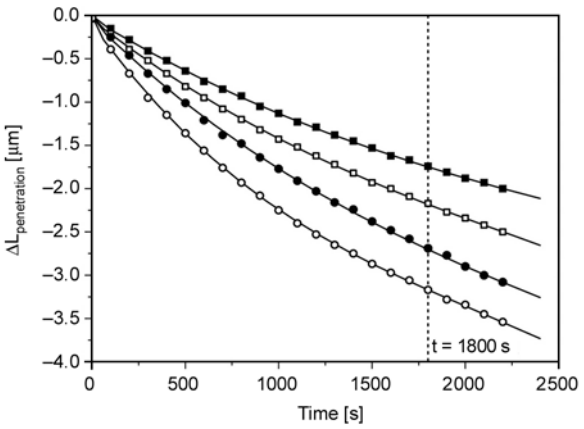

Figure 8. Transverse displacement due to the extensometer lateral penetration measured on an undeformed specimen as a function of time at various temperatures: 30°C (■); 40°C (□); 50°C (●); 60°C (○)

tion of about 1.7 μm is found at 30°C and almost the double at 60°C. These values are not negligable if compared with the transverse displacement variation recorded during REL tests. In fact, at the two temperatures considered, they reach about 30 and 60% of the values measured in REL tests during the constant axial strain maintenance, respectively. This indicates that the compensation of such undesired effect becomes a strict requirement in order to provide a quantitative evaluation of the viscoelastic Poisson's ratio in relaxation tests.

3.3. Constant deformation rate tests

The effects of temperature and strain rate on the short-time Poisson's ratio, ν_{CDR}, were investigated in CDR experiments. The results of the experiments are reported in Figures 9a and b, representing the Poisson's ratio and Young's modulus, respectively, as a function of temperature at two strain rates.

Figure 9a shows that, for both strain rates, the Poisson's ratio increases with temperature. Such dependence can be fitted with a sigmoidal function, extending from a lower plateau value of about 0.41 to an upper plateau value scattered around 0.5, representative of the conditions of constant volume deformation, typical of incompressible materials in the rubbery state. The inflection point of the sigmoidal curves is located for both strain rates at temperatures in the proximity of the PBT glass transition temperature, whereas the upper plateau is approached at about 100°C, i.e. well above T_g. As the strain rate increases, a lower ν_{CDR} value is found for a given temperature, and a shift of the sigmoidal fitting curve to higher temperatures can be observed. Such a shift, if evaluated with reference to the inflection point, is about 10°C for a strain rate increase of about 20 times. The Young's modulus, which is measured in the same experiment, displays a sigmoidal decreasing dependence on temperature, only slightly affected by strain rate. For both strain rates the inflection point of the curves is located at about 40°C, in proximity to that found for the Poisson's ratio measured at the lower strain rate.

It is interesting to compare these results with those previously obtained by this group, under similar experimental methodology, on epoxy resins [14]. A similar sigmoidal dependence on temperature was evidenced for the epoxy systems, but with an inflection point for the Poisson's ratio *vs*. temperature curve occurring 20°C below the inflection point of the simultaneously measured Young's modulus *vs*. temperature curve. Moreover, the upper plateau was approached for deformation temperatures close to the glass transition temperature. Tcharkhtchi *et al.*

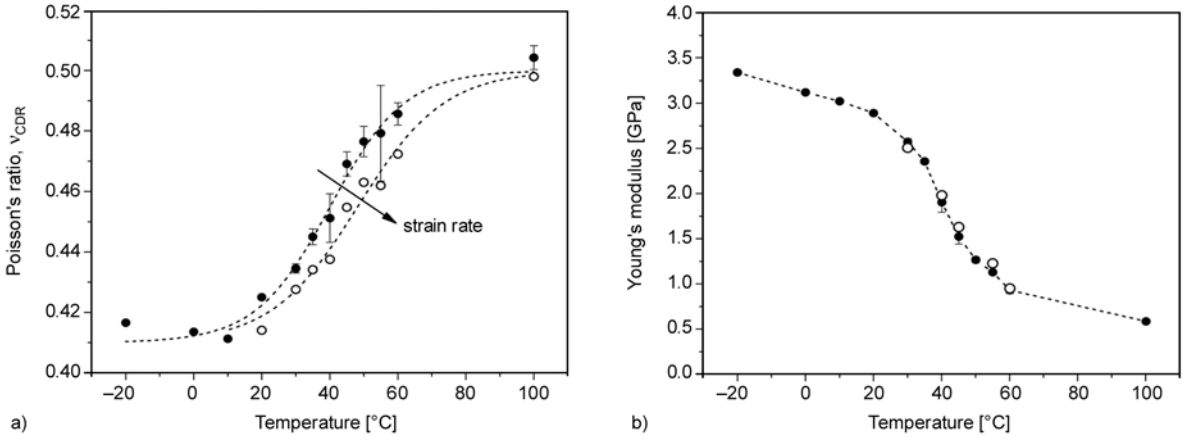

Figure 9. a) Viscoelastic Poisson's ratio, ν_{CDR}, and b) Young modulus for semicrystalline PBT evaluated at different deformation temperatures along a deformation ramp at strain rate of 0.003 s^{-1} (●) and of 0.05 s^{-1} (○)

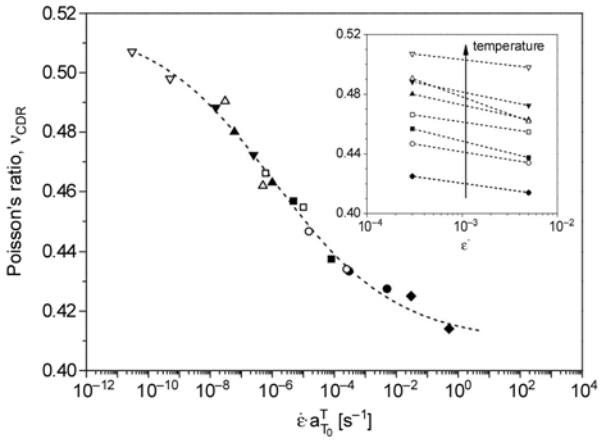

Figure 10. Viscoelastic Poisson's ratio, ν_{CDR}, master curve as function of reduced strain rate at a reference temperature T_0 = 30°C after shifting of the isothermal curves at temperatures: 20°C (♦); 30°C (●); 35°C (○); 40°C (■); 45°C (□); 50°C (▲); 55°C (Δ); 60°C (▼); 100°C (∇); insert: isothermal curves before shifting

[15] provided analogous results on similar epoxy systems. The results here presented for semicrystalline PBT suggest that higher temperatures are required with respect to amorphous materials to display the quasi-constant volume conditions and that the T_g region plays an important role on the transition to such deformational behaviour. This result could be interpreted by considering a mobility hindrance exerted by the coexistence of crystalline and amorphous regions.

By a tentative application of a time–temperature reduction scheme, the isothermal ν_{CDR} data, represented as a function of the strain rate, were rigidly shifted along the strain rate axis until the best superposition was reached. The master curve obtained is presented for a reference temperature T_0 = 30°C in Figure 10. The decreasing (sigmoidal) dependence of the Poisson's ratio on strain rate indicates that as the strain rate decreases the deformation can occur under quasi-constant volume conditions, and, although only qualitatively, the result seems to suggest that for a deformation at 30°C these deformation conditions can be met for very slow strain rates, lower than about 10^{-9} s^{-1}.

3.4. Constant deformation tests

REL tests permitted the investigation of Poisson's ratio dependence on time and temperature, starting from the net transverse displacement signal and correcting it for the extensometer knives penetration. The results obtained are reported in Figure 11a, which displays the Poisson's ratio, ν_{REL}, as a function of the relaxation time, t_{REL}, in terms of isothermal curves measured for an applied axial deformation ε_{AX} = 0.01. For all the investigated temperatures, the viscoelastic Poisson's ratio displays a monotonic increase with time, and, for any given instant, a higher value of the Poisson's ratio is found as temperature increases. The average slope of the curves increases for temperatures up to 40°C, i.e. in the proximity of the glass transition temperature, and decreases again for temperatures above T_g.

The initial part of the curves is characterized by a fairly regular increase, whereas at longer times (t_{REL} longer than approximately 10 min) the isothermal curves tend to overlap, exhibiting a less regular behaviour and the tendency to converge to a value slightly above 0.5, i.e. above the incompressibility conditions. It is important to underline that if the transverse extensometer reading was not corrected, even higher Poisson's ratio values would have been read. In the author's opinion these high Poisson's ratio values have to be interpreted as scattered around 0.5, and affected by inaccuracies related to the correction of transverse deformation for long times and high temperatures. At the same time, it can not be excluded that the upper plateau could be higher than 0.5, due to non-homogeneity on a microstructural scale, already present in the materials (such as crystalline regions below the melting temperature [1] or porosity [28]) or developed during the deformational process (as cavitational effects [29–32], although these should have major importance at deformations higher than those investigated here).

The decrease of stress was simultaneously monitored, permitting an evaluation of the time evolution of the relaxation modulus E_{REL}, which is reported in Figure 11b in terms of isothermal curves for an axial deformation ε_{AX} = 0.01. The well-known dependence on time and temperature is exhibited and it is noteworthy to underline that the steepest decrease is found at T = 40°C.

As previously shown in the evaluation of short-time Poisson's ratio by CDR tests, the glass transition temperature seems to play a relevant role on the PBT viscoelastic Poisson's ratio also even under these loading conditions. Not being directly in possession of data regarding the effect of temperature

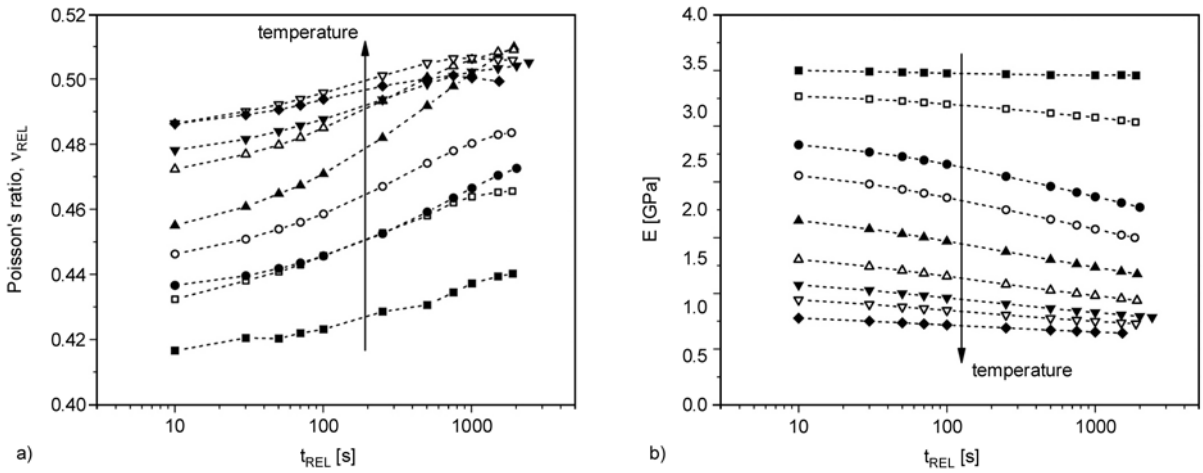

Figure 11. a) Isothermal Poisson's ratio, ν_{REL}, and b) relaxation modulus, E, isothermal curves as a function of relaxation time, t_{REL}, at various temperatures: 0°C (■); 20°C (□); 30°C (●); 35°C (○); 40°C (▲); 45°C (Δ); 50°C (▼); 55°C (∇); 60°C (♦); data obtained for an axial deformation $\varepsilon_{AX,REL} = 0.01$

on relaxation Poisson's ratio of amorphous materials, our results were compared with literature data, which underline some relevant differences between semicrystalline and amorphous polymers. O'Brien *et al.* [17] reported isothermal curves of the viscoelastic so-called lateral contraction ratio for epoxy resins under creep conditions. They evidenced an upper plateau at 0.49 for temperatures approaching the glass transition region, while the simultaneously measured creep compliance still displays an increasing trend. Similar results were obtained on amorphous poly (methylmetacrylate) by the group of Knauss [10]. In both the above-cited works the steepest part of the Poisson's ratio isothermal curve is located at temperatures lower than T_g.

The REL experiments performed at $\varepsilon_{AX} = 0.005$ led to results similar to those obtained at the higher deformation level, although a less regular trend for the isothermal Poisson's ratio *vs*. relaxation time curves was found. This is probably due to the fact that, in the case of a lower axial deformation, the extensometer knives penetration becomes of higher importance with respect to the transverse contraction, and thus an even greater accuracy is required for the data correction.

On the basis of a time-temperature reduction scheme, the ν_{REL} and E_{REL} isothermal curves obtained for the two sets of axial strains were shifted along the time scale, in order to tentatively achieve a master curve representation of the two functions. The master curves obtained are reported in Figures 12a and b, in which the Poisson's ratio and the relaxation modulus, respectively, are plotted as a function of the reduced time for a reference temperature $T_0 = 30$°C; Figure 12b reports also the Poisson's ratio master curve evaluated at $\varepsilon_{AX} = 0.01$ in order to directly compare the time dependence of the two functions.

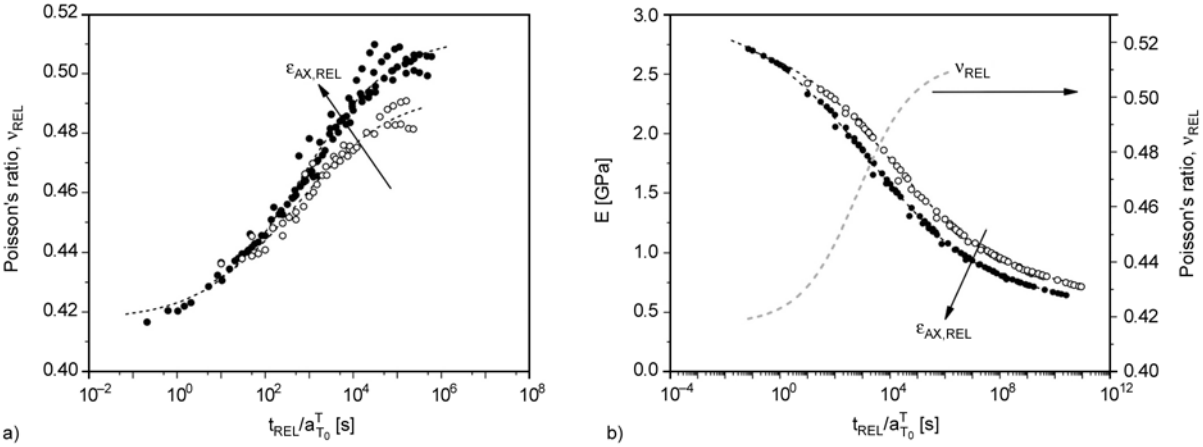

Figure 12. a) Poisson's ratio, ν_{REL}, and b) relaxation modulus, E, master curves as a function of reduced relaxation time at a reference temperature $T_0 = 30$°C for two different axial deformations $\varepsilon_{AX,REL}$: 0.005 (○) and 0.01 (●)

For both axial strain levels, Poisson's ratio shows an increasing trend with time, which can be fitted by a sigmoidal function and can be viewed as a retardation (or delay) process. At this reference temperature the master curve upper plateau seems to be approached at times in the order of 10^6 s and the inflection point is located at about 10^3 s. The applied axial strain seems to marginally affect the time-dependence of the viscoelastic Poisson's ratio, and mainly in the region of longer relaxation times: in fact, although following similar sigmoidal trend, higher Poisson's ratio values can be found for a given instant as the applied strain increases. Also the relaxation modulus master curve seems to be dependent on the applied strain, and lower relaxation moduli are found at the higher strain. Such effect on both viscoelastic functions is interpreted as a typical non-linear viscoelastic effect related to the higher mobility occurring when larger deformations are applied.

Several aspects anyway suggest that the time distribution of the Poisson's ratio master curve here provided, at this stage, should be considered as merely qualitative; these aspects regard i) the different distribution of the Poisson's ratio and of the relaxation modulus as a function of the reduced time scale, and ii) the different shift-factors for the two functions.

In Figure 12b it is shown that, with respect to E_{REL}, the ν_{REL} function displays inflection points occurring at shorter times (the E_{REL} inflection point being at about 10^6 s) and a narrower transition region. This latter is seen to span over 3–4 decades in the case of ν_{REL}, thus on a significantly narrower region with respect to the 7–8 decades transition region exhibited by the simultaneously measured relaxation modulus, and, similarly, by the storage modulus master curve. Since Tschoegl *et al.* [1] claims that the delay times distribution can not be assumed to be identical to that of relaxation and retardation times measured in stress relaxation and creep experiments, such a result can not be regarded as inconsistent. Nevertheless, inspection of literature data does not provide great help in interpreting this effect. A tentative explanation of the peculiar distribution of delay times observed for PBT's ν_{REL} with respect to relaxation times shown by E_{REL} could be based on the different relaxation kinetics of the hydrostatic and deviatoric stress components of the stresses. In fact, it was experimentally proven that bulk relaxation shows a narrower distribution of relaxation times with respect to shear relaxation (Morita *et al.* on poly (isobutyl metacrylate), and Kono *et al.* on poly (isobutylether); both listed in [1]); further, Di Landro and Pegoraro [18] have attributed to the same reason the observed transition of the viscoelastic Poisson's ratio of polyetherimide (PEI) occurring at times shorter than that measured for shear and tensile modulus.

Of more difficult interpretation is the result concerning the different shift factors required for the construction of Poisson's ratio (ν_{CDR} *vs*. strain rate; ν_{REL} *vs*. time) and of the relaxation and storage moduli master curves, as can be seen from their representation as a function of the inverse absolute temperature in Figure 13. The shift factors of the relaxation modulus are not affected by the strain level and exhibit values quite close to those estimated in DMTA tests. The shift factors for the master curves of Poisson's ratio in REL tests also seem to be unaffected by the axial strain, but show a less steep slope with respect to those related to the moduli functions. Finally, the data obtained from the Poisson's ratio measured in CDR experiments, shows an intermediate behavior, exhibiting values close to those measured for the moduli functions for temperature up to 40°C, while a deviation is exhibited for higher temperatures, with a slope similar to that shown by the ν_{REL} set of data. Previous literature data have always shown that the shift factors

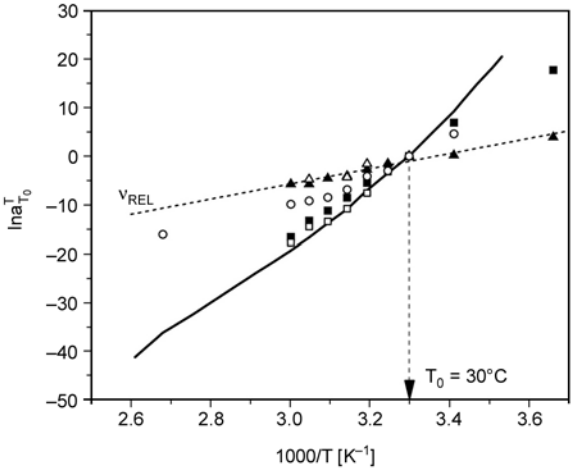

Figure 13. Shift factors employed for the construction of the following master curves: a) storage modulus vs. frequency, b) Poisson's ratio ν_{CDR} *vs*. strain rate, c) Poisson's ratio ν_{REL} *vs*. t_{REL} ($\varepsilon_{AX,REL}$ = 0.005 (▲) and 0.01 (■)) and *E vs*. t_{REL} ($\varepsilon_{AX,REL}$ = 0.005 (Δ) and 0.01 (□))

required for the Poisson's ratio master curve construction are the same as those obtained for other viscoelastic functions [10, 17, 20]. The difference found between master curves distribution and between the related shift factors are effects not fully understood, and that could be tentatively ascribed to an interference due to the contact extensometer. In fact, although the subtraction of the transverse penetration is believed to correct the value of Poisson's ratio in any experimental condition, the presence of additional stress components, locally induced by the lateral clip-on device, cannot be avoided.

4. Conclusions

The viscoelastic dependence of Poisson's ratio on time and temperature was investigated for semicrystalline PBT in tensile ramp tests at constant deformation rate (CDR tests) and in tests in which the axial strain was maintained constant (constant deformation, or REL, tests). The axial and transverse deformations were simultaneously recorded by means of a biaxial clip-on extensometer, and a correction procedure was proposed in order to subtract the lateral penetration of the extensometer knives from the net transverse displacement recorded.

It was shown that PBT Poisson's ratio exhibits viscoelastic features, with values increasing with time and temperature and decreasing with strain rate. The results of CDR tests show that the short-time Poisson's ratio, ν_{CDR}, measured at strain rates in the order of 10^{-3}–10^{-2} s^{-1}, displays a sigmoidal increase with temperature with an upper plateau at about 0.5 (i.e. the constant volume deformation conditions), approached for temperatures well above T_g, in contrast to what was reported for amorphous polymers, which generally reach such deformational behaviour at T_g. Further, for the same temperature a higher ν_{CDR} value is found as the strain rate increases, and a tentative representation of the ν_{CDR} *vs*. strain rate master curve would suggest that, for a reference temperature $T_0 = 30°C$, the upper plateau can be approached for strain rates lower than 10^{-9} s^{-1}.

In REL tests it is shown that stress relaxation is accompanied by a continuous lateral contraction process, which leads to a monotonous increase of Poisson's ratio, ν_{REL}, with time, exhibiting the fastest increase in proximity to the glass transition temperature. The master curve representation of Poisson's ratio, tentatively obtained from the isothermal ν_{REL} curves, qualitatively describes a sigmoidal increasing dependence on the logarithmic reduced time, confirming the nature of viscoelastic Poisson's ratio as a retardation (or delay) process.

References

[1] Tschoegl N. W., Knauss W. G., Emri I.: Poisson's ratio in linear viscoelasticity – A critical review. Mechanics of Time-Dependent Materials, **6**, 3–51 (2002). DOI: 10.1023/A:1014411503170

[2] Hilton H. H.: Implications and constraints of time-independent Poisson ratios in linear isotropic and anisotropic viscoelasticity. Journal of Elasticity, **63**, 221–251 (2001). DOI: 10.1023/A:1014457613863

[3] Lakes R. S., Wineman A.: On Poisson's ratio in linearly viscoelastic solids. Journal of Elasticity, **85**, 45–63 (2006). DOI: 10.1007/s10659-006-9070-4

[4] Hilton H. H., Yi S.: The significance of (an)isotropic viscoelastic Poisson ratio stress and time dependencies. International Journal of Solids and Structures, **35**, 3081–3095 (1998). DOI: 10.1016/S0020-7683(97)00357-0

[5] Delin M., Rychwalski W. R., Kubát J. M., Kubát J.: Volume changes during stress relaxation in polyethylene. Rheologica Acta, **34**, 182–195 (1995). DOI: 10.1007/BF00398438

[6] Bertilsson H., Delin M., Kubát J., Rychwalski W. R., Kubát M. J.: Strain rates and volume changes during short-term creep of PC and PMMA. Rheologica Acta, **32**, 361–369 (1993). DOI: 10.1007/BF00435082

[7] Tsou A. H., Greener J., Smith G. D.: Stress relaxation of polymer films in bending. Polymer, **36**, 949–954 (1995). DOI: 10.1016/0032-3861(95)93593-B

[8] Drozdov A. D.: Volume changes in glassy polymers. Archive of Applied Mechanics, **68**, 689–710 (1998). DOI: 10.1007/s004190050197

[9] Popelar C. F., Liechti K. M.: A distortion-modified free volume theory for nonlinear viscoelastic behavior. Mechanics of Time-Dependent Materials, **7**, 89–141 (2003). DOI: 10.1023/A:1025625430093

[10] Lu H., Zhang X., Knauss W. G.: Uniaxial, shear, and Poisson relaxation and their conversion to bulk relaxation: Studies on poly(methyl methacrylate). Polymer Engineering and Science, **37**, 1053–1064 (1997). DOI: 10.1002/pen.11750

[11] Sane S. B., Knauss W. G.: The time-dependent bulk response of poly (methyl methacrylate). Mechanics of Time-Dependent Materials, **5**, 325–343 (2001). DOI: 10.1023/A:1012517421899

[12] Okoli O. I., Smith G. F.: The effect of strain rate and fibre content on the Poisson's ratio of glass/epoxy composites. Composite Structures, **48**, 157–161 (2000). DOI: 10.1016/S0263-8223(99)00089-6

[13] Steinberger R., Jerabek M., Major Z., Lang R. W.: Determination of time dependent Poisson's ratio vales of polypropylene in monotonic and creep tensile experiments. in: 'Proceedings of the 13th International Conference on Deformation, Yield and Fracture of Polymers, Kerkrade, The Netherlands' 381–384 (2006).

[14] Pandini S., Pegoretti A.: Time, temperature, and strain effects on viscoelastic Poisson's ratio of epoxy resins. Polymer Engineering and Science, **48**, 1434–1441 (2008). DOI: 10.1002/pen.21060

[15] Tcharkhtchi A., Faivre S., Roy L. E., Trotignon J. P., Verdu J.: Mechanical properties of thermosets. Journal of Materials Science, **31**, 2687–2692 (1996). DOI: 10.1007/BF00687301

[16] Jazouli S., Luo W., Brémand F., Vu-Khanh T.: Nonlinear creep behavior of viscoelastic polycarbonate. Journal of Materials Science, **41**, 531–536 (2006). DOI: 10.1007/s10853-005-2276-1

[17] O'Brien D. J., Sottos N. R., White S. R.: Cure-dependent viscoelastic Poisson's ratio of epoxy. Experimental Mechanics, **47**, 237–249 (2007). DOI: 10.1007/s11340-006-9013-9

[18] Di Landro L., Pegoraro M.: Determinazione delle funzioni viscoelastiche di materiali polimerici (in Italian). in: 'Proceedings of IV National Congress AIMAT, Cagliari, Italy' 663–668 (1998).

[19] Caracciolo R., Giovagnoni M.: Frequency dependence of Poisson's ratio using the method of reduced variables. Mechanics of Materials, **24**, 75–85 (1996). DOI: 10.1016/0167-6636(96)00002-6

[20] Caracciolo R., Gasparetto A., Giovagnoni M.: An experimental technique for complete dynamic characterization of a viscoelastic material. Journal of Sound and Vibration, **272**, 1013–1032 (2004). DOI: 10.1016/j.jsv.2003.03.008

[21] Arzoumanidis G. A., Liechti K. M.: Linear viscoelastic property measurement and its significance for some nonlinear viscoelasticity models. Mechanics of Time-Dependent Materials, **7**, 209–250 (2003). DOI: 10.1023/B:MTDM.0000007357.18801.13

[22] Litt M. H., Torp S.: Strain softening and yeild of polycarbonate-Moiré-grid biaxial-strain analysis. Industrial and Engineering Chemistry Product Research and Development, **11**, 357–363 (1972). DOI: 10.1021/i360043a021

[23] Kästner S., Pohl G.: Ein Beitrag zur Frage der vollständigen Erfassung des mechanischen Relaxationsverhaltens der Polymeren. Colloid and Polymer Science, **191**, 114–123 (1963).

[24] Pritz T.: The Poisson's loss factor of solid viscoelastic materials. Journal of Sound and Vibration, **306**, 790–802 (2007). DOI: 10.1016/j.jsv.2007.06.016

[25] Zhang L., Ernst L. J., Brouwer H. R.: A study of nonlinear viscoelasticity of an unsaturated polyester resin. Part 2. 3D model. Mechanics of Materials, **26**, 167–195 (1997). DOI: 10.1016/S0167-6636(97)00029-X

[26] Lakes R. S.: The time-dependent poissons ratio of viscoelastic cellular materials can increase or decrease. Cellular Polymers, **11**, 466–469 (1992).

[27] van Krevelen D. W.: Properties of polymers. Elsevier, Amsterdam (1990).

[28] Pawlak A., Galeski A.: Plastic deformation of crystalline polymers: The role of cavitation and crystal plasticity. Macromolecules, **38**, 9688–9697 (2005). DOI: 10.1021/ma050842o

[29] Pawlak A., Galeski A.: Cavitation during tensile deformation of polypropylene. Macromolecules, **41**, 2839–2851 (2005). DOI: 10.1021/ma0715122

[30] Quatravaux T., Elkoun S., G'Sell C., Cangemi L., Meimon Y.: Experimental characterization of the volume strain of poly(vinylidene fluoride) in the region of homogeneous plastic deformation. Journal of Polymer Science Part B: Polymer Physics, **40**, 2516–2522 (2002). DOI: 10.1002/polb.10318

[31] Addiego F., Dahoun A., G'Sell C., Hiver J. M.: Volume variation process of high-density polyethylene during tensile and creep tests. Oil and Gas Science and Technology – Rev. IFP, **61**, 715– 724 (2006). DOI: 10.2516/ogst:2006009

[32] Addiego F., Dahoun A., G'Sell C., Hiver J-M.: Characterization of volume strain at large deformation under uniaxial tension in high-density polyethylene. Polymer, **47**, 4387–4399 (2006). DOI: 10.1016/j.polymer.2006.03.093

eXPRESS Polymer Letters Vol.5, No.8 (2011) 698–707
Available online at www.expresspolymlett.com
DOI: 10.3144/expresspolymlett.2011.68

Intrinsic fluorescence studies of compatibility in thermoplastic phenol formaldehyde resin / poly(ε-caprolactone) blends

J. Yang[1], *M. K. Liu*[2], *B. Zhang*[3], *X. D. Chen*[1], *R. W. Fu*[3], *M. Q. Zhang*[3*]

[1]Institute of Polymer Science, DSAPM Lab, OFCM Institute, School of Chemistry and Chemical Engineering, Sun Yat-sen University, Guangzhou 510275, PR China
[2]School of Light and Chemical Engineering, Guangdong University of Technology, Guangzhou 510006, PR China
[3]Key Laboratory for Polymeric Composite and Functional Materials of Ministry of Education, School of Chemistry and Chemical Engineering, Sun Yat-sen University, Guangzhou 510275, PR China

Received 14 November 2010; accepted in revised form 14 February 2011

Abstract. Intrinsic fluorescence method was applied to study the miscibility and interactions of thermoplastic phenol formaldehyde resin (TPF) / poly(ε-caprolactone) (PCL) blends. The characteristic intrinsic fluorescence emission of TPF at 313 nm showed the very good sensitivity to monitor the macromolecular chain motion in the TPF/PCL blends. The glass transition (T_g), crystallization (T_c), and melting transition point (T_m) of TPF/PCL blends were measured by the temperature dependence of intrinsic fluorescence intensities upon heating or cooling process. Interestingly, when TPF/PCL ≥ 5/5, besides a T_g for the amorphous phase of blend, another transition at temperature a little higher than T_g of PCL can be observed by intrinsic fluorescence method. This microheterogeneity can be explained by the so-called 'rigid amorphous phase' (RAP) due to the good flexibility and the strong self-association of PCL chains in amorphous phase. Besides, the analysis of the dependence of T_g on the content of PCL suggests that this microheterogeneity can attenuate the interactions between TPF and PCL chains and result in a lowering of T_gs of blends. In view of the simplicity and sensitivity of measurement as well as affordability of instrument, intrinsic fluorescence proved to be an effective means for characterization of microstructural variation in polymer blends.

Keywords: *polymer blends and alloys, miscibility, interactions, fluorescence*

1. Introduction

During the past years, the miscibility and specific interaction of miscible blends involving crystallizable polymers have been topics of intense interest in polymer science because of the strong economic incentives arising from their potential applications [1–4]. On the basis of the crystallizability of the constituents, crystalline/amorphous binary polymer blends are more widely studied because of their simpler crystalline phase relative to crystalline/crystalline ones [5–14]. And the addition of an amorphous polymer to a crystalline one can modify both the melting (T_m) and the glass transition temperature (T_g) of the crystalline polymer and consequently has an important effect on kinetic parameters governing the crystallization process. Therefore, it would be very important to determine the interactions between the amorphous polymer and crystallization regimes. And most of studies on these systems are concerned with dipole-dipole interactions, hydrogen bonding strengths, morphology patterns or crystallization kinetics.

From one experimental point of view, an improvement in the understanding of the correlation between

*Corresponding author, e-mail: ceszmq@mail.sysu.edu.cn

microstructure and interaction of polymers has been obtained by several techniques, such as differential scanning calorimetry (DSC), dynamic mechanical thermal analysis (DMA), electron microscopy (EM), Fourier transform infrared (FTIR) spectroscopy etc. [5–14] Each of these techniques has its advantages and drawbacks. For instance, DSC is very convenient to observe miscibility in polymer blends, but it is not so sensitive and sometimes it is very hard to clearly identify T_gs of the blends. Though DMA is relatively sensitive [15], the sample preparation is complicated, especially for those polymers whose T_g is below the room temperature. Compared with thermal analysis and EM, FTIR can analyze, in situ, some positive information on specific interactions between polymers without introducing additional physical process like freezing a given phase-separated state for the measurements. However, the IR spectral bands cannot be readily resolved into two peaks with areas corresponding to the free and the hydrogen-bonded absorptions [16]. Relatively, owing to the merits of high sensitivity and nondestructive measurements, the fluorescence technology has been regarded as a powerful and effective tool to measure the macromolecular motions on a molecular level with probe and labeling [17–19]. Although this method can obtain lots of useful information of polymer micromorphology and microstructure, the labeling procedure is often tedious. In addition, in most of the fluorimetric studies of polymer, the fluorescent probe was covalently attached to one of the polymers, which in fact changed the microenvironment of macromolecules and made the macromolecules more hydrophobic, thus enhancing their complexation ability. It is worth noting that the intrinsic fluorescence of polymers has also shown to be highly sensitive to issues ranging from local polymer conformational populations in solution and phase behavior in solvents and polymer blends to local microenvironments in bulk homopolymers [20–23]. Due to its intrinsic sensitivity, this fluorescence method also proved to be powerful in the study of small-scale phase separation and low-concentration miscibility [24]. In our previous researches [25, 26], the intrinsic fluorescence spectra were found to be very simple and sensitive means to characterize the transition of molecular conformation and aggregation of macromolecular chains.

In this work, we employed the intrinsic fluorescence method to investigate the miscibility and interactions of crystalline/amorphous polymer blends. For convenience, we chose a very common crystalline polymer, poly(ε-caprolactone) (PCL), which is miscible with several amorphous polymers through the formation of hydrogen bonding [27, 28]. Since the miscibility of PCL blends depends on the self-association and inter-association of hydrogen-bonding donor polymers, the amorphous component used here is thermoplastic phenol formaldehyde resin (TPF) which has polar group (hydroxyl group) and chromophores (benzene rings). It was found that the intrinsic fluorescence can provide us valuable information of compatibility on a very small scale and might supplement the existing characterization tools.

2. Experimental

2.1. Materials and samples preparation

The PCL used in this work was purchased from Polysciences (UK). The TPF was synthesized as follows: First, the molten phenol and oxalic acid were placed into a flask fitted with a mechanical stirrer, a condenser, and a thermometer. And then the mixture was heated to 90°C (a slight exotherm was noted), and formaldehyde was charged into the reaction mixture over a 90 min period using a dropping funnel, during which time the temperature began to drop. The molar ratio for phenol / formaldehyde / oxalic acid was 1 / 0.75 / 0.01. External heating was required to keep the system at ~95°C for the duration of the reaction. Reactions were heated for an additional 6 h before the resins were isolated. After the condensation process, volatiles, water, and some free phenol were removed using a high-temperature (150°C) vacuum distillation. Finally, the solid resin was powdered using a mortar and pestle. The molecular weights and the polydispersity index (DPI) were determined through gel permeation chromatography (GPC) using a Waters 510 HPLC (U. S. A.), equipped with a 410 differential refractometer, a refractive index (RI) detector, and three Ultrastyragel columns connected in series in order of increasing pore size. *N*,*N*-dimethylformamide (DMF) with LiBr (1 g/l) was used as eluent solvent at a flow rate of 0.6 ml/min at 25°C. DMF (A. R.) and toluene (A. R.), purchased from Guangzhou Chemical Reagent Factory (P. R. China),

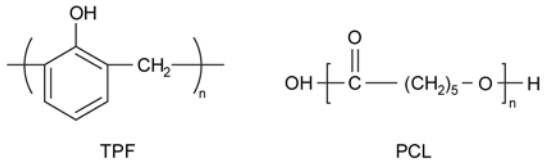

Figure 1. Schematic representation of the chemical structure of TPF and PCL molecules

Table 1. Characterization of TPF and PCL used in this study

Polymer	M_n [Da][a]	DPI	T_g [K][b]	T_m [K][b]
TPF	$1 \cdot 10^3$	1.9	337	–
PCL	$4 \cdot 10^4$	1.5	210	327

[a]Data obtained from GPC measurement
[b]Determined by DSC method

were distilled under reduced pressure before use. The chemical structures and basic characterization of TPF and PCL are shown in Figure 1 and Table l, respectively. Film samples with various compositions were prepared by casting from 1 wt% toluene solutions onto quartz plates at room temperature. Firstly, the solution was allowed to evaporate slowly at room temperature for 1 day, and then the films were further heat treated in a vacuum oven at 50°C for 24 h to ensure the total elimination of solvent.

2.2. Apparatus

The fluorescence spectra were recorded with a FLS920 Combined Fluorescence Lifetime and Steady State Spectrometer (Edinburgh, England) using either a cooling or heating rate of 3 K/min. Unless otherwise specified, in cooling and heating measurements, the fluorescence spectra were recorded after having annealed samples at 410 and 180 K for 15 min, respectively. To minimize the influence of reflected light, 45º-angle sample geometry was employed. For the convenience of comparison, samples were also examined by a DSC-204 (Netzsch, Germany) under the same condition.

3. Results and discussion

3.1. Intrinsic fluorescence of TPF and PCL solutions.

In order to better understand the intrinsic fluorescence of blend films, we first measured the emission spectra in TPF and PCL solution at the concentration of 2 g/l. Clearly, a negligible fluorescence emission of PCL can be seen in Figure 2. Besides, there exists the maximum fluorescence intensity for

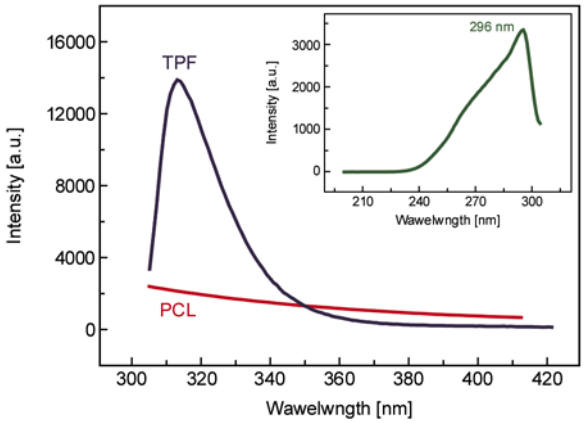

Figure 2. Fluorescence emission spectra of TPF and PCL solution (C = 2 g/l) in THF (λ_{ex} = 296 nm). Inset shows the excitation spectrum for phenolic film.

TPF at 315 nm when excitation was done at 296 nm according to the excitation spectrum shown in the inset of Figure 2. Thus, these results make it easy to attribute the fluorescence emission of TPF/PCL films in the following discussions.

3.2. Temperature dependent intrinsic fluorescence of TPF/PCL Films

Figure 3 shows the intrinsic fluorescence spectra of TPF/PCL (3/7) blend film at various temperatures during the cooling process. As expected, a maximum intensity can be observed at about 313 nm, indicative of the emission of TPF phase. Obviously, the emission intensity increases as the temperature decreases, suggesting a decrease in the non-radiative deactivation process upon cooling.

Figure 4 presents the temperature dependence of fluorescence intensity of TPF/PCL (3/7) blend film during the cooling process. It can be clearly seen that two crossovers are located at 241 and 298 K,

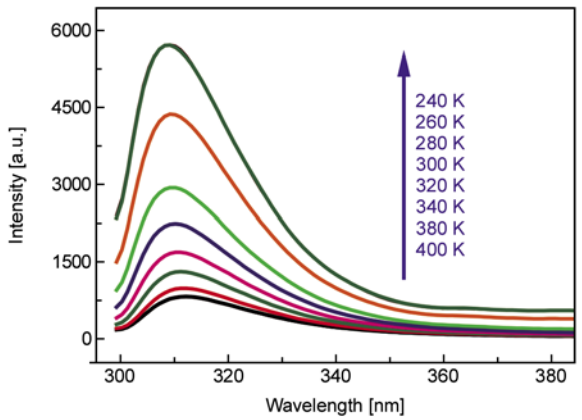

Figure 3. Intrinsic fluorescence spectra of TPF/PCL (3/7) blend film at various temperatures during the cooling process

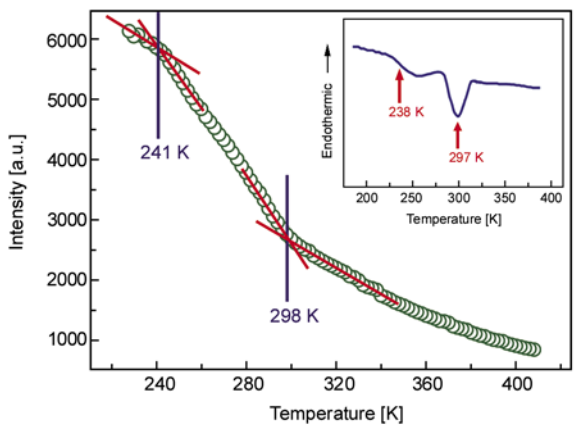

Figure 4. Temperature dependence of the intrinsic fluorescence intensity for TPF/PCL (3/7) blend film during the cooling process. The inset shows the DSC cooling trace.

respectively, which are in good agreement with the transition temperatures shown in DSC cooling trace, i.e., 238 and 297 K, respectively (see inset of Figure 4). Thus, these two crossovers should be attributed to the glass transition temperature (T_g) of TPF/PCL amorphous phase and the crystallization temperature (T_c) of PCL crystalline phase, respectively. Such single T_g obtained by both fluorescence and DSC methods indicates that TPF/PCL (3/7) blend is fully miscible in the amorphous region.

Before we present a further interpretation of the temperature dependence of fluorescence intensity shown in Figure 4, it is necessary to review briefly several aspects of the photophysical process. Fundamentally, the excited state of chromophore promoted by absorption of a photon is deactivated by radiative (fluorescence K_r), and non-radiative (K_{nr}), thus the fluorescence intensity (I) can be understood as Equation (1):

$$I \propto \varphi_F = \frac{K_r}{K_r + K_{nr}} \tag{1}$$

where φ_F is the fluorescence quantum yield. Since Kr only depends on temperature through the refraction index [29], Equation (1) can be expressed as Equation (2):

$$I \propto \frac{K_r^0 n^2}{K_r^0 n^2 + K_{nr}} = 1 - \frac{K_{nr}}{K_r^0 n^2 + K_{nr}} \tag{2}$$

where K_r^0 is a constant independent of temperature and n is the refraction index. Distinctly, as shown in Equation (2), the intrinsic fluorescence intensity is mainly influenced by n and K_{nr}. Usually, it is assumed that, the non-radiative processes (K_{nr}) almost become zero at very low temperatures, so that the radiative deactivation is the favored pathway and only K_r accounts for the fluorescence intensity. However, at relatively high temperatures, the motions of the polymer chains are less limited and the balance of these two factors should be taken into account: (i) the reduction of the refraction index [30] and (ii) the deactivation of the fluorescence by non-radiative processes due to the increased thermal motions [31]. Note that, the refractive index of amorphous polymer film decreases with the temperature increases and shows a inflection point at Tg, suggesting stronger temperature dependence at $T > T_g$ than $T < T_g$ [30]. Hence, the explanation of the results obtained in Figure 4 should now be clear. When the temperature was lower than 298 K ($T < T_c$), the molecular chains of PCL started to arrange themselves in regular arrays upon crystallization and restrict the motions of TPF chains which reduced the non-radiative decay rate and finally caused the higher fluorescence quantum yield and the greater temperature dependence of intrinsic fluorescence intensity. On the other hand, the less temperature dependence of intrinsic fluorescence intensity at $T < 241$ K was dominantly induced by the effect of refraction index and non-radiative rate, which both showed less temperature dependence in the glassy state compared to rubbery state [32], due to the limited large-scale cooperative mobility of macromolecular chains in amorphous region at $T < T_g$.

To obtain the comprehensive assessment of intrinsic fluorescence, the heating process of TPF/PCL (3/7) blend film has also been studied, shown in Figure 5. There are also two obvious crossovers in the plot, located at 248 and 318 K, highly consistent with the T_g of TPF/PCL amorphous phase (245 K) and the melting temperature (T_m) of PCL crystalline phase (319 K) obtained by DSC method (see inset of Figure 5). As expected, the temperature dependence of fluorescence intensity around T_g of TPF/PCL amorphous phase during cooling process (Figure 4) is similar with that during heating process (Figure 5). However, in contrast to cooling process, the heating process shows an opposite intensity variance around the transition temperature of PCL crystalline, that is, a stronger temperature dependence of fluorescence intensity. This behavior sug-

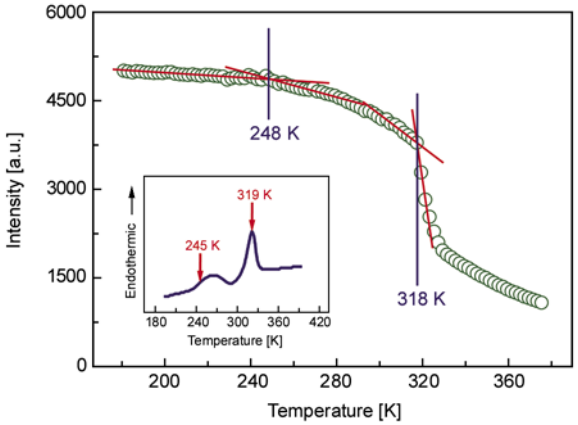

Figure 5. Temperature dependence of the intrinsic fluorescence intensity for TPF/PCL (3/7) blend film during the heating process. The inset shows the DSC heating trace.

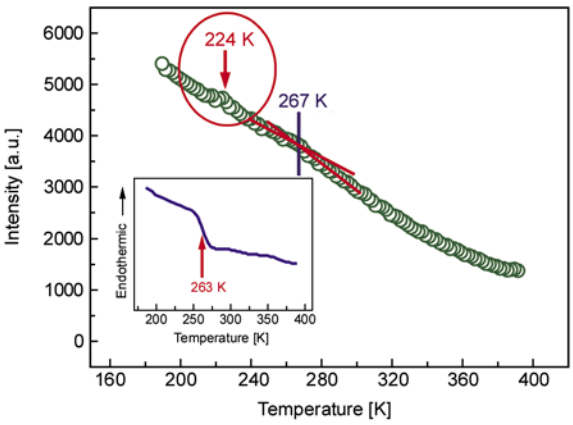

Figure 7. Temperature dependence of the intrinsic fluorescence intensity for TPF/PCL (5/5) blend film during the cooling process. The inset shows the DSC cooling trace.

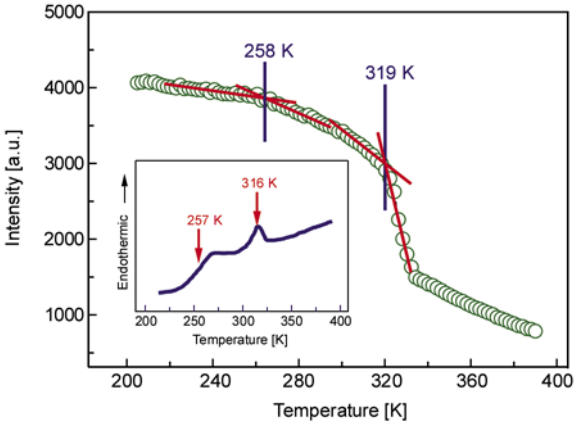

Figure 6. Temperature dependence of the intrinsic fluorescence intensity for TPF/PCL (4/6) blend film during the heating process. The inset shows the DSC heating trace.

gests that, when melting process started to occur, the flexible PCL chains could render more drastic movement of TPF due to the strong hydrogen bond interaction between the hydroxyls of TPF and carbonyls of PCL, which greatly increased the non-radiative decay rate and thus reduced intrinsic fluorescence quantum yield of TPF. Thus, the results in Figure 5 not only verify our explanation in Figure 4, but also strongly suggest that the intrinsic fluorescence is very sensitive method for monitoring the molecular chain motions in TPF/PCL blend film. The similar behavior can be also found in the case of TPF/PCL (4/6) blend (see Figure 6).

However, it can be seen for TPF/PCL (5/5) blend, there is only a single T_g (263 K) in the DSC trace (inset of Figure 7), which indicates the TPF/PCL (5/5) blend is not only completely amorphous but also homogeneous due to the strong hydrogen bond interaction. Surprisingly, as shown in Figure 7, it can be observed that there are two crossovers determined by intrinsic fluorescence, located at 267 and 224 K, respectively. The former temperature is in agreement with T_g of TPF/PCL blend in DSC trace, while the latter one is a little higher than the T_g of PCL (210 K). Generally, a polymer blend is regarded as miscible when it exhibits a single T_g and regarded as immiscible when it exhibits two T_gs corresponding to those of the constituent components as determined by DSC. However, there is a general consensus that such experimental technique, while very useful to investigate macrophase separation in the polymer blends, cannot guarantee that a polymer blend is miscible on a molecular level [33–35]. Besides, fluorescence spectroscopy has proven to be very sensitive method in studying aggregation and phase separation behavior at the molecular level, and can provide us with information on a scale smaller than conventional light scattering and comparable to small-angle neutron scattering (SANS) [36]. Since the homogeneity of a polymer blend is usually dependent on the detectable minimum domain size by the experimental technique used, a plausible explanation is that, the crossover at 224 K may be ascribed to the microscopic heterogeneity in the TPF/PCL (5/5) blend.

Note, in Figure 7, that there is a slight change in the slope at around 320 K which is close to the T_c of PCL. Was this caused by the inhomogeneous mixing in sample preparation? To answer this question, Figure 8 displayed the temperature dependence of

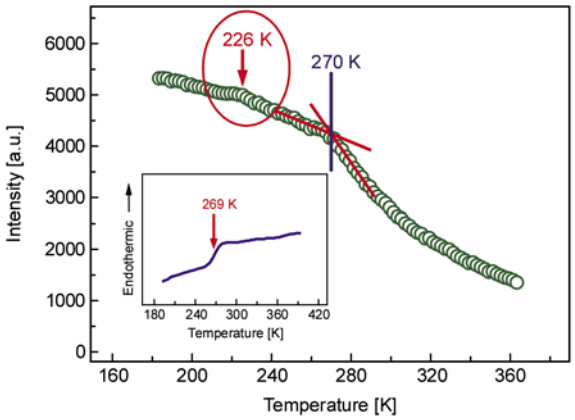

Figure 8. Temperature dependence of the intrinsic fluorescence intensity for TPF/PCL (5/5) blend film during the heating process. The inset shows the DSC heating trace.

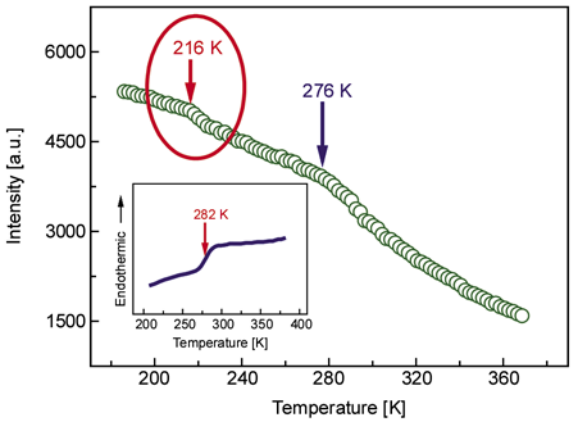

Figure 9. Temperature dependence of the intrinsic fluorescence intensity for TPF/PCL (6/4) blend film during the heating process. The inset shows the DSC heating trace.

the intrinsic fluorescence intensity for TPF/PCL (5/5) blend film during the heating process. Clearly, the inflexion point at 270 K can be observed, which is ascribed to the T_g of TPF/PCL blend. However, another unexpected crossover at 226 K has also been found. Moreover, no drastic decrease in the slope appears around T_m of PCL in Figure 8. This result strongly convinces us that the crossover at lower temperature (224 K) in Figure 7 should result from the microheterogeneity in the TPF/PCL (5/5) blend instead of the error in sample preparation.

In order to further testify the above result, TPF-rich blend has also been investigated. Because the intrinsic fluorescence showed the more obvious response upon heating than upon cooling, we only concentrate on the temperature dependence of fluorescence intensity of TPF/PCL (6/4) and (7/3) blend film during the heating process, shown in Figure 9 and 10, respectively. Similarly, no indication of PCL crystalline but two transition temperatures appear (one close to T_g of blend and the other a little higher than T_g of PCL), which coincides with the result shown in Figure 7 and 8.

To better understand the compatibility of TPF/PCL, a careful analysis of the dependence of T_g for polymer blends on the content of PCL was considered. As we know, the Fox relation [37, 38] (see Equation (3)) is well used to describe the T_g dependence of random mixed polymer blend:

$$\frac{1}{T_g} = \frac{W_1}{T_{g1}} + \frac{W_1}{T_{g2}} \tag{3}$$

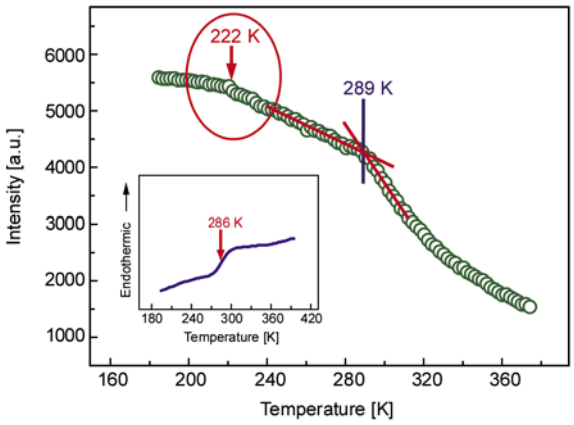

Figure 10. Temperature dependence of the intrinsic fluorescence intensity for TPF/PCL (7/3) blend film during the heating process. The inset shows the DSC heating trace.

where T_{g1}, T_{g2} and T_g refer to the T_g of TPF, PCL and TPF/PCL blend, W_1 and W_2 refer to weight fractions of component, i.e. TPF and PCL, respectively. Figure 11 summarizes the variation of T_g by the intrinsic fluorescence and DSC with increasing W_1 of TPF/PCL blends. As can be seen, results obtained by intrinsic fluorescence and DSC method show a good agreement. In order to better understand Figure 11, the curves are divided into three regions by two critical weight fractions W_{cr1} and W_{cr2}, which are located at 0.5 and 0.7, respectively. Obviously, an upward curvature of $T_g - W_1$, i.e. strong positive deviations from Fox rule can be seen at $W_1 < W_{cr2}$ (region I and region II). Note that, only DSC data are shown at $W_2 < W_{cr1}$ (region I) since it is hard for intrinsic fluorescence method to calculate the weight fraction of amorphous component when there exist a crystallization phase in

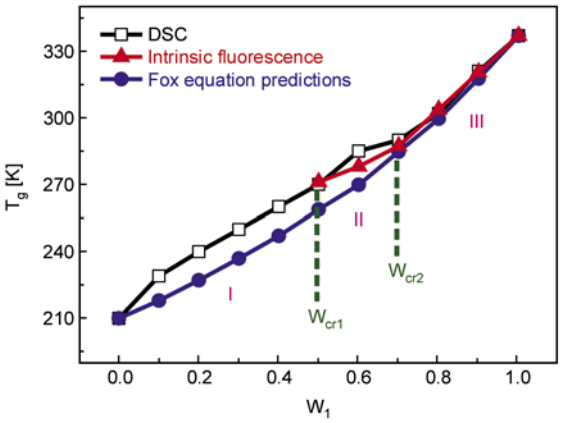

Figure 11. Dependence of T_g obtained by intrinsic fluorescence and DSC on weight fraction of TPF, W_1, for TPF/PCL blends.

TPF/PCL blends. Since there is no microheterogeneity in region I, the positive deviations can be simply explained by the balance of two opposite effects: (i) the increase in stiffness due to strong interactions between two components which enhances T_gs of blends [39–41], and (ii) the destruction of the self association of each component which lowers T_gs of blends [42]. So it is easy to understand the former effect is the dominant one in region I. Besides, this result also implies that the strong interactions between the TPF and PCL chains can still exist even when the content of TPF is relatively low, e.g. $W_1 < 0.3$. Thereby, it is reasonable to expect that the similar situation should also arise when the content of TPF is high, e.g. $W_2 > 0.7$. Unfortunately, when the content of TPF increases up to W_{cr2} ($W_1 = 0.7$), the upward curvature disappears (region III). As we know, for the amorphous phase in TPF/PCL blends, the only difference between region I and region III is that there is the microheterogeneity in the latter but not in the former. Thus, the phenomenon in region III not only confirms the existence of microheterogeneity but also suggests this microheterogeneity can attenuate the interactions between TPF and PCL chains and result in a lowering of T_gs of blends.

3.3. The mechanism of formation of microheterogeneity

According to the finding above, a hypothetical mechanism is schematically proposed in Figure 12, to describe the interaction behavior and formation of microheterogeneity in TPF/PCL blends: (i) when TPF/PCL < 5/5, the blend can form a homogeneous amorphous phase and a crystalline phase due to the strong hydrogen bond interactions between the hydroxyls of TPF and the carbonyl or ether groups of PCL; (ii) when TPF/PCL > 5/5, the regular arrangement of PCL macromolecular chain in the crystalline phase is completely destroyed by a large amount of TPF chains. It is worth mentioning that many semi-crystalline polymers such as poly(ethylene terephtahlate) (PET) [43], poly(cabonate) (PC) [44], polypropylene (PP) [45], have been found to possess of in a three-phase structure consisting of crystalline, amorphous phases and a so-called third phase i.e., rigid amorphous phases (RAP). The RAP has the distinct chain mobility from conventional amorphous phase and can only unfreeze at a temperature higher than T_g [46]. Thus, similarly in the cases of TPF/PCL > 5/5, due to their good flexibility and the strong self-association, the amorphous PCL phase still tend to arrange orderly to some extent in a small domain, forming an amorphous PCL microphase like RAP and leading to the microheterogeneity. Similar phenomena have also been observed in other miscible crystalline/amorphous polymer blends judging from the DSC and morphological results. For example, by using ^{1}H spin-lattice relaxation times in the rotating and laboratory frames, Parizel *et al.* [47] found that, the organization of the PEO/PMMA blend consisted of three parts: a crystalline PEO, constrained PEO units in the neighborhood of the crystalline lamellae and a miscible amorphous phase that is PMMA-rich. In addition, Asano *et al.* [48] have successfully utilized high-resolution solid-state NMR to analyze various heterogeneity scales in blends of poly

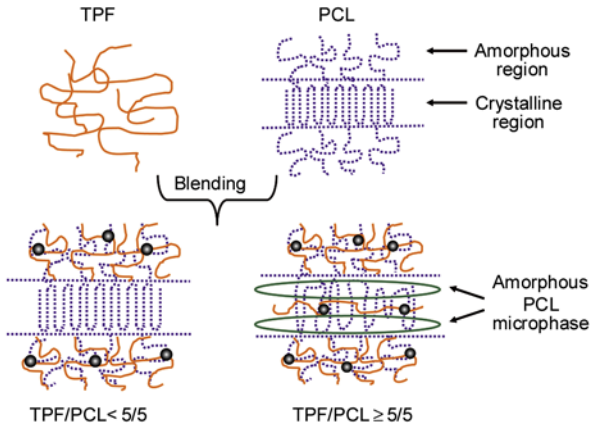

Figure 12. Schematic representation for the heterogeneity in TPF/PCL blends. The solid round dots stand for hydrogen bonds between TPF and PCL.

(vinylphenol) with poly(ethylene oxide) (PEO), leading to the conclusion that miscibility is limited to above the 20–30 nm scale. Furthermore, in the research of Lin *et al.* [49], the rotating-frame spin-lattice relaxation time for protons, $T_{1\rho}(^1H)$, was measured from ^{13}C CP/MAS/DD NMR to probe molecular scales of heterogeneity in the miscible poly(benzyl methacrylate) (PBzMA)/poly(ethylene oxide) (PEO) blend over the whole composition range. Their results indicated that, three phases also appeared for the blends with PEO component > 16%, containing one miscible homogenous PBzMA-rich phase, one constrained PEO phase and one crystalline PEO phase. It worth mentioning, what a pity it is that the unambiguous clarification of PCL micro-phase structure in TPF/PCL blend is now not attainable due to the limitation of the detectable minimum domain size of our existing equipments. However, this work is still in progress in our laboratory by using other model polymer systems with the fluorescent probe technique.

4. Conclusions

The miscibility and interactions in TPF/PCL blends were investigated by the intrinsic fluorescence method. By monitoring characteristic intrinsic fluorescence intensity of TPF, the microheterogeneity can be observed in the blends (TPF/PCL ≥ 5/5). Such a behavior is because that, after the crystalline phase of PCL is completely destroyed by TPF chains, the amorphous PCL phase still tend to arrange orderly to some extent in a small area due to their good flexibility and the strong self-association and thus forms the RAP. Besides, the analysis of the dependence of T_g on the content of PCL suggests that this microheterogeneity can attenuate the interactions between TPF and PCL chains and result in a lowering of T_gs of blends. In view of the simplicity and sensitivity of measurement, affordability and availability of instrument, intrinsic fluorescence method proved to be an effective means for characterization of microstructural variation in polymer blends.

Since the molecular weight of TPF is low and the TPF molecules are very easy to diffuse in the blend, whether or not the microheterogeneity behavior obtained in this work can be extended to high-molecular-weight polymers deserves further verification. And we believe that deeper information on the molecular level would be obtained by changing the various chromophores. Besides, the intrinsic fluorescence method can also be extended to applied researches, like *in-situ* inspection of macromolecular motion, diffusing process, phase separation mechanism, the interfacial interaction between polymers and evaluation of the effect of compatibilizer.

Acknowledgements

X. D. Chen acknowledges the financial support from the program of National Natural Science Foundation of China (Grant no. 50973129), Natural Science Foundation of Guangdong province (Grant no. 07003702) and China Postdoctoral Science Foundation (Grant no. 20100470953).

References

[1] Zhong Z., Guo Q., Mi Y.: Solid-state n.m.r. investigation of crosslinkable blends of novolac and poly(ε-caprolactone). Polymer, **40**, 27–33 (1998). DOI: 10.1016/S0032-3861(98)00242-0

[2] Miyoshi T., Takegoshi K., Hikichi K.: High-resolution solid-state ^{13}C nuclear magnetic resonance study of a polymer complex: poly(methacrylic acid)/poly(ethylene oxide). Polymer, **37**, 11–18 (1996). DOI: 10.1016/0032-3861(96)81594-1

[3] Chu P. P., Wu H-D.: Solid state NMR studies of hydrogen bonding network formation of novolac type phenolic resin and poly(ethylene oxide) blend. Polymer, **41**, 101–109 (1999). DOI: 10.1016/S0032-3861(99)00098-1

[4] Sawatari C., Kondo T.: Interchain hydrogen bonds in blend films of poly(vinyl alcohol) and its derivatives with poly(ethylene oxide). Macromolecules, **32**, 1949–1955 (1999). DOI: 10.1021/ma980900o

[5] Russell T. P., Ito H., Wignall G. D.: Neutron and X-ray scattering studies on semicrystalline polymer blends. Macromolecules, **21**, 1703–1709 (1988). DOI: 10.1021/ma00184a029

[6] Defieuw G., Groeninckx G., Reynaers H.: Miscibility and morphology of binary polymer blends of polycaprolactone with solution-chlorinated polyethylenes. Polymer, **30**, 595–603 (1989). DOI: 10.1016/0032-3861(89)90141-9

[7] Talibuddin S., Runt J., Liu L-Z., Chu B.: Microstructure development and crystallization of poly(ethylene oxide) and melt-miscible PEO blends. Macromolecules, **31**, 1627–1634 (1998). DOI: 10.1021/ma971265+

[8] Penning J. P., st. John Manley R.: Miscible blends of two crystalline polymers. 1. Phase behavior and miscibility in blends of poly(vinylidene fluoride) and poly (1,4-butylene adipate). Macromolecules, **29**, 77–83 (1996).
DOI: 10.1021/ma950651t

[9] Eersels K. L. L., Groeninckx G., Koch M. H. J., Reynaers H.: Influence of transreaction processes on the morphology of semicrystalline aliphatic/aromatic polyamide blends. Polymer, **39**, 3893–3900 (1998).
DOI: 10.1016/S0032-3861(97)10092-1

[10] Huo P. P., Cebe P., Capel M.: Dynamic mechanical relaxation and X-ray scattering study of poly(butylene terephthalate)/polyarylate blends. Macromolecules, **26**, 4275–4282 (1993).
DOI: 10.1021/ma00068a031

[11] Cheung Y. W., Stein R. S., Lin J. S., Wignall G. D.: Small-angle scattering investigations of poly(ε-caprolactone)/polycarbonate blends. 2. Small-angle X-ray and light scattering study of semicrystalline/semicrystalline and semicrystalline/amorphous blend morphologies. Macromolecules, **27**, 2520–2528 (1994).
DOI: 10.1021/ma00087a021

[12] Saito H., Stuehn B.: Exclusion of noncrystalline polymer from the interlamellar region in poly(vinylidene fluoride)/poly(methyl methacrylate) blends. Macromolecules, **27**, 216–218 (1994).
DOI: 10.1021/ma00079a032

[13] Sadocco P., Canetti M., Seves A., Martuscelli E.: Small-angle X-ray scattering study of the phase structure of poly(D-(−)-3-hydroxybutyrate) and atactic poly(epichlorohydrin) blends. Polymer, **34**, 3368–3375 (1993).
DOI: 10.1016/0032-3861(93)90462-J

[14] Liu L-Z., Chu B., Penning J. P., Manley R. S. J.: A synchrotron SAXS study of miscible blends of semicrystalline poly(vinylidene fluoride) and semicrystalline poly(1,4-butylene adipate). Macromolecules, **30**, 4398–4404 (1997).
DOI: 10.1021/ma961719n

[15] Molnar A., Eisenberg A.: Miscibility of polyamide-6 with lithium or sodium sulfonated polystyrene ionomers. Macromolecules, **25**, 5774–5782 (1992).
DOI: 10.1021/ma00047a032

[16] Le Menestrel C., Bhagwagar D. E., Painter P. C., Coleman M. M., Graf J. F.: Hydrogen bonding in ternary polymer blend systems: Determination of association parameters. Macromolecules, **25**, 7101–7106 (1992).
DOI: 10.1021/ma00052a005

[17] Klopffer M-H., Bokobza L., Monnerie L.: Structural side effects in the use of a fluorescent probe for monitoring polymer mobility. Macromolecules, **31**, 8291–8296 (1998).
DOI: 10.1021/ma980717v

[18] Moffitt M., Farinha J. P. S., Winnik M. A., Rohr U., Müllen K.: Steady-state and dynamic fluorescence measurements of a perylene-labeled triblock copolymer: Evidence for ground-state dye aggregate formation. Macromolecules, **32**, 4895–4904 (1999).
DOI: 10.1021/ma990332s

[19] Corrales T., Peinado C., Bosch P., Catalina F.: Study of secondary relaxations of poly(ethylene terephthalate) by photoluminescence technique. Polymer, **45**, 1545–1554 (2004).
DOI: 10.1016/j.polymer.2003.12.051

[20] Major M. D., Torkelson J. M.: Fluorescence of vinyl aromatic polyelectrolytes: Effects of conformation, concentration, and molecular weight of sodium poly (styrene sulfonate). Macromolecules, **19**, 2801–2806 (1986).
DOI: 10.1021/ma00165a024

[21] Tsai F. J., Torkelson J. M.: Phase separation of oligomeric polystyrene-polybutadiene blends as studied by excimer fluorescence. Macromolecules, **21**, 1026–1033 (1988).
DOI: 10.1021/ma00182a031

[22] Clauss B., Salem D. R.: A chain-intrinsic fluorescence study of orientation-strain behavior in uniaxially drawn poly(ethylene terephthalate) film. Macromolecules, **28**, 8328–8333 (1995).
DOI: 10.1021/ma00128a049

[23] Sanz A., Mendicuti F.: Excimers in dilute solutions of *N*-vinyl carbazole/styrene copolymers of different molar compositions. Polymer, **43**, 6123–6130 (2002).
DOI: 10.1016/S0032-3861(02)00584-0

[24] Semerak S. N., Frank C. W.: Excimer fluorescence as a molecular probe of blend miscibility. 3. Effect of molecular weight of the host matrix. Macromolecules, **14**, 443–449 (1981).
DOI: 10.1021/ma50003a039

[25] Luo W-A., Liao Z., Yan J., Li Y., Chen X., Mai K., Zhang M.: Cold-crystallization of poly(trimethylene terephthalate) studied by photoluminescence of its amorphous portion. Macromolecules, **41**, 7513–7518 (2008).
DOI: 10.1021/ma801119n

[26] Luo W-A., Chen Y., Chen X., Liao Z., Mai K., Zhang M.: Photoinduced energy transfer in poly(trimethylene terephthalate). Macromolecules, **41**, 3912–3918 (2008).
DOI: 10.1021/ma8000059

[27] Lezcano E. G., Coll C. S., Prolongo M. G.: Melting behaviour and miscibility of poly(ε-caprolactone) + poly(4-hydroxystyrene) blends. Polymer, **37**, 3603–3609 (1996).
DOI: 10.1016/0032-3861(96)00170-X

[28] De Juana R., Cortazar M.: Study of the melting and crystallization behavior of binary poly(ε-caprolactone)/poly(hydroxy ether of bisphenol A) blends. Macromolecules, **26**, 1170–1176 (1993).
DOI: 10.1021/ma00057a042

[29] Birks J. B.: Photophysics of aromatics molecules. Wiley, New York (1970).
[30] Beaucage G., Composto R., Stein R. S.: Ellipsometric study of the glass transition and thermal expansion coefficients of thin polymer films. Journal of Polymer Science Part B: Polymer Physics, **31**, 319–326 (1993). DOI: 10.1002/polb.1993.090310310
[31] Turrión S. G., Olmos D., Ekizoglou N., González-Benito J.: Fluorescence response from anthracene labeled polystyrene to study its thermal transitions. Polymer, **46**, 4023–4031 (2005). DOI: 10.1016/j.polymer.2005.03.056
[32] Mundra M. K., Ellison C. J., Behling R. E., Torkelson J. M.: Confinement, composition, and spin-coating effects on the glass transition and stress relaxation of thin films of polystyrene and styrene-containing random copolymers: Sensing by intrinsic fluorescence. Polymer, **47**, 7747–7759 (2006). DOI: 10.1016/j.polymer.2006.08.064
[33] Wagler T., Rinaldi P. L., Han C. D., Chun H.: Phase behavior and segmental mobility in binary blends of polystyrene and poly(vinyl methyl ether). Macromolecules, **33**, 1778–1789 (2000). DOI: 10.1021/ma9909105
[34] Kuo S. W., Huang C. F., Chang F. C.: Study of hydrogen-bonding strength in poly(ε-caprolactone) blends by DSC and FTIR. Journal of Polymer Science Part B: Polymer Physics, **39**, 1348–1359 (2001). DOI: 10.1002/polb.1107
[35] Stoelting J., Karasz F. E., MacKnight W. J.: Dynamic mechanical properties of poly(2,6-dimethyl-1,4-phenylene ether)-polystyrene blends. Polymer Engineering and Science, **10**, 133–138 (1970). DOI: 10.1002/pen.760100302
[36] Gomez-Elvira J. M., Halary J. L., Monnerie L., Fetters L. J.: Isotope effects on the phase separation in polystyrene-poly(vinyl methyl ether) blends. 2. Influence of the microstructure of linear and star block copolymers. Macromolecules, **27**, 3370–3375 (1994). DOI: 10.1021/ma00090a035
[37] Prolongo M. G., Salom C., Masegosa R. M.: Glass transitions and interactions in polymer blends containing poly(4-hydroxystyrene) brominated. Polymer, **43**, 93–102 (2001). DOI: 10.1016/S0032-3861(01)00567-5
[38] Fox T. G.: Influence of diluent and of copolymer composition on the glass temperature of a polymer system. Bulletin of the American Physical Society, **1**, 123–124 (1956).
[39] Kwei T. K.: The effect of hydrogen bonding on the glass transition temperatures of polymer mixtures. Journal of Polymer Science, Polymer Letters Edition, **22**, 307–313 (1984). DOI: 10.1002/pol.1984.130220603
[40] Prinos A., Dompros A., Panayiotou C.: Thermoanalytical and spectroscopic study of poly(vinyl pyrrolidone)/poly(styrene-co-vinyl phenol) blends. Polymer, **39**, 3011–3016 (1998). DOI: 10.1016/S0032-3861(97)10085-4
[41] Wang J., Cheung M. K., Mi Y.: Miscibility in blends of poly (4-vinylpyridine)/poly (4-vinylphenol) as studied by ^{13}C solid-state NMR. Polymer, **42**, 3087–3093 (2001). DOI: 10.1016/S0032-3861(00)00643-1
[42] Sanchis A., Prolongo M. G., Salom C., Masegosa R. M.: Melting behavior, miscibility, and hydrogen-bonded interactions of poly(ε-caprolactone)/poly(4-hydroxystyrene-co-methoxystyrene) blends. Journal of Polymer Science Part B: Polymer Physics, **36**, 95–104 (1998). DOI: 10.1002/(SICI)1099-0488(19980115)36:1<95::AID-POLB11>3.0.CO;2-9
[43] Takayanagi M., Yoshino M., Minami S.: State of crystallization of polyethylene terephthalate determined by the viscoelastic absorptions. Journal of Polymer Science, **61**, 7–10 (1962). DOI: 10.1002/pol.1962.1206117129
[44] Laredo E., Grimau M., Müller A., Bello A., Suarez N.: Influence of aging and crystallinity on the molecular motions in bisphenol-A polycarbonate. Journal of Polymer Science Part B: Polymer Physics, **34**, 2863–2879. (1996). DOI: 10.1002/(SICI)1099-0488(199612)34:17<2863::AID-POLB2>3.0.CO;2-S
[45] Zuo F., Keum J. K., Chen X., Hsiao B. S., Chen H., Lai S-Y., Wevers R., Li J.: The role of interlamellar chain entanglement in deformation-induced structure changes during uniaxial stretching of isotactic polypropylene. Polymer, **48**, 6867–6880 (2007). DOI: 10.1016/j.polymer.2007.08.065
[46] Cheng S. Z. D., Wu Z. Q., Wunderlich B.: Glass transition and melting behavior of poly(thio-1,4-phenylene). Macromolecules, **20**, 2802–2810 (1987). DOI: 10.1021/ma00177a028
[47] Parizel N., Lauprétre F., Monnerie L.: N.m.r. and d.s.c. investigations of the miscibility of poly(methyl methacrylate)/poly(ethylene oxide) blends. Polymer, **38**, 3719–3725 (1997). DOI: 10.1016/S0032-3861(96)00952-4
[48] Asano A., Takegoshi K., Hikichi K.: Solid-state NMR study of miscibility and phase-separation of polymer blend: polycarbonate/poly(methyl methacrylate). Polymer Journal, **24**, 555–562 (1992). DOI: 10.1295/polymj.24.555
[49] Lin R-H., Woo E. M., Chiang J. C.: A solid-state ^{13}C NMR study on phase heterogeneity in the miscible blend of amorphous poly(benzyl methacrylate) with semicrystalline poly(ethylene oxide). Polymer, **42**, 4289–4297 (2001). DOI: 10.1016/S0032-3861(00)00671-6

eXPRESS Polymer Letters Vol.5, No.8 (2011) 708–716
Available online at www.expresspolymlett.com
DOI: 10.3144/expresspolymlett.2011.69

Qualitative separation of the effect of voids on the static mechanical properties of hygrothermally conditioned carbon/epoxy composites

A. Y. Zhang[1,2], *D. H. Li*[1], *D. X. Zhang*[1*], *H. B. Lu*[1], *H. Y. Xiao*[1], *J. Jia*[1]

[1]Harbin Institute of Technology, 150001 Harbin, China
[2]Harbin University, 150086 Harbin, China

Received 4 December 2010; accepted in revised form 22 February 2011

Abstract. The paper investigates the effect of voids and hygrothermal conditions on bending, compressive, and interlaminar shear strength (ILSS) of T300/914 composite laminates. By adopting different autoclave pressures during a cure cycle, specimens with three different void contents ranging from 0.33% to 1.50% were obtained. Experimental results reveal that compressive, bending strength, and ILSS decrease with increasing void contents and immersion time. The most significant decrease in strength of aged specimens is in the ILSS and compressive strength, followed by the bending strength. The effect of voids on the absorption/desorption behavior is also discussed. For a similar porosity, the compressive strength and ILSS of dried specimens are higher than that of the aged specimens, while they are lower than that of the unaged specimens. The bending strength of the dried specimens is higher than that of the unaged specimens. The experimental results are explained by the supportive micrographs that illustrate different types of voids and their morphology before and after moisture absorption/desorption.

Keywords: *mechanical properties, laminates, porosity, moisture absorption, carbon fiber*

1. Introduction

Manufacturing defects, particularly voids are among the most common manufacturing induced defects in composites [1, 2]. In polymeric composite materials, voids always have detrimental effects on the mechanical properties [3–5]. In general, voids have detrimental effects on the strength and fatigue life of composite laminates. Furthermore, voids cause a greater susceptibility to water penetration and environmental conditions [3].

Costa *et al.* [3] indicated that the ILSS values decreases with the void content of the carbon/epoxy laminates and carbon/BMI (bismaleimide) laminates. Chambers *et al.* [5] reported that increasing void content reduces both flexural strength and fatigue performance by acting both on the initiation and propagation stages of failure. de Almeida and Nogueira Neto [6] indicated that voids may cause a remarkable decrease in fatigue life despite having only a moderate influence on the static strength.

Composite aircraft structures are usually exposed to a range of hygrothermal conditions through their designed service life, which causes degradation in material properties of CFRP laminates. For polymer composites, moisture often causes swelling and degradation. The material degradation includes chemical changes of the matrix materials and debonding at the fiber/matrix interface. Long-term exposure at high temperatures is also a concern for CFRP, as higher temperatures accelerate diffusion rates of moisture and generally accelerate aging [7, 8].

*Corresponding author, e-mail: dongxingzhang@163.com

Costa *et al.* [3, 9] indicated that voids in polymer matrix composites may result in significant reductions in matrix dominated mechanical properties such as interlaminar shear, compressive, and flexural strengths. Voids affect the same mechanical properties affected by environmental conditions. Costa *et al.* [3] also indicated that moisture absorption has been shown to lead to general reduction of the mechanical properties of composites. This has been attributed, in part, to the degradation of the fiber/matrix interfacial bond. Jedidi *et al.* [10] reported that polymer matrix composites undergo dimensional and stress state changes due to moisture induced swelling and thermal expansion in hygrothermal environment. Gigliotti *et al.* [11] indicated that temperature differentials and moisture absorption induce swelling in the material: then the heterogeneity of the hygrothermal fields and of the material are responsible for stress both at the micro and the macroscale. Cândido *et al.* [12] also reported that moisture absorption may induce mechanical and physical-chemical changes that toughen the polymeric matrix and/or deteriorate matrix/fiber by interfacial debonding or micro-cracking. The degradation of physical and mechanical properties has been found to depend primarily upon the total amount of moisture absorbed. Meziere *et al.* [13] reported that humidity has an influence on the fiber/matrix interface as well as the matrix properties. The behavior of any composite depends on the efficiency of the fiber/matrix interface which can be reduced by the presence of water.

As described above, many previous literatures have studied the effect of voids on the mechanical strength of unidirectional fiber composite materials under hygrothermal conditions. However, studies evaluating the mechanical performance of woven carbon/epoxy laminates under moisture absorption/desorption conditions are scarce.

This research was aimed to characterize the voids in woven carbon fiber materials and to investigate the effect of void content on compressive, bending, and interlaminar shear strength (ILSS) of T300/914 laminates that are kept at room temperature, hygrothermal, and dry environments, respectively. In this paper, a series of experiments was carried out to study the effects of void content on the hygrothermal and desorption behaviors of carbon/epoxy laminates.

2. Experimental

2.1. Raw materials and specimens preparation

The specimens were fabricated from commercially available (Hexcel Composites Ltd., Stamford,CT, USA) carbon/epoxy pre-impregnated tapes. The tapes were made of T300 carbon fibers pre-impregnated with Hexcel 914 epoxy resin (fiber volume fraction of 58%). The material was laid up by hand in 270mm × 300 mm woven laminates $[(\pm 45)_4/(0,90)/(\pm 45)_2]_S$. Each laid-up stack was fit into a vacuum bag and placed in an autoclave for curing. The laminates were cured with a ramp of 1.5°C/min from room temperature to 135°C, and then held at 135°C for 0.5 h prior to being ramped to 180°C at 1.5°C/min. The laminates were further held at 180°C for 2.5 h. Finally, they were ramped to 45°C to produce the final composite laminates. In addition, each step was conducted in a vacuum bag of 0.06 MPa.

Using the described procedure to produce the compressive, bending, and ILSS samples, specimens with three different porosity levels ranging from 0.33 to 1.50% were obtained by employing autoclave pressures of 0.4, 0.2 and 0.0 MPa.

An experimental program to characterize the effect of voids on the strength of T300/914 laminates was presented. Three conditions were used in this study: (a) ambient conditions: the specimens were kept at room temperature, defined as unaged specimens; (b) hygrothermal conditions: the specimens were dried in an oven at 70°C until their weights were stabilized and then (the now engineering dry specimens) were immersed in distilled water at 70°C until reaching a saturated moisture content, defined as aged specimens; and (c) dried conditions: the aged specimens were dried in an oven at 70°C until reaching equilibrium, defined as dried specimens.

2.2. Morphology and structure observation

The distribution, shape, and location of voids in the unaged and aged laminates were observed with a metallurgical microscope (VNT-100, Visual New Technology Developing Co., Ltd, Beijing, China). The specimens were carefully prepared for microstructural analysis using a polishing regime beginning with grade silicon carbide abrasive paper, and ending with 1 μm diamond paste. The microscope was then used to analyze the pore morphology.

A scanning electron microscopy (SEM) STERED SCAN-240 (Sonatest Ltd, UK) was used to study the effect of moisture absorption on the microstructure of the water-immersed composite specimens. The fractographic examinations were carried out in detail on the compressive, bending, and ILSS fracture surfaces of specimens before and after moisture absorption.

2.3. Moisture absorption test procedure

Moisture absorption tests were carried out according to Chinese standard HB 7401-96. Prior to the moisture tests, all specimens were dried in an oven at 70°C until their weight became stable. The engineering dry specimens were immersed in distilled water at 70°C until reaching saturated moisture content. The change in weight of each specimen was measured as a function of immersion time. The specimen were removed from the water bath at regular intervals, wiped with filter paper to remove surface water, and then cooled back to room temperature before recording the weight and being placed back into water bath. The water content in the specimen was measured by the difference in weight throughout the moisture tests.

2.4. Mechanical tests

The compressive strength of T300/914 composite laminates was measured with an Instron 5582 mechanical testing machine (U.S. INSTRON Company, Norwood, MA, U.S.) in accordance with the Chinese standard GB/T3856-2005 procedure at a crosshead speed of 2 mm/min. The length, width, and the thickness of the compressive specimen were approximately 140, 6, 4.5 mm, respectively. Two different porosity levels ranging from 0.33 to 1.50% were obtained for the compressive specimen.

The three-point bending tests were performed with the MTS-810 multi-purpose machine in accordance with the Chinese standard GB/T3356-1999 at a loading rate of 5 mm/min. The rectangular specimens had the dimensions of 90 mm × 25 mm × 4.5 mm, where the span is 72 mm. Two different porosity levels ranging from 0.33 to 1.50% were obtained for the bending specimen.

The ILSS strength of the T300/914 composite laminates was measured with an Instron 5582 mechanical testing machine in accordance with the Chinese standard GB/T1450.1-2005 procedure at a crosshead speed of 2 mm/min. The rectangular specimens have the dimensions of 33 mm × 6 mm × 4.5 mm, with a span-to-thickness ratio of 5. Three different porosity levels ranging of 0.33, 0.71 and 1.50% were obtained for the ILSS specimen.

For statistical purposes, a total of five samples per condition were tested.

3. Results and discussion

3.1. Pore morphology analysis

A metallurgical microscope provides an excellent technique for examining the distribution, shape, and location of voids in the composite specimens. It is expected that the surface morphology of the moisture absorbed composite specimen will be different from that of dry composite specimens, particularly in terms of voids, porosity, swelling, sorption in micro-cracking, and disbanding around filler. The pores can act as stress concentration points, and lead to premature failure of the composites during loading. Therefore, studies of the composite surface topography provide vital information on the level of interfacial adhesion that exists between the fiber and matrix when used as reinforcement in wet conditions [14].

Figure 1 shows the microstructural morphology of voids in the carbon/epoxy laminate which was kept at room temperature. As shown in Figure 1a) and b), where the porosity ranged from 0.33 to 0.71%, the typically spherical voids were mostly, and preferentially located at the resin rich areas. As shown in Figure 1c), when porosity increased to 1.50%, elongated or elliptical voids appeared in the resin along the fiber/matrix interface. Some voids were typically located at the crossing of the woven fiber tows, therefore having a triangular shape within the resin rich areas. It could be seen that the larger voids tended to be relatively aligned in the fiber direction.

Figure 2 illustrates the pore morphology of the aged specimens. As shown in Figure 2a), when the porosity is 0.33%, the aged specimens present minor cracks from the fiber/matrix interface. Figure 2b) and c) show that matrix cracks and interlaminar cracks emanate from the void, and propagate longitudinally along the fiber/matrix interface. Damage evolution of the aged specimen was primarily caused by the debonding of the fiber/matrix inter-

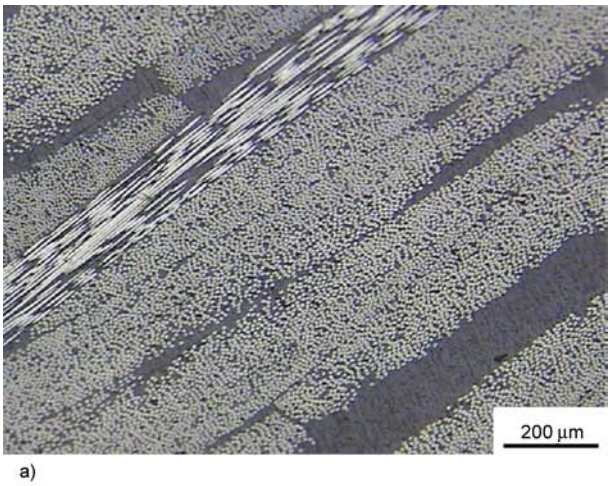

Figure 1. Morphology and structure of the unaged specimens with different void content. a) Porosity of 0.33%, b) porosity of 0.71%, c) porosity of 1.50%.

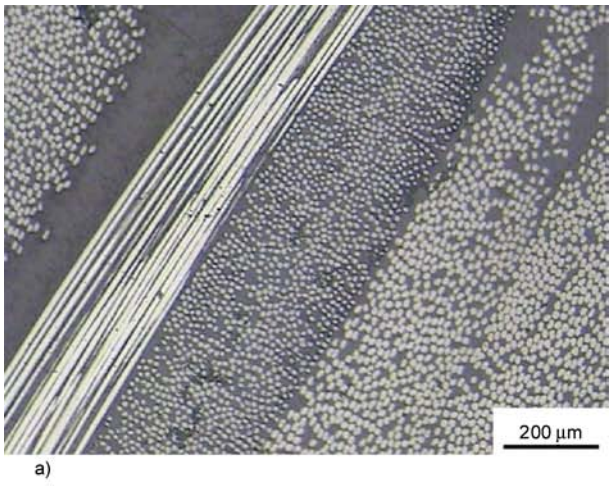

Figure 2. Pore morphology of the aged specimens with different porosity. a) Porosity of 0.33%, b) porosity of 0.71%, c) porosity of 1.50%.

face. Voids could potentially amplify the effects of moisture absorption in the laminate, and introduce high stress concentrations that facilitate the development of microcracks [9]. Moisture absorption accelerates the damage propagation in the composite. With the same porosity, a greater number of matrix cracks and interfacial cracks were observed in the aged specimens in comparison to the unaged specimens (as shown in Figure 1).

3.2. Compressive strength test

The presence of moisture within polymeric composites often degrades their physical and mechanical properties [12, 15]. As shown in Figure 3, with the porosity increasing from 0.33 to 1.50%, the compressive strength of unaged and aged specimens decreased 4.3 and 10.8%, respectively. Compared with the unaged specimens, the compressive strength of aged specimens decreased 14.6 and 20.4%, with respective porosities of 0.33 and 1.50%, respectively.

A compressive test is principally driven by the behavior of the resin and the fiber/matrix interfaces, especially in hygrothermal aging conditions. Costa *et al.* [9] indicated that the water absorbed by the laminates causes either reversible or irreversible plasticization of the matrix. Combined with the temperature effects, these factors may cause significant changes in the matrix toughness, affecting the laminate strength. These factors reduce the load transfer capacity of the interface.

Figure 4 shows the compression fractures of fiber, interfacial cracks, and fiber buckling, leading to an irregular, 'stepped' fracture surface. This is a characteristic feature of compression failure.

As shown in Figure 5, the general trend of the compressive strength decreased with increasing porosity, and the compressive strength of dried specimens was higher than that of aged specimens in the case of similar porosity. The water absorbed by the laminates caused reversible swelling and a plasticization effect on the matrix, which was usually recoverable after drying.

Compared to unaged specimens, the compressive strength retention of the dried specimens were 90.4 and 81.6% with a porosity of 0.33 and 1.50%, respectively. The compressive strength of the dried specimens was lower than that of the unaged specimens for the same porosity. Water absorption in the laminates, combined with external or internal stresses (caused by loading or thermo-elastic effects), instigated crack propagation and hydrolysis in the resin

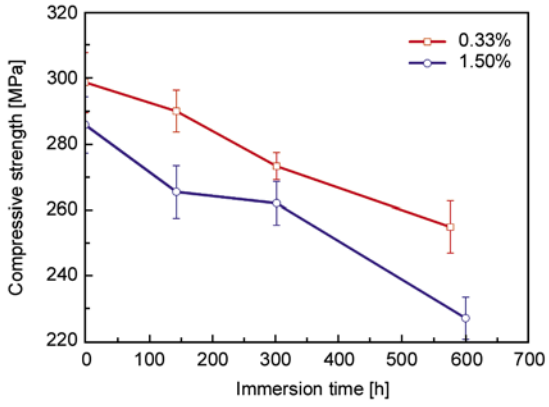

Figure 3. Compressive strength curves of the aged specimens with different porosity

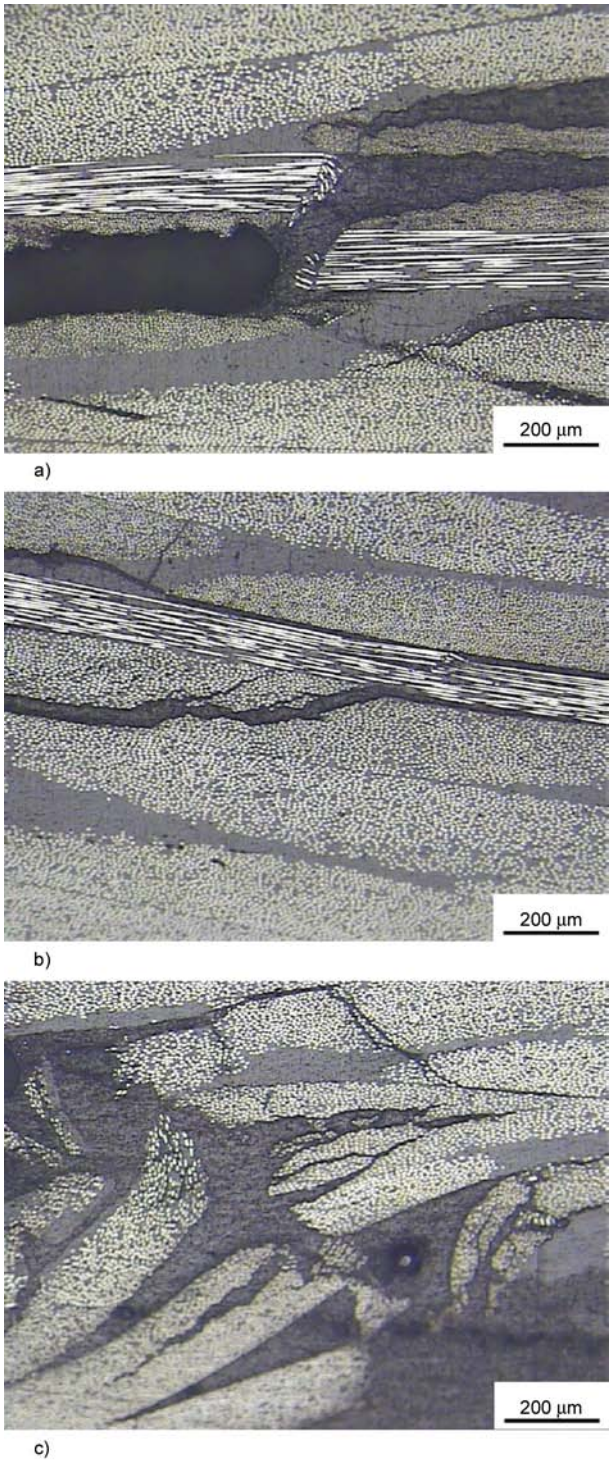

Figure 4. Pore morphology of the aged compressive specimens. a) Fiber compressive fractures, b) interfacial cracks, c) fiber buckling.

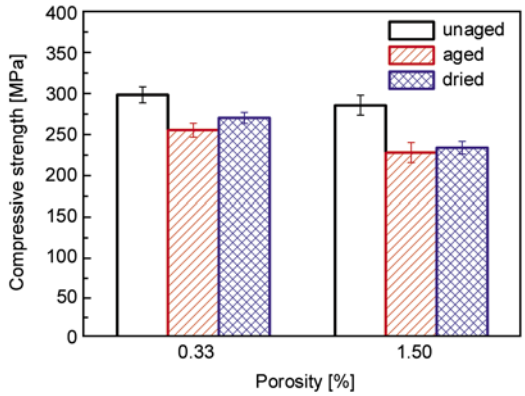

Figure 5. Compressive strength in different conditions of different porosity

matrix. The composite undergoes permanent weakening and its strength cannot be recovered after drying.

3.3. Bending strength test

As shown in Figure 6, with the porosity increasing from 0.33 to 1.50%, the bending strength of unaged and aged specimens decreased 7.2 and 9.8%, respectively. The reduction in net section combined with the increase in void content had a detrimental effect on strength.

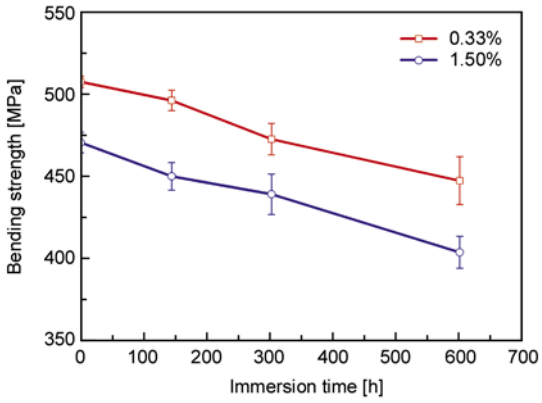

Figure 6. Bending strength curves of the aged specimens with different porosity

Compared to the unaged specimens, the bending strength of the aged specimens decreased 11.8 and 14.2% with porosity of 0.33 and 1.50%, respectively. Water absorption and its resulting effects contribute to the loss of compatibility between the fibers and matrix, which resulted in debonding and weakening of the interfacial adhesion [16]. The interface and the effects of environmental conditions on its strength play a major role in determining the strength of composite laminates in the presence of moisture [9].

Figure 7 illustrates that the damage of the tensile side of the aged failed bending specimens was more severe than that of the compressive side. Matrix cracks, fiber breakage and the interfacial cracks were observed in the tensile side of the aged failed bending specimens.

The delamination and cracks act like pores, which allow the further diffusion of water and chemicals and causes degradation. The delamination and cracks in the matrix weaken the load transfer between the fibers, and additional harmful chemicals diffuse to the interface between the fiber and matrix. Consequently, the interface between the fiber and matrix is weakened, reducing the mechanical performance [17].

Figure 8 shows that the bending strength of the aged specimens was lower than that of the unaged specimens for similar porosity. This could be due to the fact that the immersion of composites specimens at

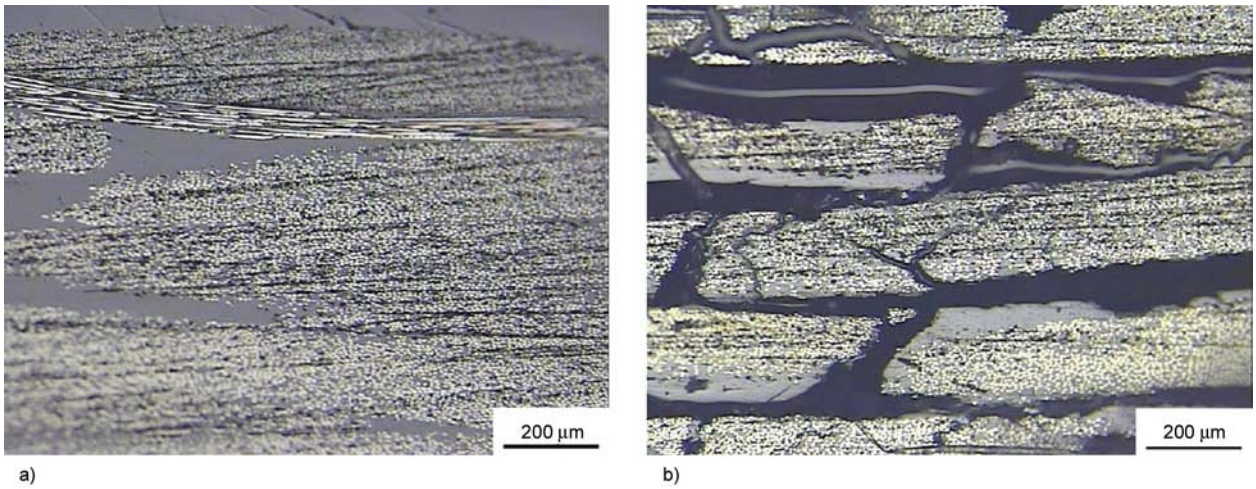

Figure 7. Micrographs of the aged failed bending specimens. a) Compressive side, b) tensile side

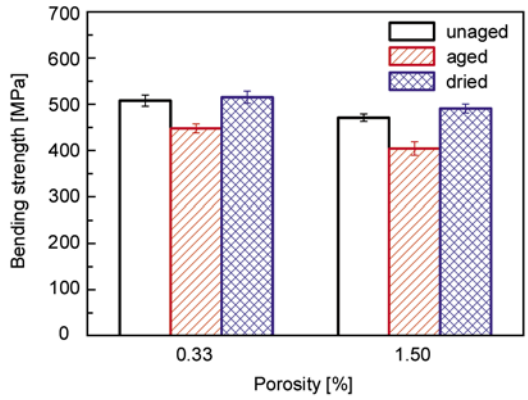

Figure 8. Bending strength in different conditions of different porosity

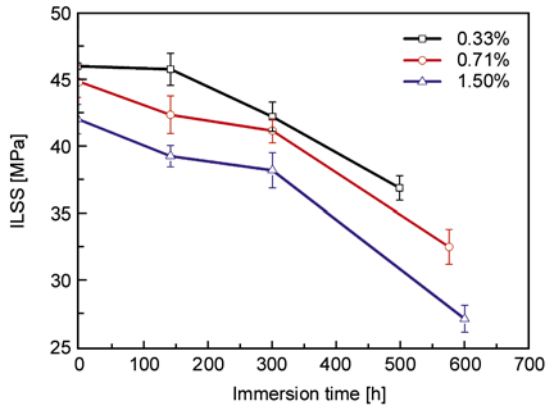

Figure 9. ILSS curves of the aged specimens with different porosity

water affected the interfacial adhesion between the fiber and matrix and created the debonding leading to a decrease in the mechanical properties of the composites. As shown in Figure 8, the general trend of the bending strength of dried specimens decreased with the increase of porosity. Furthermore, the bending strength of dried specimens was higher than that of the unaged specimens for similar porosity. This may be due to the dry conditions leading to an increase of the curing degree, which eliminated some of the residual stress and improved the adhesion of the fiber/matrix interface.

3.4. ILSS test

As seen in Figure 9, with the porosity increasing from 0.33 to 1.50%, the ILSS of the unaged and aged specimens decreased 8.6 and 26.2%, respectively. Compared to the unaged specimens, the interlaminar shear strength of the corresponding aged specimens decreased 19.7, 27.4, and 35.2% with porosity of 0.33, 0.71, and 1.50%, respectively.

It is observed in Figure 9 that ILSS dropped incrementally in hygrothermal conditions as immersion time increased. Moisture absorption and high temperature cause plasticization of the matrix which changes its toughness. Moreover, humidity and temperature cause dimensional changes and induce stresses in the laminate that degrade the fiber/matrix interface [9]. The ILSS test is principally driven by the behavior of the resin and the fiber/matrix interfaces, which are particularly affected by hygrothermal aging. As shown in Figure 9, the ILSS of aged specimens indeed decreases with the immersion time.

Figure 10a shows that matrix cracks, interlaminar cracks, and further crack propagation were observed in the aged ILSS failure specimens with a porosity of 0.33%. As shown in Figure 10b, an apparent

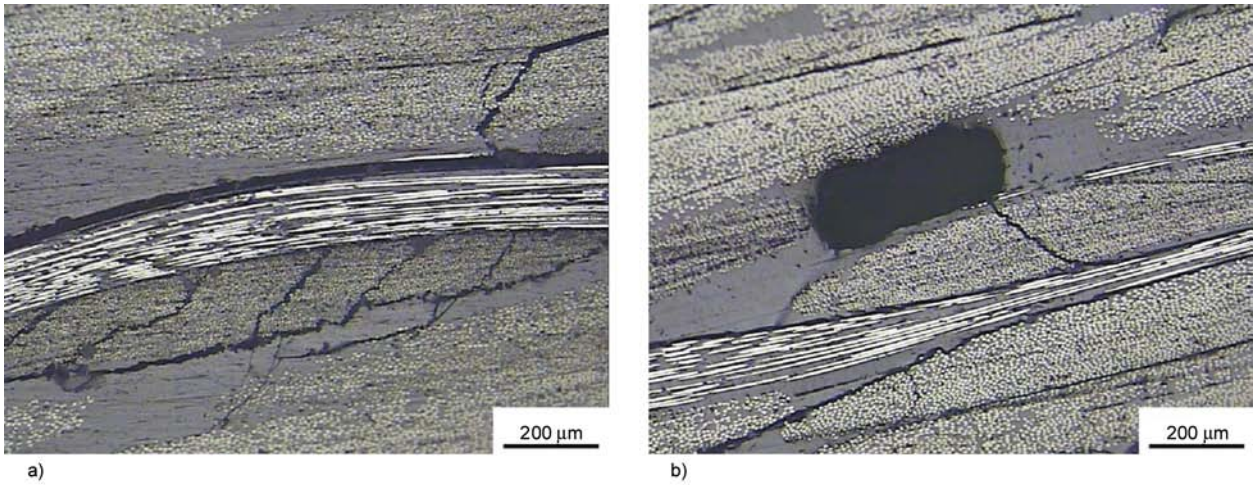

Figure 10. Pore morphology of the aged ILSS failed specimens with different porosity. a) Porosity of 0.33%, b) porosity of 1.50%.

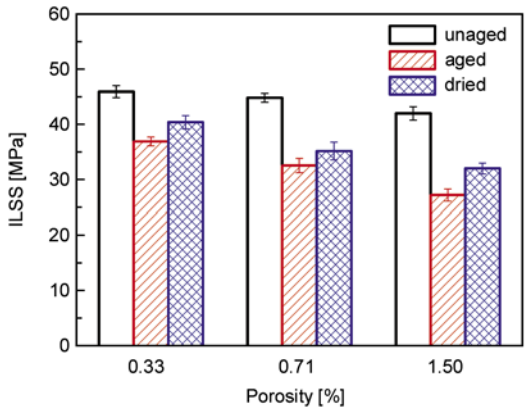

Figure 11. ILSS in different conditions of different porosity

matrix crack was initiated from a void and extended to the fiber/matrix interface in the aged ILSS failure specimens with a porosity of 1.50%.

A decrease in the ILSS with increasing porosity was observed for all the T300/914 laminates in Figure 11. Compared to the unaged specimens, the ILSS retention of dried specimens was 87.9, 78.5, and 76.3% with porosities of 0.33, 0.71, and 1.50%, respectively. For the same porosity, the ILSS of dried specimens was lower than that of the unaged specimens but higher than that of the aged specimens for similar porosity.

4. Conclusions

A series of experiments were conducted to separate qualitatively the effect of voids on the static mechanical properties of hygrothermal conditioned carbon/epoxy composites. Through systematic investigation, there were three conclusions to be drawn. (1) Moisture absorption led to an acceleration of damage to the composite. For similar porosity, a higher concentration of matrix crack and interfacial crack were observed in the aged specimens than in the unaged specimens. (2) The general trend of the compressive, bending, and interlaminar strength of the unaged, aged and dried specimens decreased with the increase of porosity and immersion time. The most significant decrement in the strength of the aged specimens was in the ILSS and compressive strength, with the reduction of the bending strength being less prominent. The ILSS and compressive strength tests were principally driven by the behavior of the resin and the fiber/matrix interfaces, which are particularly affected by hygrothermal aging. (3) For similar porosity, the compressive strength and ILSS of the dried specimens was higher than that of the aged specimens, but lower than that of the unaged specimens. However, the bending strength of the dried specimens was higher than that of the unaged specimens.

Acknowledgements

The authors are gratefully to the Harbin Aircraft Industry Group for supporting this work.

References

[1] Puglia P. D., Sheikh M. A., Hayhurstb D. R.: Classification and quantification of initial porosity in a CMC laminate. Composites Part A: Applied Science and Manufacturing, **35**, 223–230 (2004). DOI: 10.1016/j.compositesa.2003.09.026

[2] Birt E. A., Smith R. A.: A review of NDE Methods for porosity measurement in fiber-reinforced polymer composites. Non-Destructive Testing and Condition Monitoring, **46**, 681–686 (2004).

[3] Costa M. L., de Almeida S. F. M., Rezende M. C.: The influence of porosity on the interlaminar shear strength of carbon/epoxy and carbon/bismaleimide fabric laminates. Composites Science and Technology, **61**, 2101–2108 (2001). DOI: 10.1016/S0266-3538(01)00157-9

[4] Wisnom M. R., Reynolds T., Gwilliam N.: Reduction in interlaminar shear strength by discrete and distributed voids. Composites Science and Technology, **56**, 93–101 (1996). DOI: 10.1016/0266-3538(95)00128-X

[5] Chambers A. R., Earl J. S., Squires C. A., Suhot M. A.: The effect of voids on the flexural fatigue performance of unidirectional carbon fibre composites developed for wind turbine applications. International Journal of Fatigue, **28**, 1389–1398 (2006). DOI: 10.1016/j.ijfatigue.2006.02.033

[6] de Almeida S. F. M., Nogueira Neto Z. S.: Effect of void content on the strength of composite laminates. Composite Structure, **28**, 139–148 (1994). DOI: 10.1016/0263-8223(94)90044-2

[7] Aokia Y., Yamada K., Ishikawa T.: Effect of hygrothermal condition on compression after impact strength of CFRP laminates. Composites Science and Technology, **68**, 1376–1383 (2008). DOI: 10.1016/j.compscitech.2007.11.015

[8] Tsai Y. I., Bosze E. J., Barjasteh E., Nutt S. R.: Influence of hygrothermal environment on thermal and mechanical properties of carbon fiber/fiberglass hybrid composites. Composites Science and Technology, **69**, 432–437 (2009). DOI: 10.1016/j.compscitech.2008.11.012

[9] Costa M. L., Rezende M. C., de Almeida S. F. M.: Strength of hygrothermally conditioned polymer composites with voids. Journal of Composite Materials, **39**, 1943–1961 (2005).
DOI: 10.1177/0021998305051807

[10] Jedidi J., Jacquemin F., Vautrin A.: Design of accelerated hygrothermal cycles on polymer matrix composites in the case of a supersonic aircraft. Composite Structure, **68**, 429–437 (2005).
DOI: 10.1016/j.compstruct.2004.04.009

[11] Gigliotti M., Jacquemin F., Molimard J., Vautrin A.: Transient and cyclical hygrothermoelastic stress in laminated composite plates: Modelling and experimental assessment. Mechanics of Materials, **39**, 729–745 (2007).
DOI: 10.1016/j.mechmat.2006.12.006

[12] Cândido G. M., Costa M. L., Rezende M. C., Almeida S. F. M.: Hygrothermal effects on quasi-isotropic carbon epoxy laminates with machined and molded edges. Composites Part B: Engineering, **39**, 490–496 (2008).
DOI: 10.1016/j.compositesb.2007.03.007

[13] Meziere Y., Bunsell A. R., Favry Y., Teissedrea J-C., Do A. T.: Large strain cyclic fatigue testing of unidirectional carbon fibre reinforced epoxy resin. Composites Part A: Applied Science and Manufacturing, **36**, 1627–1636 (2005).
DOI: 10.1016/j.compositesa.2005.03.020

[14] Athijayamani A., Thiruchitrambalam M., Natarajan U., Pazhanivel B.: Effect of moisture absorption on the mechanical properties of randomly oriented natural fibers/polyester hybrid composite. Materials Science and Engineering: A, **517**, 344–353 (2009).
DOI: 10.1016/j.msea.2009.04.027

[15] Costa M. L., Rezende M. C., de Almeida S. F. M.: Effect of void content on the moisture absorption in polymeric composites. Polymer-Plastics Technology and Engineering, **45**, 691–698 (2006).
DOI: 10.1080/03602550600609549

[16] Kim H. J., Seo D. W.: Effect of water absorption fatigue on mechanical properties of sisal textile-reinforced composites. International Journal of Fatigue, **28**, 1307–1314 (2006).
DOI: 10.1016/j.ijfatigue.2006.02.018

[17] Won J-P., Lee S-J., Kim Y-J., Jang C-I., Lee S-W.: The effect of exposure to alkaline solution and water on the strength–porosity relationship of GFRP rebar. Composites Part B: Engineering, **39**, 764–772 (2008).
DOI: 10.1016/j.compositesb.2007.11.002

eXPRESS Polymer Letters Vol.5, No.8 (2011) 717–731
Available online at www.expresspolymlett.com
DOI: 10.3144/expresspolymlett.2011.70

Poly(ester amide) nanocomposites by in situ polymerization: Kinetic studies on polycondensation and crystallization

L. Morales-Gámez[1,2], *I. Jones*[1], *L. Franco*[1,2], *J. Puiggalí*[1,2*]

[1]Departament d'Enginyeria Química, Universitat Politècnica de Catalunya, Av. Diagonal 647, E-08028, Barcelona, Spain
[2]Centre de Recerca en NanoEnginyeria (CRNE), Universitat Politècnica de Catalunya, Edifici C', c/ Pascual i Vila s/n, E-08028, Barcelona, Spain

Received 16 December 2011; accepted in revised form 28 February 2011

Abstract. Preparation of nanocomposites by in situ polymerization of sodium chloroacetylaminohexanoate in the presence of Cloisite 20A (C20A) or Cloisite 30B (C30B) organo-modified montmorillonites was studied. Both clays rendered an intercalated structure that contrasts with the exfoliated structure previously found with the use of the C25A montmorillonite. Polymerization under non-isothermal and isothermal conditions was evaluated by Wide Angle X-ray Diffraction (WAXD) synchrotron radiation and Fourier Transform Infrared Spectroscopy (FTIR) experiments. Results indicate that C20A and C30B had a similar influence on the polymerization kinetics. Thus, the activation energy and the Arrhenius pre-exponential factor decreased compared to those calculated for the neat monomer. Clear differences were also found when using the C25A clay since, in this case, polymerization had similar activation energy to that determined for the neat monomer. The crystallization kinetics of the intercalated C20A and C30B nanocomposites was studied by FTIR and optical microscopy. The incorporation of clay particles increased the overall rate kinetic constant due to the enhancement of the primary nucleation. On the contrary, the spherulitic growth rate was slightly disfavored by the clay.

Keywords: *nanocomposites, in situ polymerization, poly(ester amide), polymerization kinetics, crystallization kinetics*

1. Introduction

The preparation of new polymer nanocomposites is a promising topic since material properties can be enhanced and their range of applications extended by using molecular or nanoscale reinforcements rather than conventional fillers [1–5]. Since the first works performed with nylon 6 [6, 7], several polymer based systems and preparation methodologies such as melt-mixing, solution intercalation and *in situ* polymerization have been developed. Results clearly demonstrate that properties of the neat polymer like water-absorption rate, thermal-expansion coefficients, Young modulus, thermal stability and gas barrier effect can be improved by the incorporation of a small amount of clay, and also that the crystallization kinetics can be affected.

Layered silicate particles are especially interesting for nanocomposite preparation as they may be dispersed into individual layers with a thickness close to 1 nm to tune surface interactions with the polymer/monomer through exchange reactions with organic and inorganic cations [8]. The final structure of the composite depends on the extent to which the organic matrix and inorganic clay components are made compatible [9], and varies from an intercalated to a fully exfoliated nanostructure, which has an obvious impact on the final properties. Despite extensive research, the influence of nano-

*Corresponding author, e-mail: Jordi.Puiggali@upc.es

composite structure on nucleation and crystal growth rate is not entirely clear in view of the conflicting results reported in some cases [10–14].

Aliphatic poly(ester amide)s constitute a promising family of materials since the presence of hydrolyzable ester groups may enhance degradability, and the establishment of intermolecular hydrogen bonding interactions between amide groups may provide suitable thermal and mechanical properties for most applications [15–19]. Furthermore, several monomers and synthetic routes have been developed to obtain materials with variable composition and chemical microstructure, which can consequently meet numerous requirements. The alternating poly(ester amide) derived from glycolic acid and 6-aminohexanoic acid (poly(glc-*alt*-amh)) has recently received attention for two main reasons: a) The simple synthesis procedure based on only two reaction steps (Figure 1a), and b) A composition based on the main units of biodegradable polyesters (glycolic acid) and aliphatic polyamides (6-aminohexanoic acid).

Poly(glc-*alt*-amh)) is obtained by a thermal polycondensation reaction based on the formation of a metal halide salt as the driving force of the condensation reaction [20, 21], which seems an appropriate procedure to prepare nanocomposites by in situ polymerization. This is a highly attractive technique due to its versatility and compatibility with various reactive monomers, making it a valuable process for commercial applications [22, 23]. Several examples in the literature concern the preparation of polystyrene [24], polycaprolactone [25] and nylon 6 [26] nanocomposites.

The *in situ* polymerization technique was effective and rendered practically exfoliated nanocomposites of poly(glc-*alt*-amh) and the Cloisite 25A (C25A) organo-modified montmorillonite [27]. Typical calorimetric techniques were not suitable for proper evaluation of the polymerization kinetics at temperatures lower than 145ºC due to the overlapping of the exothermic polymerization peak with an endothermic peak associated with polymer crystallization. Thus, Fourier Transform Infrared Spectroscopy (FTIR) was a basic tool to compare and study the influence of clay particles on the polymerization kinetics. Nanocomposites prepared by the above in situ polymerization and the melt mixing technique gave rise to two different structures (i.e. exfoliated and intercalated) that clearly influenced the crystallization kinetics [27, 28]. The main purpose of the present work is to determine the effect of montmorillonites based on two different surfactants (Closites 30B and 20A) on *in situ* polymerization and to study the crystallization kinetics of the derived nanocomposites. The polymerization kinetics is evaluated through real-time synchrotron and FTIR experiments whereas the crystallization kinetics is studied through FTIR to obtain the overall crystallization rate and optical microscopy measurements to determine the nucleation and crystal growth rates.

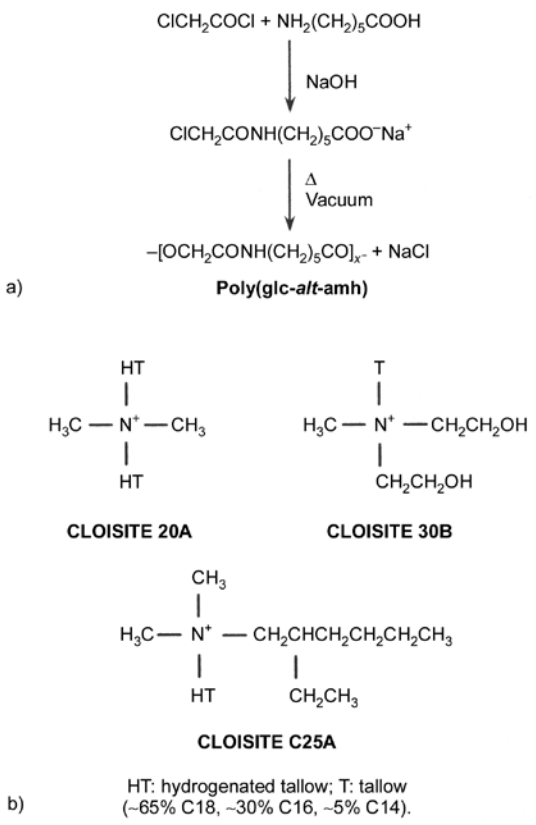

Figure 1. a) Synthesis scheme for the poly(ester amide) studied in this work. b) Chemical structure of Closites 20A, 25A and 30B

2. Experimental section

2.1. Materials

The monomer, sodium chloroacetylaminohexanoate, was synthesized following a previously reported method [20, 21]. All reagents and solvents were purchased from Aldrich Chemical Company, (Milwaukee, WI, USA) and used as received. Polymerization was based on a thermal polycondensation which rendered sodium chloride as a byproduct (Figure 1a) [20, 21].

The nanocomposites were based on two organo-modified layered phyllosilicates: methyl tallow bis(2-hydroxyethyl) ammonium montmorillonite (Closite 30B, Southern Clay Products, MT2EH, Gonzales, Texas, USA) and dimethyl dihydrogenated-tallow ammonium montmorillonite (Closite 20A, Southern Clay Products, 2MH2HT, Gonzales, Texas, USA). Results are also compared with those previously obtained with Closite 25 A (Southern Clay Products, 2MHTEX, Gonzales, Texas, USA) [27]. The chemical structure of all employed montmorillonite surfactants is shown in Figure 1b.

2.2. Preparation of nanocomposites

For both nanocomposite preparations, 10 mg of monomer was dissolved in 10 ml of water, and separately, the appropriate clay was dispersed in water (< 0.1 wt%). The monomer solution and clay dispersion were stirred for two hours, and then mixed and liophilized. The ratio of the solution and dispersion was conveniently adjusted to obtain a clay content of 3 wt% in the final solid. Polymerization was carried out by heating the monomer/clay mixture to 160ºC. A white solid was recovered and extensively washed with water, methanol and acetone. This procedure was similar to that performed with Cloisite 25A. For comparison purposes, polymerization without organoclay was also performed and the final sample purified as above.

No significant differences were found between the molecular weights of the neat poly(ester amide), the two new prepared nanocomposites and that derived from C25A. Thus, weight average molecular weight (M_w) and number average molecular weight (M_n) were always in the 14 000–17 000 and 37 000–43 000 ranges, respectively, according to Gel Permeation Chromatography (GPC) measurements using 1,1,1,3,3,3-hexafluoroisopropanol as the solvent and poly(methyl methacrylate) standards.

2.3. Measurements

Interlayer spacing of the clay was studied by Wide Angle X-ray Diffraction (WAXD) using a Siemens D-500 diffractometer (Karlsruhe, Germany) with Cu K_α radiation (λ = 0.1542 nm).

The structure and distribution of Cloisite were observed with a Philips TECNAI 10 (FEI/Philips Electron Optics, Eindhoven, Netherlands) transmission electron microscope (TEM) at an accelerating voltage of 100 kV. TEM specimens were prepared by embedding in a low viscosity modified Spurr epoxy resin and curing at 40°C for a few days and then at 60°C for 6 h. Ultrathin sections (less than 100 nm) were cut at room temperature using a Sorvall Porter-Blum microtome (Sorvall Products, Newton, CT, USA) equipped with a diamond knife. Finally, the sections were collected in a trough filled with water and lifted onto carbon coated copper grids. In order to prevent diffusion of the epoxy resin into the polymer film, a thin layer of carbon was evaporated over the film surface.

The spherulitic growth rate was determined by optical microscopy using a Zeiss Axioskop 40 Pol light polarizing microscope (Carl Zeiss Microlmaging, GmbH, Germany) equipped with a Linkam temperature control system configured by a THMS 600 heating and freezing stage (Linkam, Scientific Instruments, Guilford Surrey, United Kingdom) connected to a Liquid Nitrogen Pump (LNP 94). Spherulites were grown from homogeneous melt-crystallized thin films produced by melting 1 mg of the polymer mixture on microscope slides. Next, small sections of these films were pressed or smeared between two cover slides and inserted in the hot stage. The thicknesses of the squeezed samples were close to 10 μm in all cases. Samples were kept at 170ºC (more than 10ºC above the polymer melting point of 157ºC) for 5 minutes to wipe out sample history effects, and then quickly cooled to the selected crystallization temperature. The radius of the growing spherulites was monitored during crystallization by taking micrographs with a Zeiss AxiosCam MRC5 digital camera (Carl Zeiss Microlmaging, GmbH, Germany) at appropriate time intervals. A first-order red tint plate was employed to determine the sign of spherulite birefringence under crossed polarizers.

Time-resolved WAXD experiments were carried out at the Collaborating Research Group (CRG) beamline BM16 of the European Synchrotron Radiation Facility (ESRF) of Grenoble. The beam was monochromatized to a wavelength of 0.098 nm. Monomer/clay samples were confined between Kapton films and then held in a Linkam hot stage with temperature control within 0.1ºC. WAXD profiles were acquired during polymerization and crystallization experiments in time frames of 12 s. The WAXD detector was calibrated with diffractions of

a standard of an alumina (Al_2O_3) sample. The diffraction profiles were normalized to the beam intensity and corrected considering the empty sample background. Deconvolution of WAXD peaks was performed with the PeakFit v4 program by Jandel Scientific Software using a mathematical function known as 'Gaussian area'.

Infrared absorption spectra were recorded with a Fourier Transform FTIR 4100 Jasco spectrometer (Jasco International Co. Ltd., Tokyo, Japan) in the 4000–600 cm^{-1} range. A Specac model MKII Golden Gate attenuated total reflection (ATR) with a heated Diamond ATR Top-Plate which can be used up to 200ºC, and a Series 4000 High Stability Temperature Controller were also utilized.

3. Results and discussion

3.1. Dispersion structure of C20A and C30B clays in the poly(glc-*alt*-amh) composites

C20A and C30B organo-modified clays were easily mixed with the sodium salt of *N*-chloroacetyl-6-aminohexanoic acid before performing thermal polycondensation at a temperature close to 160ºC. The final nanostructures were analyzed by X-ray diffraction and transmission electron microscopy. Evidence of intercalation of polymer chains into the silicate galleries can be obtained from diffraction patterns in the range of $2\theta = 1–10º$, when the characteristic silicate diffraction peaks appear at larger spacings than neat clay ones. Similarly, the absence of these peaks may suggest an exfoliated structure. Direct TEM morphological observation is always advisable to corroborate diffraction data although TEM images show a local distribution that also depends on how the sample was previously cut.

Direct observation of the morphology and phase distribution of ultrathin sections of poly(glc-*alt*-amh)/C20A specimens by transmission electron microscopy clearly showed that an intercalated structure was predominant (Figure 2a). X-ray diffraction profiles of the nanocomposite sample also revealed the existence of a low angle reflection associated with the stacking of silicate layers. The measured spacing was close to 3.58 nm, a higher value than that observed in the profile of C20A clay (2.52 nm). Thus, polymer chains in the nanocomposite sample were intercalated in the galleries of the dispersed clay and increased the interlayer spacing.

The poly(glc-*alt*-amh)/C30B nanocomposite showed that the 001 peak was significantly reduced and also shifted to a larger spacing (from 1.80 to 2.89 nm). A certain ratio of an exfoliated structure after polymerization seems to be produced. However, it should be noticed that this feature is only supported by the great decrease of the silicate reflection and a certain loose of the layer stacking order as shown in the electron micrograph of Figure 2b. Despite the final structure could be considered intercalated, a less regular layer disposition than poly(glc-*alt*-amh)/C20A samples was found.

Similar observations performed with Cloisite 25A indicated a well distinguished exfoliated structure from both X-ray and TEM observations. Thus, it

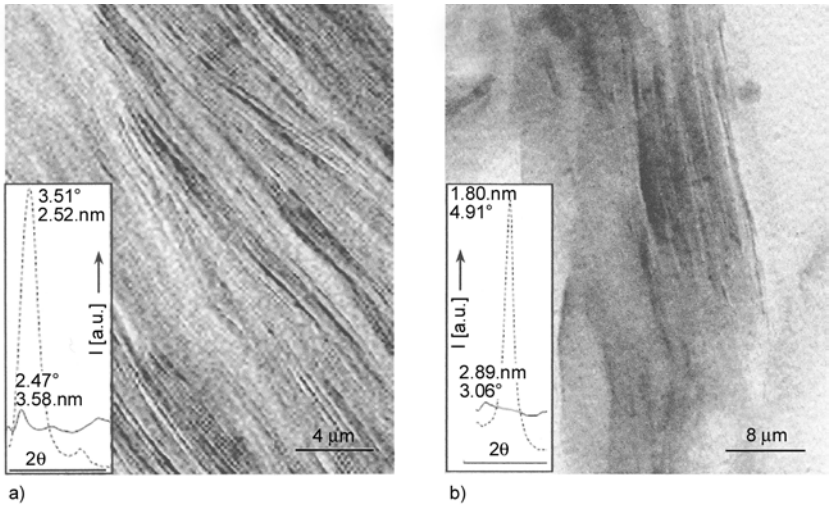

Figure 2. Transmission electron micrographs showing the morphology of the poly(glc-*alt*-amh)/C20A (a) and poly(glc-*alt*-amh)/C30B nanocomposites with a Cloisite concentration of 3%. Inset shows the diffraction peak associated with the interlayer spacing observed in the pure organo-modified clay (solid line) and the corresponding nanocomposite sample (dashed line).

became interesting to progress in polymerization and crystallization kinetics of new mixtures to get an insight into the effect of nanocomposite structure.

It is clear from the given experiments that monomer salts would be intercalated into the silicate galleries due to the good interactions with the cationic surfactants. Polycondensation reaction depends basically on the closeness between reactive groups (from monomer salts or the growing polymer chains) and should take place independently of the presence of quaternary ammonium cations of the organo-modifier. However, the surfactant is important since influences the spacing between silicate layers (i.e. the available space for polymer chains to growth inside the silicate galleries) and also on the interactions with the growing polymer. Cloisite 20B has the largest interlayer spacing and consequently the disruption of the layer stacking to render an exfoliated nanocomposite structure may be more difficult. Experimental results suggest that the expected good interactions between the carbonyl groups of the monomer/polymer and the two hydroxyl groups of the organo-modifier may still keep a close to intercalated nanocomposite structure despite the decrease on the silicate spacing. This feature cannot be considered when Closite C25A was employed and the structure of the nanocomposite became clearly exfoliated.

3.2. Non-isothermal polymerization of the sodium salt of N-chloroacetyl-6-aminohexanoic acid with C20A and C30B organo-modified clays

Synchrotron experiments were performed to compare the non-isothermal polymerizations of the monomer mixtures with each of the considered clays. The diffraction profiles initially showed the characteristic Bragg reflections of the monomer, which were most intense at values of the scattering vector, $q = (4\pi/\lambda)\cdot\sin\theta$, in the 14–17 nm^{-1} range (Figure 3). At a temperature close to 130ºC the monomer underwent a structural change, as evidenced by the variation in intensities and spacings of the main reflections (Figure 4). Note that the intensities of reflections close to 15.4 and 15.7 nm^{-1} increased and slightly decreased, respectively. The intensity increase is relevant since the occurrence of polycondensation reactions should lead to the destruction of the monomer crystal structure, and consequently to a gradual disappearance of all corresponding reflections.

At temperatures higher than 150ºC, the X-ray diffraction profiles showed the appearance of two peaks at $q \sim 19$ and 22 nm^{-1} of gradually increasing intensity (Figure 3). These, which could be indexed as the (100) and (110) reflections of the NaCl structure (~ 0.326 and 0.282 nm, respectively), demonstrated the occurrence of the polycondensation

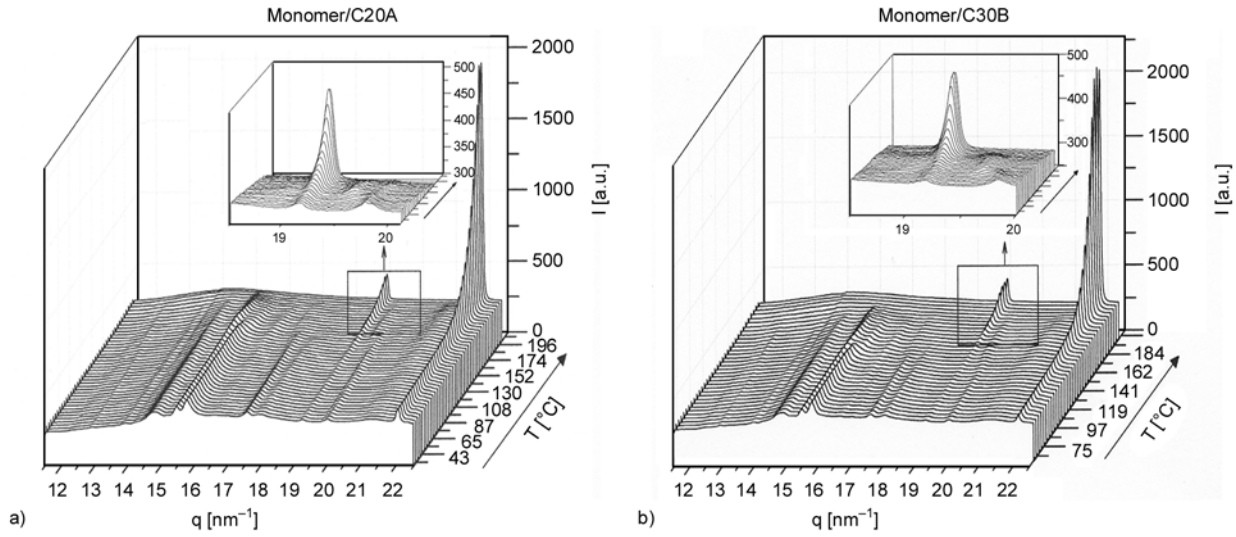

Figure 3. WAXD profiles taken during the non-isothermal polymerization performed at a heating rate of 20ºC/min with the monomer / C20A mixture (a) and the monomer / C30B mixture (b). Insets show the evolution of the weak (100) NaCl reflection.

reaction. Note that a delay between polymerization and formation of the inorganic salt crystal may occur since ions must move towards the growing crystal.

The evolution of NaCl peak intensities is useful to follow the polymerization process and even to demonstrate that polycondensation started in the solid state. It is worth pointing out that reflections related to the monomer structure were still visible when NaCl peaks developed. Logically these reflections became weaker when NaCl peaks started to increase and disappeared completely before these peaks reached maximum intensity. Diffraction profiles clearly revealed that the polymer was not able to crystallize under the assayed non-isothermal conditions since some of its characteristic reflections [29] were not detected. The polymer structure is defined by an orthorhombic unit cell having a = 0.477 nm, b = 0.873 nm and c = 1.057 nm and the corresponding diffraction pattern is characterized by strong Bragg reflections in the 14.4–16.2 nm^{-1} range. Specifically, the (020), (101), (110) and (111) reflections that appeared at 0.437, 0.435, 0.418 and 0.389 nm. At high temperature (190–200ºC) only an amorphous halo, the NaCl reflections and even small peaks attributed to (*hk*0) reflections of the clay were observed.

Figure 5 plots the area of the (100) NaCl peak versus temperature for the two studied polymerizations. A similar evolution was observed but, remarkably, some differences were detected, indicating that clay type has some influence on the polymerization kinetics. Specifically, the polymerization induction time was shorter when C20A clay was employed (i.e. the peak started to develop at temperatures of 110 and 140ºC for C20A and C30B,

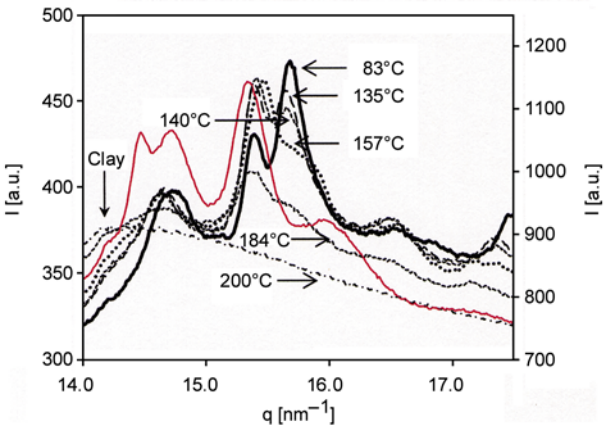

Figure 4. Representative WAXD profiles taken during a non-isothermal heating run (20ºC/min) performed with the monomer / C20A mixture and plotted in the q range where the main monomer reflections appeared (14–17.5 nm^{-1}). The selected temperatures correspond to the sample before (e.g. 83ºC) and after (e.g. 135ºC) occurrence of the monomer polymorphic transition, after being partially polymerized (e.g. 140, 157 and 184ºC) and at the end of the polycondensation reaction (e.g. 200ºC). In the last case only the amorphous halo and a small peak (see arrow) attributed to the clay could be observed. For the sake of completeness, the profile corresponding to a melt crystallized polymer sample taken at 140ºC is also shown (red curve).

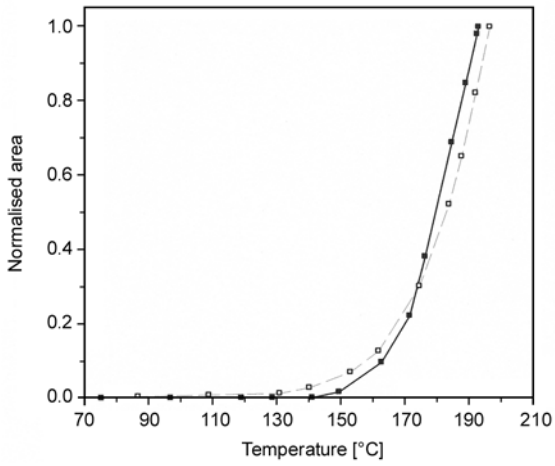

Figure 5. Intensity evolution of the (100) Bragg reflection of the NaCl structure (~ 0.326 nm) during non-isothermal polymerization (20ºC/min) of the monomer / C20A (□) and monomer / C30B (■) mixtures

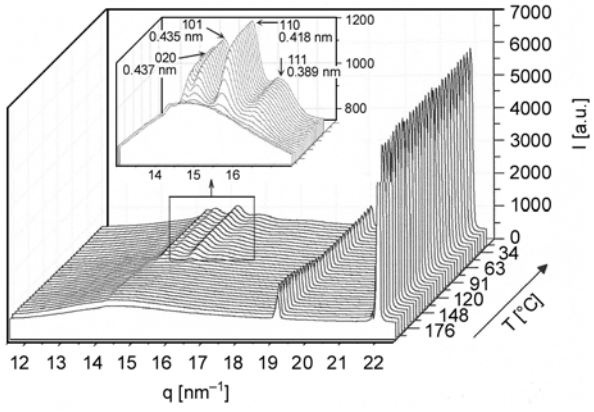

Figure 6. WAXD profiles taken during the non-isothermal crystallization performed at a cooling rate of 20ºC/min and after non-isothermal polymerization of the momomer/C20A mixture at a heating rate of 20ºC/min. Insets show a magnification of the Bragg reflections corresponding to the poly (glc-*alt*-amh) structure

respectively) whereas the reaction proceeded more rapidly when C30B was used (i.e. the peak developed in the 140–193 and 110–196ºC ranges for C20A and C30B, respectively).

X-ray diffraction patterns taken during a subsequent cooling run (e.g. Figure 6) revealed that polymerizations were successful since the mentioned characteristic diffraction peaks of poly(glc-*alt*-amh) [29] appeared and progressively increased in intensity. Logically, the intensity of NaCl peaks remained constant during the cooling run.

3.3. Isothermal kinetic analysis of *in situ* polymerization of C20A and C30B clay mixtures with *N*-chloroacetyl-6-aminohexanoic acid

The occurrence of the above monomer polymorphic transition and polymer crystallization should have endothermic/exothermic effects that make it impossible to evaluate the isothermal polymerization kinetics by DSC experiments. Note that these should only measure the exothermic enthalpy associated with the polycondensation reaction, which, in the studied case, is not possible due to the overlapping with the above processes. Thus, FTIR spectroscopy seems an ideal alternative technique given that the polymerization rate can be determined from the absorbance evolution of the new bonds that are formed.

The main changes in the FTIR spectra occurring during polymerization correspond to the appearance of a C=O absorption band at 1742 cm^{-1}, which is associated with the ester bond formed during polycondensation and a change in the wavenumber of the amide I absorption band (Figure 7). The latter should be found in both monomer and polymer samples but the different intermolecular hydrogen bond interactions should lead to a variation in the peak position and corresponding intensity.

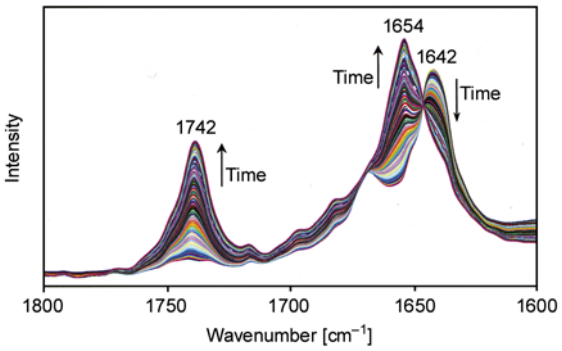

Figure 7. Absorbance FTIR spectra showing the evolution of the bands associated with the carboxylic ester group (1742 cm^{-1}) and amide I (1680–1620 cm^{-1}) during isothermal polymerizations of themomomer/C30B mixture at 110ºC

Absorbance measurements of the above peaks during isothermal polymerizations were used (Equation (1)) to evaluate the relative conversion degree, $\alpha(t)$, for a given reaction time, t:

$$\alpha(t) = \frac{A_t - A_0}{A_\infty - A_0} \quad (1)$$

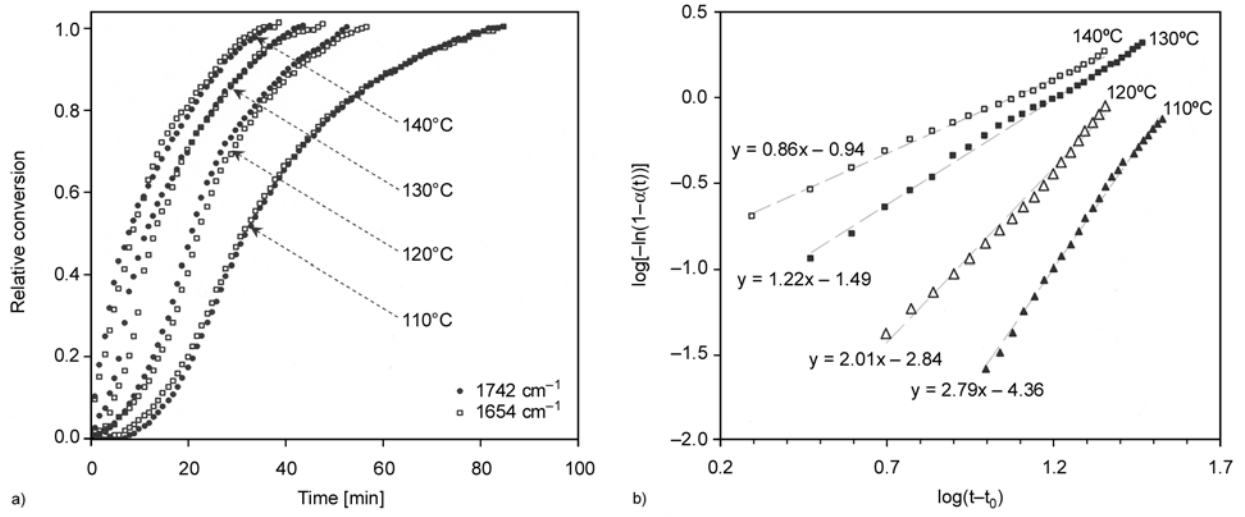

Figure 8. a) Plots of conversion versus reaction time for the isothermal polymerization of the momomer/C20A mixture at 140, 130, 120 and 110ºC. Conversions were determined by absorbance measurements of 1742 and 1654 cm^{-1} FTIR peaks during the reaction process. b) Avrami plots for the polymerizations of the momomer/C20A mixture at the indicated temperatures.

where A_t is the absorbance at time t, and A_∞ and A_0 are, respectively, the final and initial absorbances.

Figure 8a compares the time evolution of the bands at 1742 and 1654 cm^{-1} for polymerizations carried out at different temperatures and in the presence of the C20A clay. For a given clay the evolution of the two bands is quite similar although slight differences were found when polymerization was performed at higher temperatures (i.e. at higher polymerization rates). As will be explained, the addition of clay particles and even their nature had an influence on the polymerization kinetics.

The 1742 cm^{-1} band was selected to perform a polymerization kinetic analysis since it seemed capable of rendering the most accurate data since it is not overlapped with other bands. The Avrami model was considered to examine the polymerization kinetics as it was previously applied for in situ polymerization using C25A clay and other similar systems [21, 27, 30]. This is a rough approximation that makes unnecessary a detailed study of the kinetic model but can provide useful values for comparison purposes. Conversion was then calculated by Equation (2):

$$\alpha(t) = 1 - \exp(-Z(t - t_0)^n) \quad (2)$$

where Z and n are the corresponding Avrami parameters and t_0 the time at which polymerization starts. Plots of $\log[-\ln(1-\alpha(t))]$ versus $\log t$ at different reaction temperatures gave straight lines with slopes corresponding to the Avrami exponent, n, and their intercepts at the origin to $\log Z$ (e.g. Figure 8b for polymerizations carried outwith C20A). Moreover, a kinetic constant (k) with units independent of the Avrami exponent was calculated from $Z^{1/n}$. These parameters are summarized in Table 1 for the two studied systems and the four assayed temperatures, together with the reciprocal of half conversion times ($\tau_{1/2}$). Note that these times could be easily estimated from the conversion curves, and consequently without assuming a specific kinetic model. As expected, the kinetic constant increased with the polymerization temperature and evolved similarly to the reciprocal of the half polymerization time, $1/\tau_{1/2}$, as shown in Figure 9a for the polymerization with C20A. This good agreement is relevant since the Avrami analysis results are corroborated by direct experimental measurements such as half polymerization times.

For comparative purposes, Table 1 also includes previous data on the polymerization of the neat monomer and its mixture with C25A (3 wt%) [27]. It is clear that the overall rate kinetic constant of these two samples increased drastically with increasing temperature whereas a moderate change was observed for polymerizations carried out with C20A and C30B. In this way, the neat monomer had a lower and higher polymerization rate than the C20A and C30B mixtures at 110 and 140ºC, respectively. The influence of temperature on the conversion degree is shown in Figure 9b, where simulated curves from Avrami parameters are plotted for all samples at the intermediate temperatures of 130 and 120ºC. It is worth pointing out that the neat monomer

Table 1. Polymerization kinetic parameters deduced from FTIR absorbance measurements of the 1742 cm^{-1} band

	T [ºC]	$1/\tau_{1/2}$ [min^{-1}]	Z [min^{-n}]	n	k [min^{-1}]
Monomer/C20A mixture	110	0.033	$4.00 \cdot 10^{-5}$	2.79	0.027
Monomer/C20A mixture	120	0.049	$1.43 \cdot 10^{-3}$	2.01	0.038
Monomer/C20A mixture	130	0.087	$3.20 \cdot 10^{-2}$	1.22	0.060
Monomer/C20A mixture	140	0.120	$1.11 \cdot 10^{-1}$	0.86	0.081
Monomer/C30B mixture	110	0.033	$3.89 \cdot 10^{-3}$	1.51	0.025
Monomer/C30B mixture	120	0.050	$3.18 \cdot 10^{-3}$	1.76	0.038
Monomer/C30B mixture	130	0.083	$3.89 \cdot 10^{-3}$	1.98	0.060
Monomer/C30B mixture	140	0.134	$7.19 \cdot 10^{-2}$	1.14	0.098
Monomer/C25A mixture[a]	100	0.010	$1.12 \cdot 10^{-4}$	1.80	0.006
Monomer/C25A mixture[a]	120	0.036	$1.02 \cdot 10^{-2}$	1.31	0.030
Monomer/C25A mixture[a]	130	0.060	$1.51 \cdot 10^{-2}$	1.42	0.052
Monomer/C25A mixture[a]	140	0.142	$1.82 \cdot 10^{-1}$	0.93	0.158
Neat monomer[a]	100	0.011	$5.01 \cdot 10^{-4}$	1.59	0.008
Neat monomer[a]	120	0.042	$7.41 \cdot 10^{-3}$	1.50	0.038
Neat monomer[a]	130	0.128	$7.58 \cdot 10^{-2}$	1.22	0.120
Neat monomer[a]	140	0.200	$2.29 \cdot 10^{-1}$	0.87	0.185

[a]Data from reference [27]

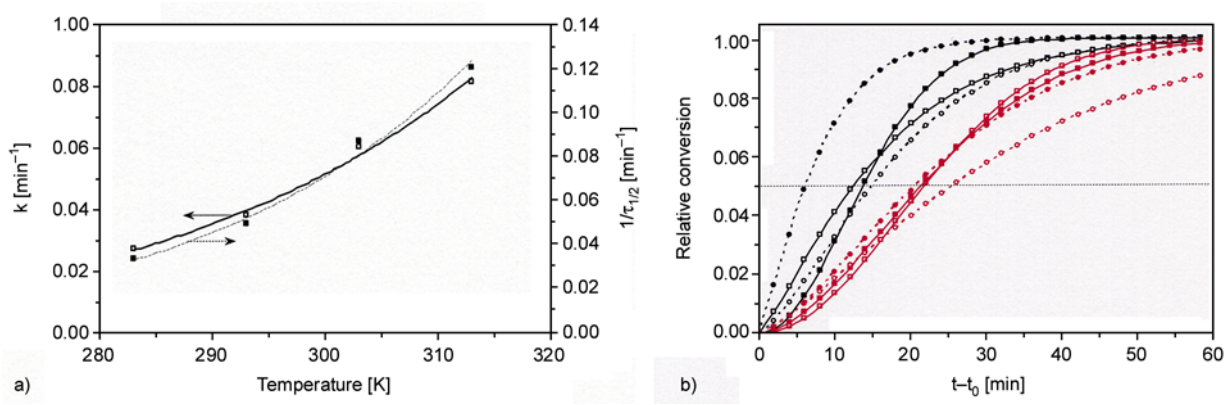

Figure 9. a) Comparison between the kinetic polymerization constant (solid line) and the reciprocal of the half polymerization time (dashed line) determined at different isothermal polymerization temperatures for the momomer/C20A mixture. b) Comparison of the conversion evolution between the neat monomer (•, dashed line), the monomer / C25A mixture (○, dashed line), the monomer / C20A mixture (□, solid line) and the monomer/C30B mixture (■, solid line) at the isothermal polymerization temperature of 130ºC (black lines) and 120ºC (red lines). Data were calculated using Equation (2) and the corresponding Avrami parameters (Table 2 and Reference [27]).

has the fastest conversion at 130ºC but its polymerization rate becomes comparable with that found for the C20A and C30B mixtures when the temperature decreased to 120ºC. Comparison data clearly demonstrated that clay particles influenced the polymerization rate and that the effect of clays that rendered a predominant intercalated structure (C20A and C30B) and C25A clay, which gave rise to an exfoliated structure, was different.

The polymerization activation energies of the mixtures between the neat monomer and C20A and C30B clays were derived by assuming an Arrhenius-type temperature dependence of the kinetic constant (Equation (3)), where E, A and R are the activation energy, the preexponential frequency factor and the universal gas constant, respectively:

$$k = A\exp\left(-\frac{E}{RT}\right) \tag{3}$$

Plots of ln$k$ versus $1/T$ (Figure 10) allowed activation energies of 49.4 and 59.8 kJ/mol to be deduced for in situ polymerization of C20A and C30B mixtures, respectively. These energies were practically identical, but differed significantly from the value previously deduced for the neat monomer (101.0 kJ/mol) and even for its C25A mixture (99.3 kJ/mol), which gave rise to an exfoliated structure [27]. In this way, the activation energy clearly decreased when *in situ* polymerization rendered an intercalated structure. The preexponential frequency factor was also lower for the nanocomposites than for the neat monomer ($3.28\cdot10^{12}$ min^{-1}), indicating

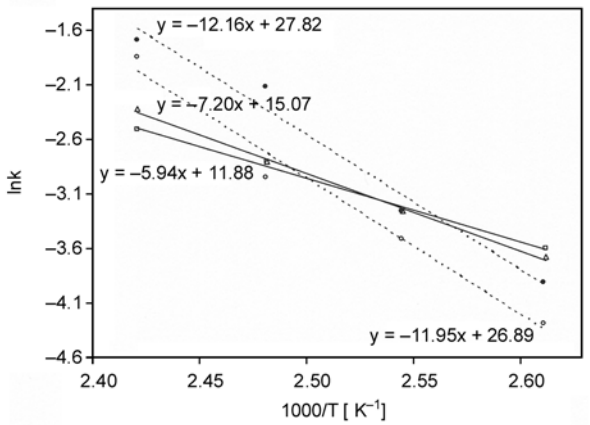

Figure 10. Plots of ln$k$ versus the reciprocal of the polymerization temperature for the neat monomer (•, dashed line) [27] and monomer/C25A (○, dashed line) [27], momomer/C20A (□, solid line) and monomer/C30B (Δ, solid line) mixtures

that chain mobility was restricted by the incorporation of clay particles. Both C20A and C30B clays led to frequency factors of a similar magnitude order ($1.4\cdot10^5$ and $3.4\cdot10^6$ min^{-1}, respectively), but significantly lower than that found for the C25A mixture ($4.77\cdot10^{11}$ min^{-1}).

The polymerization kinetics of monomer/C20A and monomer/C30B mixtures was enhanced at low temperatures due to their low activation energy, which compensated for the decrease caused by their low frequency factor. On the contrary, this factor was determinant at high temperatures, where the corresponding overall rate kinetic constants became minimal.

The changes observed in the activation energy and frequency factor may suggest that nanoconfinement in intercalated structures favored the polycondensation reaction and reduced molecular mobility. It should be emphasized that activation energy did not decrease when nanoconfinement was loosened (i.e. when an exfoliated structure was attained). In this case, the exfoliated layers hindered the chain mobility and reduced again the frequency factor of the condensation reaction.

3.4. Isothermal crystallization kinetics of poly(glc-*alt*-amh) and its C20A and C30B nanocomposites from FTIR analyses

FTIR is highly sensitive to molecular conformation and packing density, hence its usefulness in polymer crystallization studies. Characteristic bands can be correlated to the crystalline and amorphous phases of the bulk and typically remain distinguishable over the course of crystallization. Isothermal studies are preferred to avoid shape and intensity susceptibility of FTIR bands with temperature.

FTIR spectra of poly(glc-*alt*-amh) showed that 3298, 1653, 1419 and 1166 cm^{-1} bandswere characteristic of the crystalline phase. Thus, these bands appeared and their absorbance gradually increased during the isothermal crystallization of samples rapidly cooled to the selected temperature from the melt (amorphous) state.

The continuous evolution of these absorption bands is shown in Figure 11a for the C20A nanocomposite at a representative crystallization temperature of 135ºC. The time evolution of the relative degree of crystallization, $\chi(t)$, was evaluated similarly to that of the degree of conversion (i.e. changing $\alpha(t)$ by $\chi(t)$ in Equations (1) and (2)). Figure 11b shows that the four selected bands exhibit a similar behavior for a given crystallization temperature. Thus, in all cases the maximum crystallinity change was detected at a similar time. However, absorbance measurements seemed more accurate when the signal corresponding to the Amide A (3298 cm^{-1}) was considered. The establishment of stronger hydrogen bond interactions in the crystalline structure gave rise to a well defined band which, in addition, was not overlapped by other peaks.

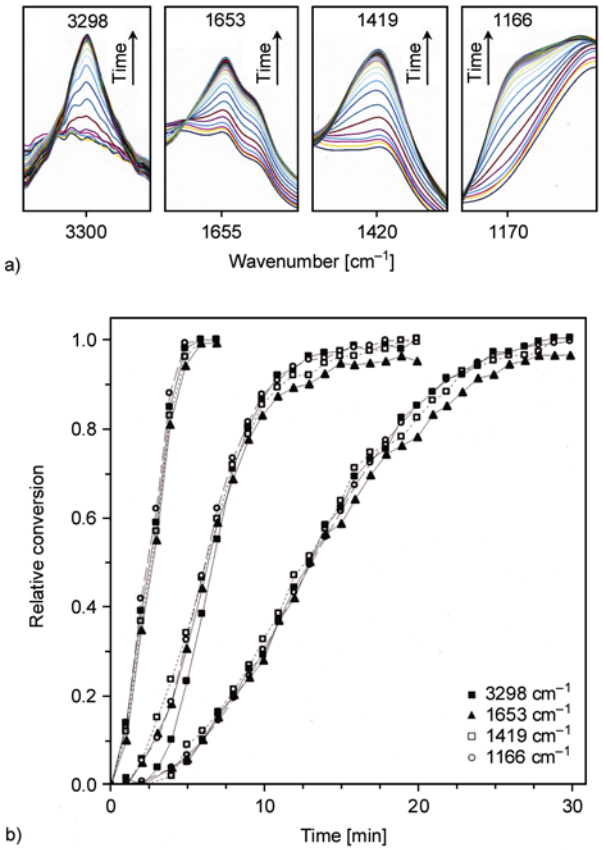

Figure 11. a) Changes in the infrared absorption bands at 3298, 1653, 1419 and 1166 cm^{-1} of the poly(glc-*alt*-amh)/C20A nanocomposite during isothermal crystallization at 135ºC. b) Time evolution of the relative crystallinity determined from absorbance measurements of the 3298 (■), 1653 (▲), 1419 (□) and 1166 (○) cm^{-1} FTIR bands of the poly(glc-*alt*-amh)/C30B nanocomposite during isothermal crystallization at 135ºC.

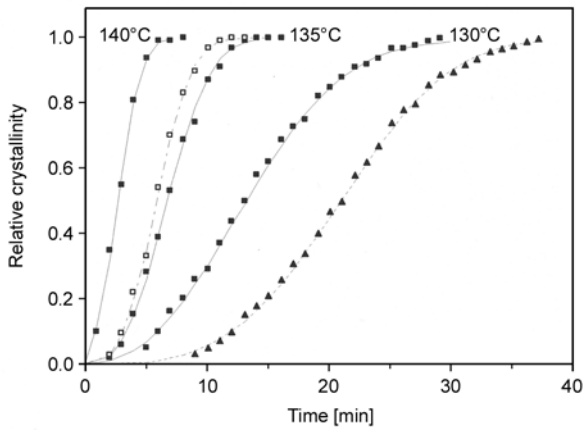

Figure 12. Time evolution of the relative crystallinity determined from absorbance measurements of the 3298 cm^{-1} FTIR band of the poly(glc-*alt*-amh)/C30B nanocomposite (■) during isothermal crystallization at 140, 135 and 130ºC. For comparative purposes, the evolution for the poly (glc-*alt*-amh)/C20A nanocomposite (□, dashed line) and the neat polymer at 135ºC is also shown (▲, dashed line).

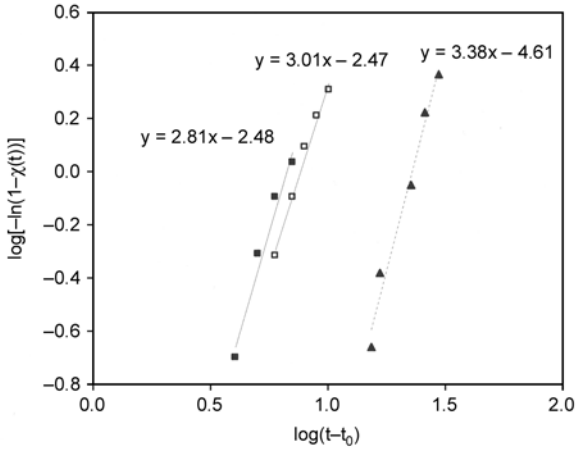

Figure 13. Avrami plot considering FTIR data (3298 cm^{-1} band) for isothermal crystallization of the neat poly(ester amide) (▲) and its C20A (□) and C30B (■) nanocomposites at 135ºC

Table 2. Crystallization kinetic parameters at 135ºC deduced from FTIR absorbance measures of the 3298 cm^{-1} band

Sample	$1/\tau_{1/2}$ [min^{-1}]	Z [min^{-n}]	n	k [min^{-1}]
Neat polymer	0.048	$2.40 \cdot 10^{-5}$	3.38	0.043
Nanocomposite with C20A	0.174	$3.40 \cdot 10^{-3}$	3.01	0.153
Nanocomposite with C30B	0.149	$3.28 \cdot 10^{-3}$	2.81	0.131

Figure 12 compares the evolution of the degree of crystallinity at different temperatures for the C30B nanocomposite, as well as the evolution of the neat polymer and its C30B and C20A nanocomposites at a representative temperature (135ºC). Note that the crystallization rate is clearly slower for the neat polymer.

Avrami plots (as shown in Figure 13 for the C30B nanocomposite) allowed determining an exponent close to 3, which is the theoretical value for heterogeneous nucleation and three-dimensional spherulitic growth. In the same way, the kinetic constant, *k*, was calculated from the deduced *Z* and n values. Table 2 compares the kinetic parameters of the three studied samples at a common temperature (135ºC). The Avrami exponents of the three samples were close enough to deduce that nucleation type and crystal dimensionality remained unaffected by the addition of clay particles. On the contrary, the incorporation of silicate layers with an intercalated structure clearly increased the overall rate kinetic constant. This effect was more pronounced with C20A clay, as shown in Table 2. Note that the same trend was observed when the reciprocal of the half crystallization time, $1/\tau_{1/2}$, was considered.This good correlation with a direct experimental measurement may validate the Avrami analysis of the crystallization process.

3.5. Optical microscopy studies on the isothermal crystallization of poly(glc-*alt*-amh) and its C20A and C30B nanocomposites

The spherulites of the neat poly(ester amide) and its C20A and C30B nanocomposites had negative birefringence, as demonstrated by the position of the blue and yellow arms in the optical micrographs in the inset of Figure 14. Different spherulitic morphologies were observed depending on the crystallization temperature and the addition of clay particles. Thus, the neat polymer gave rise to speckled, ringed and fibrilar spherulites at temperatures close to 125, 130 and 140ºC, respectively. The addition of a clay that rendered an exfoliated structure (i.e. C25A) favored the development of fibrilar textures [27] and hindered lamellar twisting, whereas the incorporation of clays associated with a final intercalated structure (i.e. C20A and C30B) led to the formation of speckled textures, as shown in Figure 14.

Nucleation density was higher for the nanocomposites derived from C20A and C30B (i.e. those with an intercalated structure), as deduced from the number of spherulites measured in the field of view of the optical microscope. At all temperatures, the nucleation density decreased in the order C20A > C30B > neat polymer, as shown in Figure 15a.

The change in the primary nucleation was responsible for the difference in overall crystallization rates between the neat polymer and C20A and C30B nanocomposites found by FTIR. The incorporation of a clay that favors an intercalated structure increased the nucleation density. In fact, the experimental data indicate that the effect was more pronounced with the addition of C20A clay. It should be pointed out that the crystallization of the C25A nanocomposite was previously studied and that a lower nucleation density was derived for this sample with an exfoliated silicate structure [27]. Furthermore, the overall crystallization rate decreased when this clay was incorporated.

The spherulic radial growth rates (*G*) of the neat sample and its C20A and C30B nanocomposites were determined with the evolution of the spherulite

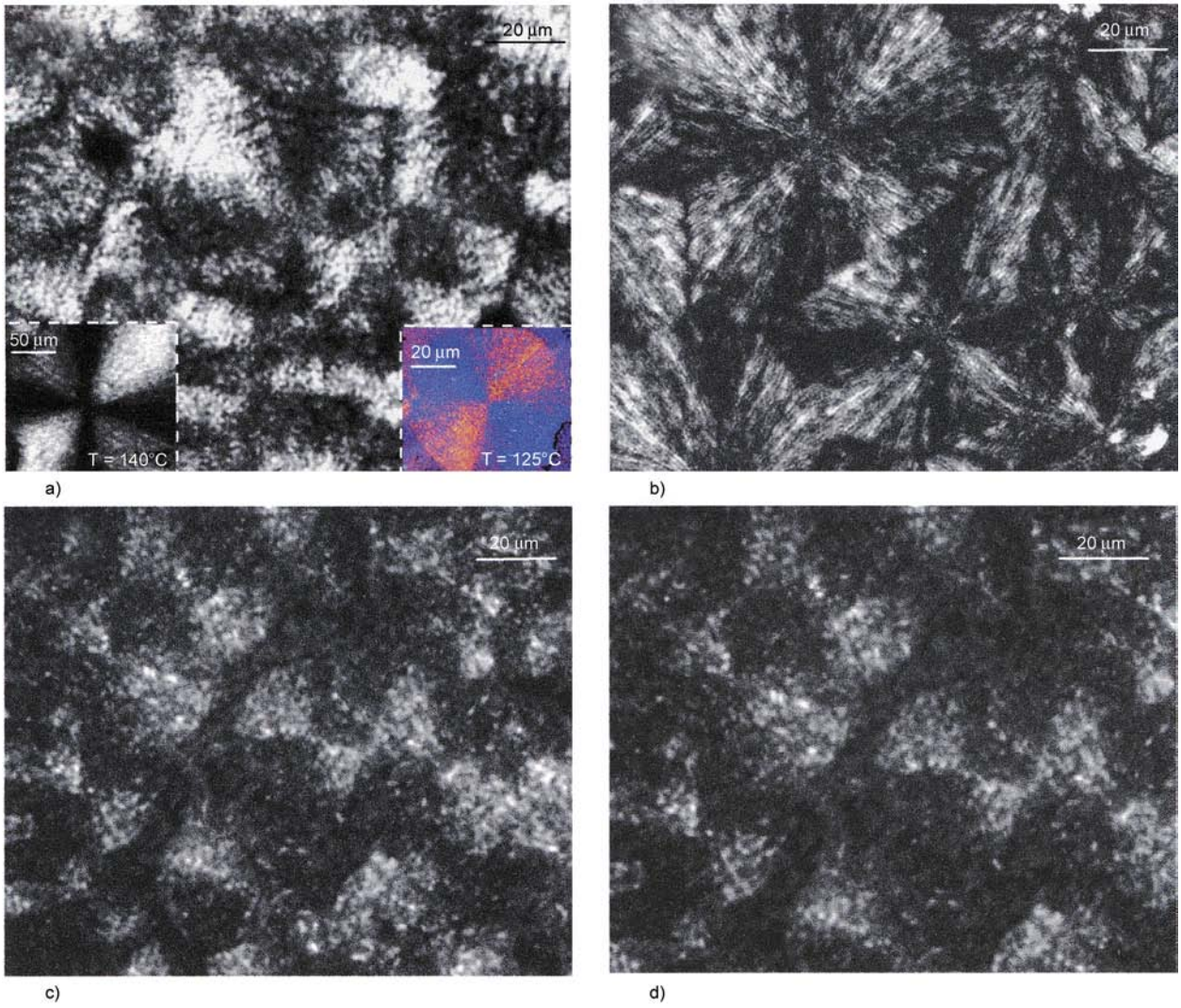

Figure 14. Polarized optical micrographs showing the isothermal hot crystallizations of the neat poly(ester amide) (a) and its C25A (b), C20A (c) and C30B (d) nanocomposites at 130ºC. Insets show micrographs of speckled and fibrilar spherulites attained at 125 and 140ºC, respectively, with the neat polymer sample.

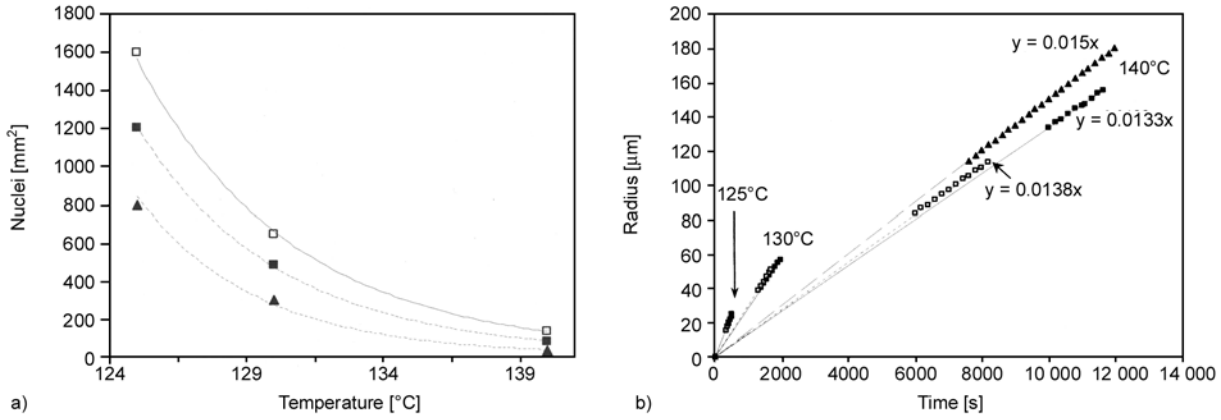

Figure 15. a) Variation in nucleation density with isothermal crystallization temperature for the neat polymer (▲) and its C20A (□) and C30B (■) nanocomposites. b) Plot of the radius of spherulites of the neat polymer (▲) and its C20A (□) and C30B nanocomposites (■) versus crystallization time for isothermal crystallizations at 125, 130 and 140ºC.

radius versus time. It is worth pointing out that a linear increase in the spherulite radius was always found, suggesting that clay particles were not segregated during spherulite growth. Data for crystallization temperatures of 125, 130 and 140ºC (Figure 15b) showed that the growth rate of the two nanocomposites was similar although a slightly lower value was found for C30B. Differences were more significant at a high crystallization temperature (e.g. 140ºC), with measurements clearly indicating that the incorporation of clay particles reduced the spherulitic growth rate (i.e. 0.015 μm/s versus 0.014–0.013 μm/s). Note that the overall crystallization process did not decelerate with the addition of clay particles since the accelerative effect caused by the increase in the primary nucleation density was more significant than the decrease in the crystal growth rate.

In summary, silicate particles acted as effective nucleating agents at low degrees of compatibility, a result that contrasts with the observations on the exfoliated structure (i.e. when the organo-modified clay becomes highly miscible with the polymer matrix) which indicated a decrease on the primary nucleation. In all cases, the addition of clay particles slightly reduced the radial growth rate since both secondary nucleation and molecular transport may be influenced by the presence of nanoparticles.

4. Conclusions

Nanocomposites constituted by a poly(ester amide) matrix and C20A or C30B organo-modified clays were obtained by *in situ* polymerization of sodium chloroacetylaminohexanoate. They showed an intercalated silicate structure, as determined by X-ray diffraction and transmission electron microscopy. The polymerization kinetics under both non-isothermal and isothermal conditions was quite similar after the incorporation of the two clays. However, great differences were found with the polymerization of the neat monomer. The temperature dependence of the polymerization kinetic constant allowed inferring the activation energies and preexponential frequency factors, which were lower when polymerization was performed in the presence of clay particles. Nanoconfinement in the intercalated silicate galleries may favor the occurrence of polycondensation reactions and reduce the corresponding activation energy. This confinement should logically result in decreased chain mobility and consequently lower frequency factor.

Optical microscopy and FTIR studies revealed that the crystallization rate of the nanocomposites increased due to the nucleation effect of clay particles. On the contrary, spherulitic crystal growth was slightly hindered when particles were added. Spherulites always showed negative birefringence but their texture was influenced by the incorporation of clay and obviously by the crystallization temperature.

Acknowledgements

This research has been supported by grants from MICYT/FEDER and AGAUR (MAT2009-11503, 2009SGR-1208). We want to express our gratitude to Drs. François Fauth and Ana Labrador of the CRG BM16 beamline staff of CELLS (Consortium for the Exploitation of the Synchrotron Light Laboratory).

References

[1] Pavlidou S., Papaspyrides C. D.: A review on polymer–layered silicate nanocomposites. Progress in Polymer Science, **12**, 1119–1198 (2008).
DOI: 10.1016/j.progpolymsci.2008.07.008

[2] Ray S. S., Bousmina M.: Biodegradable polymers and their layered silicate nanocomposites: In greening the 21st century materials world. Progress in Materials Science, **50**, 962–1079 (2005).
DOI: 10.1016/j.pmatsci.2005.05.002

[3] Ray S. S., Okamoto M.: Polymer/layered silicate nanocomposites: A review from preparation to processing. Progress in Polymer Science, **28**, 1539–1641 (2003).
DOI: 10.1016/j.progpolymsci.2003.08.002

[4] Carrado K. A.: Synthetic organo- and polymer–clays: Preparation, characterization and materials applications. Applied Clay Science, **17**, 1–23 (2000).
DOI: 10.1016/S0169-1317(00)00005-3

[5] Alexandre M., Dubois P.: Polymer-layered silicate nanocomposites: Preparation, properties and uses of a new class of materials. Materials Science and Engineering R: Reports, **28**, 1–63 (2000).
DOI: 10.1016/S0927-796X(00)00012-7

[6] Usuki A., Kojima Y., Kawasumi M., Okada A., Fukushima Y., Kurauchi T., Kamigato O.: Synthesis of nylon 6-clay hybrid. Journal of Materials Research, **8**, 1179–1184 (1993).
DOI: 10.1557/JMR.1993.1179

[7] Kawasumi M.: The discovery of polymer-clay hybrids. Journal Polymer Science Part A: Polymer Chemistry, **42**, 819–824 (2004).
DOI: 10.1002/pola.10961

[8] Ishida H., Campbell S., Blackwell J.: General approach to nanocomposite preparation. Chemistry of Materials, **12**, 1260–1267 (2000).
DOI: 10.1021/cm990479y

[9] Akelah A., Salahuddin N., Hiltner A., Baer E., Moet A.: Morphological hierarchy of butadieneacrylonitrile/montmorillonite nanocomposite. Nanostructured Materials, **4**, 965–978 (1994).
DOI: 10.1016/0965-9773(94)90103-1

[10] Kennedy M. A., Brown G. R., St-Pierre L. E.: Crystallization of isotactic (D,L) poly(propylene oxide) in the presence of fine-particle silica. I: Radial growth rates of spherulites. Polymer Engineering and Science, **30**, 769–775 (1990).
DOI: 10.1002/pen.760301304

[11] Nitta K-H., Asuka K., Liu B. P., Terano M.: The effect of the addition of silica particles on linear spherulite growth rate of isotactic polypropylene and its explanation by lamellar cluster model. Polymer, **47**, 6457–6463 (2006).
DOI: 10.1016/j.polymer.2006.06.054

[12] Somwangthanaroj A., Lee E. C., Solomon M. J.: Early stage quiescent and flow-induced crystallization of intercalated polypropylene nanocomposites by time-resolved light scattering. Macromolecules, **36**, 2333–2342 (2003).
DOI: 10.1021/ma021454e

[13] Nowacki R., Monasse B., Piorkowska E., Galeski A., Haudin J. M.: Spherulite nucleation in isotactic polypropylene based nanocomposites with montmorillonite under shear. Polymer, **45**, 4877–4892 (2004).
DOI: 10.1016/j.polymer.2004.04.058

[14] Burke M., Young R. J., Stanford J. L.: The relationship between structure and properties in titanium dioxide filled polypropylene. Polymer Bulletin, **30**, 361–368 (1993).
DOI: 10.1007/BF00343073

[15] Stapert H. R., Bouwens A. W., Dijkstra P. J., Feijen J.: Environmentally degradable aliphatic poly(ester-amide)s based on short, symmetrical and uniform bisamide-diol blocks, 1. Synthesis and interchange reactions. Macromolecular Chemistry and Physics, **200**, 1921–1929 (1999).
DOI: 10.1002/(SICI)1521-3935(19990801)200:8<1921::AID-MACP1921>3.0.CO;2-R

[16] Guo K., Chu C. C.: Synthesis, characterization, and biodegradation of copolymers of unsaturated and saturated poly(ester amide)s. Jounal of Polymer Science Part A: Polymer Chemistry, **45**, 1595–1606 (2007).
DOI: 10.1002/pola.21926

[17] Paredes N., Rodríguez-Galán A., Puiggali J.: Synthesis and characterization of a family of biodegradable poly (ester amide)s derived from glycine. Journal of Polymer Science Part A: Polymer Chemistry, **36**, 1271–1282 (1998).
DOI: 10.1002/(SICI)1099-0518(199806)36:8<1271::AID-POLA10>3.3.CO;2-U

[18] Guo K., Chu C. C.: Synthesis, characterization, and biodegradation of novel poly(ether ester amide)s based on L-phenylalanine and oligoethylene glycol. Biomacromolecules, **8**, 2851–2861 (2007).
DOI: 10.1021/bm070158c

[19] Rodríguez-Galán A., Pelfort M., Aceituno J. E., Puiggalí J.: Comparative studies on the degradability of poly(ester amide)s derived from L- and L,D-alanine. Journal of Applied Polymer Science, **74**, 2312–2320 (1999).
DOI: 10.1002/(SICI)1097-4628(19991128)74:9<2312::AID-APP21>3.0.CO;2-0

[20] Vera M., Rodríguez-Galán A., Puiggali J.: New method of synthesis of poly(ester amide)s derived from the incorporation of glycolic acid residues into aliphatic polyamides. Macromolecular Rapid Communications, **25**, 812–817 (2004).
DOI: 10.1002/marc.200300273

[21] Vera M., Franco L., Puiggalí J.: Synthesis and characterization of poly(glycolic acid-*alt*-6-aminohexanoic acid) and poly(glycolic acid-*alt*-11-aminoundecanoic acid). Macromolecular Chemistry and Physics, **205**, 1782–1792 (2004).
DOI: 10.1002/macp.200400191

[22] Wang D., Zhu J., Yao Q., Wilkie C. A.: A comparison of various methods for the preparation of polystyrene and poly(methyl methacrylate) clay nanocomposites. Chemistry of Materials, **14**, 3837–3843 (2002).
DOI: 10.1021/cm011656+

[23] LeBaron P. C., Wang Z., Pinnavaia T. J.: Polymer-layered silicate nanocomposites: An overview. Applied Clay Science, **12**, 11–29 (1999).
DOI: 10.1016/S0169-1317(99)00017-4

[24] Akelah A., Moet A.: Polymer-clay nanocomposites: Free-radical grafting of polystyrene on to organophilic montmorillonite interlayers. Journal of Materials Science, **31**, 3589–3596 (1996).
DOI: 10.1007/BF00360767

[25] Messersmith P. B., Giannelis E. P.: Polymer-layered silicate nanocomposites: In situ intercalative polymerization of ε-caprolactone in layered silicates. Chemistry of Materials, **5**, 1064–1066 (1993).
DOI: 10.1021/cm00032a005

[26] Fukushima Y., Okada A., Kawasumi M., Kurauchi T., Kamigaito O.: Swelling behavior of montmorillonite by poly-6-amide. Clay Minerals, **23**, 27–34 (1988).

[27] Morales L., Franco L., Casas M. T., Puiggalí J.: Poly(ester amide)/clay nanocomposites prepared by *in situ* polymerization of the sodium salt of *N*-chloroacetyl-6-aminohexanoic acid. Journal Polymer Science Part A: Polymer Chemistry, **47**, 3616–3629 (2009). DOI: 10.1002/pola.23430

[28] Morales-Gámez L., Franco L., Casas M. T., Puiggalí J.: Crystallization studies on a clay nanocomposite prepared from a degradable poly(ester amide) constituted by glycolic acid and 6-aminohexanoic acid. Polymer Engineering and Science, in press (2011). DOI: 10.1002/pen.21936

[29] Botines E., Casas M. T., Puiggalí J.: Alternating poly(ester amide)s of glycolic acid and ω-amino acids: Crystalline morphology and main crystallographic data. Journal of Polymer Science Part B: Polymer Physics, **45**, 815–825 (2007). DOI: 10.1002/polb.21077

[30] Rodríguez-Galán A., Vera M., Jiménez K., Franco L., Puiggalí J.: Synthesis of poly(ester amide)s derived from glycolic acid and the amino acids: β-alanine or 4-aminobutyric acid. Macromolecular Chemistry and Physics, **204**, 2078–2089 (2003). DOI: 10.1002/macp.200350064

eXPRESS Polymer Letters Vol.5, No.8 (2011) 732–741
Available online at www.expresspolymlett.com
DOI: 10.3144/expresspolymlett.2011.71

A modified coaxial electrospinning for preparing fibers from a high concentration polymer solution

D. G. Yu [1], C. Branford-White[2], K. White[2], N. P. Chatterton[2], L. M. Zhu[1], L. Y. Huang[1], B. Wang[1]*

[1]College of Chemistry, Chemical Engineering and Biotechnology, Donghua University, Shanghai 201620, China
[2]Institute for Health Research and Policy, London Metropolitan University, London, N7 8DB, UK

Received 10 January 2011; accepted in revised form 28 February 2011

Abstract. A new process technology modified from conventional coaxial electrospinning process has been developed to prepare polymer fibers from a high concentration solution. This process involves a pure solvent concentrically surrounding polymer fluid in the spinneret. The concentric spinneret was constructed simply by inserting a metal needle through a high elastic silica gel tube. Two syringe pumps were used to drive the core polymer solution and the sheath solvent. Using polyvinylpyrrolidone (PVP) as the polymer model, which normally has an electrospinnable concentration of 10% w/v in ethanol, it was possible to electrospin 35% w/v of PVP in the same solvent, when pure N, N-dimethylacetamide (DMAc) was used as sheath fluid. The resultant fibers have a smooth surface morphology and good structural uniformity. The diameter of the fibers was 2.0±0.25 μm when the DMAc-to-polymer-solution flow rate ratio was set as 0.1. The process technology reported here opens a new window to tune the polymer fibers obtained by the electrospinning, and is useful for improving productivity of the electrospinning process.

Keywords: *processing technologies, coaxial electrospinning, polymer fibers, productivity*

1. Introduction

Polymer fibers provide a platform for a number of diverse applications, including drug encapsulation, biosensing, filtration, fuel cells, composites, and nanoelectronics [1–3]. Among the advanced processing techniques that have been used to produce fibers from natural and synthetic polymers, the electrospinning process provides the simplest approach to prepare nano- or microscale diameter fibers that are exceptionally long, uniform in shape, and diverse in composition [4–6]. By utilizing electrostatic interactions and elongation of the viscoelastic jet system, electrospinning can prepare ultrafine fibers from a polymer solution or molten sample adopting a simple one-step process. Numerous polymers have been reported to be electrospun into nanofibers for functional applications in the literature [1–6].

However, although the one-step 'top-down' electrospinning process is simple, there is a wide range of parameters that influence the electrospinnability of polymer solutions and properties of the generated fibers. These parameters include solution properties (concentration, viscosity, elasticity, conductivity, and surface tension); systematic variables (flow rate, electric potential at the capillary tip, and the distance between the tip and the fiber collector); and ambient conditions (temperature, humidity, and air velocity) [7, 8]. Among these parameters, concentration is regarded as the most significant parameter for developing smooth electrospinning and high quality fibers [9, 10].

Fiber formation is primarily governed by the viscosity of the polymer solution and strength of the applied electric field. The viscosity of the polymer solution depends on the concentration and structure

*Corresponding author, e-mail: ydg017@dhu.edu.cn

of the polymer. Often there is an upper and lower limit for polymer concentration during electrospinning [11]. It is well known that the prerequisite for fiber formation is the presence of sufficient chain-entanglement density in the working solution as this prevents the capillary breakup and provides deformable networks. When the polymer concentration is lower than the minimum, there is insufficient chain-entanglement for filament forming and electrospinning will degenerate into electrospraying. A number of studies have demonstrated this phenomenon [12, 13]. However, little research has been undertaken to determine the upper concentration limit for smooth electrospinning. Often it is not possible to electrospin at high polymer concentrations due to viscosity factors that influence solvent levels and so affect the formation of a stable jet, thereby clogging the flow of components required for continuous electrospinning. If polymer solution with a high concentration can be electrospun into ultra-fine fibers, it would inevitably improve the capability of electrospinning and broaden the applications of polymer fibers. Examples include: extending the range of electrospinnable concentrations of polymer solutions; improving the productivity of the electrospinning process; allowing preparation of ultra-fine fibers with diameters between several microns to 50 μm for biomedical applications such as improving cell penetration effects of fiber-based scaffolds; facilitating encapsulation of functional materials in a core-sheath manner.

On the other hand, although significant progress has been made in the electrospinning process over the past few years and the resultant nanostructures have been exploited in a wide range of applications, this simple one-step top-down nanofiber fabricating process still needs to be optimized so as to broaden its filament-forming capability over a wide range of materials and with higher nanofiber production rates [14, 15].

Recently there is a growing need for fiber materials that are flexible and provide opportunities for the development of new electrospinning techniques that include specialized nozzle systems, auxiliary apparatus, guiding electrodes and functionalized target electrodes [16, 17]. These electrospinning processes include coaxial electrospinning, side-by-side electrospinning, elevated temperature electrospinning, vibrational electrospinning, magneto-electrospinning, siroelectrospinning and bubble electrospinning, and electrospinning with an air-blowing system, electrospinning in raised humidity conditions, and electrospinning in vacuum conditions for increasing the controllablity of the filament-forming process and also for improving the quality of the resultant fibers [18–24]. Nonetheless, seldom effort has been spent on overcoming and understanding the limitations of high polymer concentration for smooth electrospinning. Although there are several recent studies aimed at preventing clogging during the conventional electrospinning process [25, 26], they did not investigate the possibility of electrospinning polymer solutions with high concentrations that normally is impossible for the conventional electrospinning process.

In the present study, a new modified coaxial electrospinning process was developed to extend the upper concentration limit of electrospinnable solutions of polyvinylpyrrolidone (PVP), a hydrophilic filament-forming polymer used in our laboratory previously [27–29], that has a wide variety of applications in medicine, food, pharmacy, cosmetics and industrial production [30]. The new process involves synchronously pumping pure solvent concentrically around the high concentration polymer solutions to facilitate the electrospinning process.

2. Materials and methods

2.1. Materials

PVP K60 (M_w = 360 000) was purchased from Shanghai Yunhong Pharmaceutical Aids and Technology Co., Ltd. (Shanghai, China). Analytic grade N, N-dimethylacetamide (DMAc) and anhydrous ethanol was provided by the Sinopharm Chemical Reagent Co., Ltd. Water was highly purified water.

2.2. Electrospinning process

Spinning solutions of PVP of concentrations 10, 30 and 35% w/v were prepared in anhydrous ethanol, respectively. The solutions at concentration of 10 and 30% were used in conventional electrospinning.

A schematic diagram and photographs of the modified coaxial electrospinning apparatus are shown in Figure 1. Two syringe pumps (KDS100 and KDS200, Cole-Parmer, Illinois, USA) were used for driving the high concentration PVP solutions and the surrounding DMAc solvent synchronously.

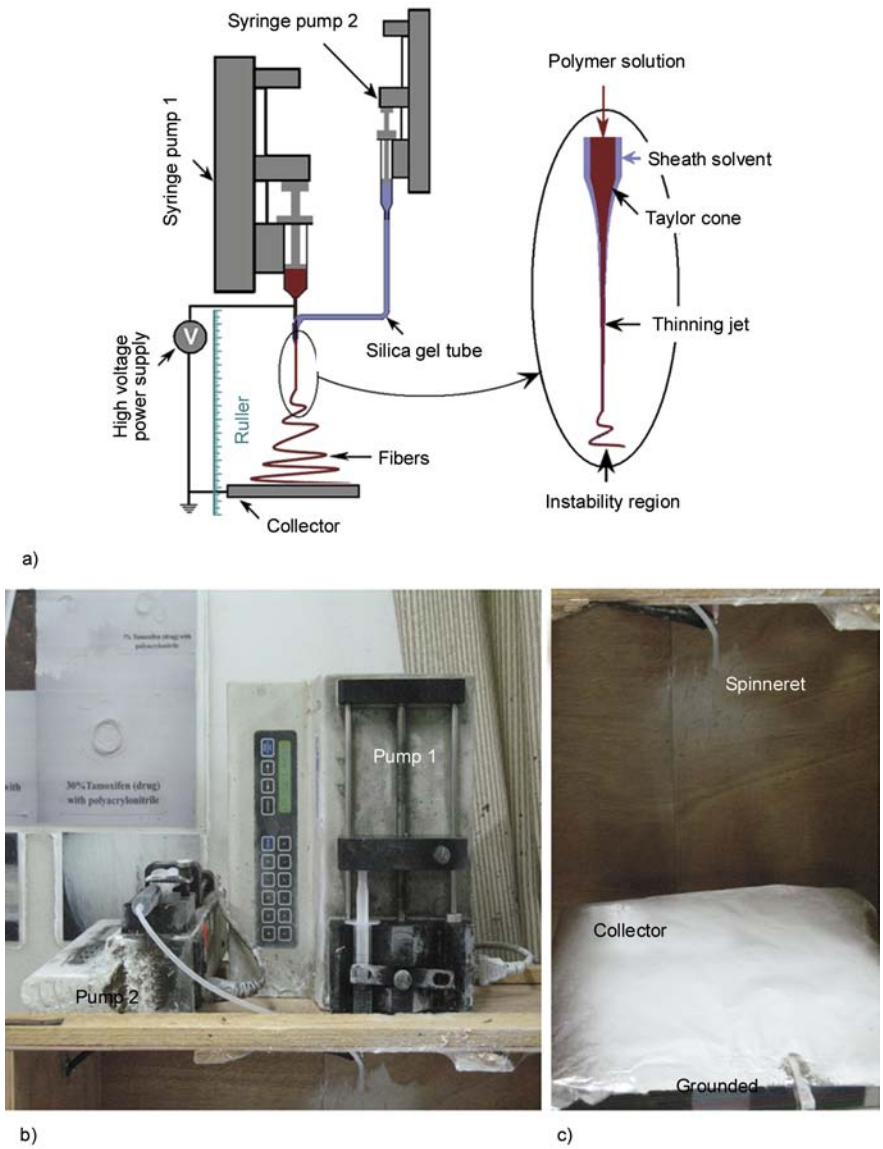

Figure 1. An apparatus for modified coaxial electrospinning. a) schematic diagram, b) pump, c) spinneret and collector.

A high-voltage power supply (ZGF 60 kV/2 mA, Shanghai Sute Corp., China) was used at a fixed voltage of 10 kV, and the fibers produced were collected on aluminium foil at a pre-determined distance. The core and sheath flow rate were selected as 1.0 and 0.1 ml/h respectively. All electrospinning was carried out under ambient conditions (24±2°C with relative humidity 54±4%).

Electrospinning was recorded using a digital video recorder (maximum magnification16×, PowerShot A640, Canon, Tokyo, Japan). The fibers were dried for over 24 h at 40°C under vacuum (320 Pa) in a DZF-6050 Electric Vacuum Drying Oven (Shanghai Laboratory Instrument Work Co. Ltd., Shanghai, China) to facilitate the removal of residual organic solvent and moisture.

2.3. Characterization

Surface morphology of the electrospun fibers was observed using an XP-700 polarized optical microscope (PM, Shanghai Changfang Optical Instrument Co., Ltd) or a JSM-5600LV scanning electron microscope (SEM, Japan Electron Optics Laboratory Co. Ltd., Tokyo, Japan). Prior to SEM examination, samples were gold sputter-coated under argon to render them electrically conductive. Pictures were then taken at an excitation voltage of 10 kV. The average fiber diameter was determined by measuring diameters of fibers at over 100 points from SEM images or polarized microscopic images using Image J software (National Institutes of Health, USA).

3. Results and discussion

3.1. Conventional electrospinning of 10 and 30% PVP solutions

When PVP solutions with a concentration of 30% flow from the syringe to the needle tip in the absence of an electric field, a semispherical droplet forms at the needle tip due to the effect of the surface tension of the solution (Figure 2a). The droplet size becomes larger and longer with a continuous supply of the polymer solution, and finally forms a column, which hangs on the tip until the gravitational force overcomes the surface tension, at which

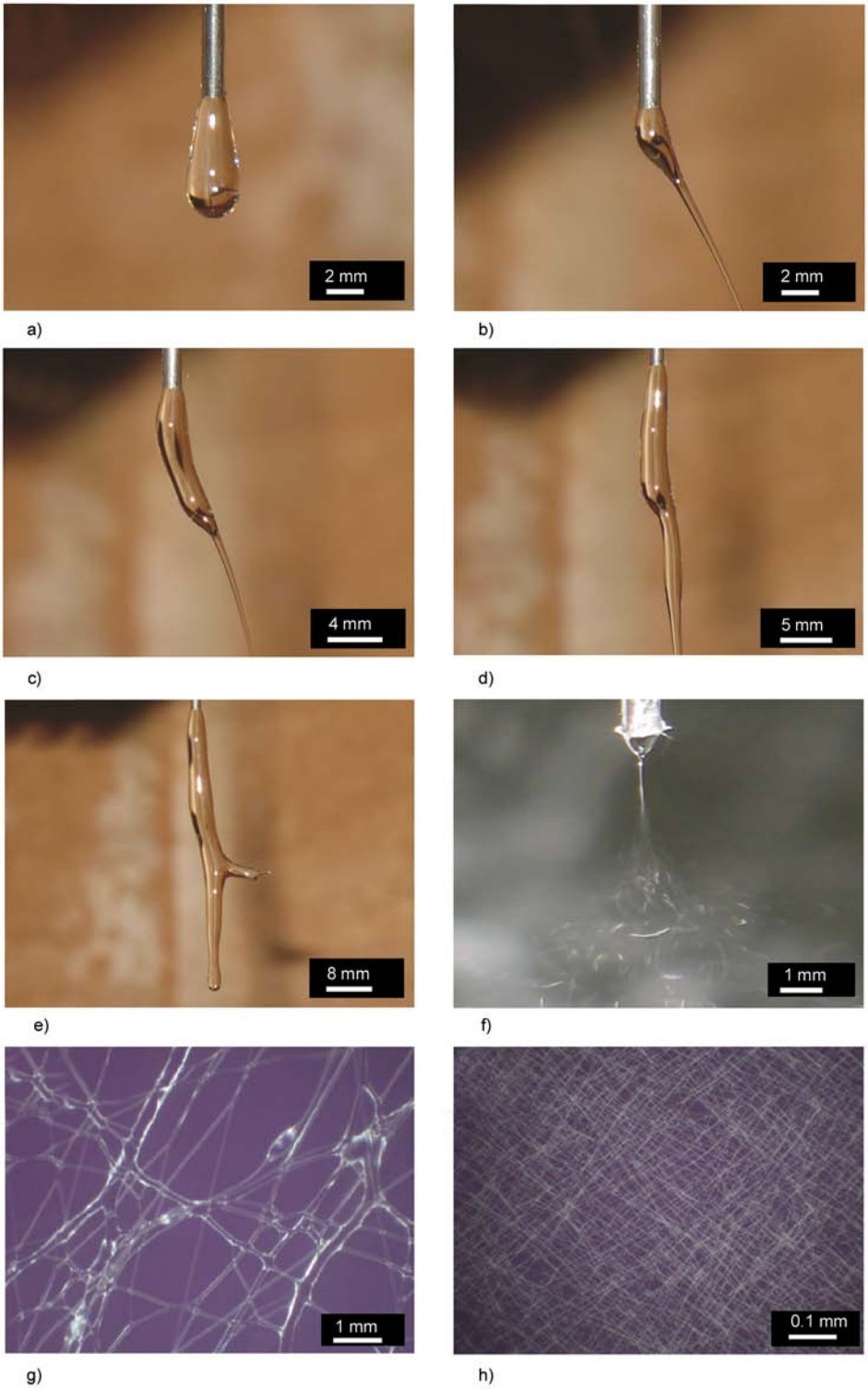

Figure 2. Images of conventional electrospinning process and the resultant fibers. a) to e) 30% (w/v) PVP solutions being electrospun in an open atmosphere, f) 10% (w/v) PVP solution being electrospun in an open atmosphere, g) and h) polarized microscopic images of the resultant fibers from 30 and 10% PVP solutions, respectively.

point the column then drips from the needle tip and new droplet and column form. During the formation and growth of the column, solvent evaporation naturally occurs due to the difference between the concentration of the solvent in the solution and that in the atmosphere. When the polymer solution was subjected to an electrically charge of 10 kV, the polymer droplet shape began to change from a semi-spherical to a conical shape, and a jet was formed because the electric force overcame the shape-maintaining forces from surface tension (Figure 2b).

As time continued, a column formed and grew rapidly (Figure 2c and d). The high viscosity of PVP solutions at high concentrations and the high-volatility of the solvent ethanol promoted the quick formation of an even more viscous gel-like skin on the droplet surface. The applied electrical force was not adequate to overcome the viscous drag force at the droplet-air interface; meanwhile the core was still fluid and driven by solution input from the pump, which in turn led to the formation of a column and a gradual enlarging of the gel skin and the volume of column. The fast evaporation of ethanol was due to Joule heating (resulting from volumetric heating when an electric field is applied across a conducting medium such as a polymer solution [31]) and the difference in concentration of ethanol between the polymer solution and the open atmosphere.

As the column further grew, the Taylor cone moved forward along the column ending up far from the tip of spinneret. This gave the solvent a long time to evaporate. Thus it was inevitable that the polymer solution could no longer be ejected from the Taylor cone, and hence the electrospinning jet was interrupted (Figure 2e). After gravitational and electronic forces cleaned up the column, elctrospinning could continue but only for a short time, after which it stopped again. Electrospinning of the high concentration PVP solution could not be carried out smoothly and continuously.

Shown in Figure 2g are electrospun fibers collected at a distance of 25 cm from the top of spinning head. The fibers obviously had very poor quality (a wide ranging diameter distribution, and all fibers bonded together) resulting from the instability of electrospinning of high PVP concentration solutions. Such clogging is frequently observed when high-volatility solvents are used to prepare polymer solutions [32, 33]. Clogging of 30% PVP solutions was accelerated owing to the high viscosity of the solution, and in contrast 10% PVP solutions could be electrospun smoothly and continuously (Figure 2f), and the resultant nanofibers were homogeneous (Figure 2h).

3.2. Coaxial electrospinning with sheath solvent

To attempt electrospinning of concentrated solutions of PVP, we used a coaxial arrangement in which the PVP solution was spun through a stainless steel capillary metal-hub needle (with an inner and outer diameter of 1 and 1.32 mm respectively) inserted into a silica gel tube (with an outer and inner diameter of 4 and 2 mm respectively) (Figure 3a).

Sheath solvent, DMAc, was coaxially spun around the PVP solution. Using this arrangement it was possible to electrospin fibers from a concentrated PVP solution of 35% (w/v), which would not be possible when using a conventional electrospinning apparatus. In the absence of sheath solvent a droplet formed immediately when the PVP solution was squeezed out of the needle (Figure 3b), which was due to the evaporation of ethanol in the atmosphere, and high viscoelasticity and surface tensions of the solution.

When sheath solvent was supplied to surround the high concentration PVP solution, a half ellipse droplet was formed (Figure 3c). When a voltage of 10 kV was supplied, the droplet shape changed from semi-spherical to conical and a jet was formed stably under the electrical force (Figure 3d).

By using a DMAc flow rate that was only 10% (w/v) of the PVP solution, the electrospinning of the high concentration PVP solution was continuous and smooth. The surrounding DMAc played the following roles during the electrospinning process: (1) lubricating the spinning head to avoid the polymer clinging to it; (2) slowing the rate of solvent evaporation and hence retarding the formation of a highly viscous surface on the Taylor cone and the thinning jet; (3) keeping the jet at a fluid state and thus under an electrical drawing force for a longer time to make the fiber diameters thinner.

It is well known that electrospinning involves the use of an electrical charge to draw micro or nano

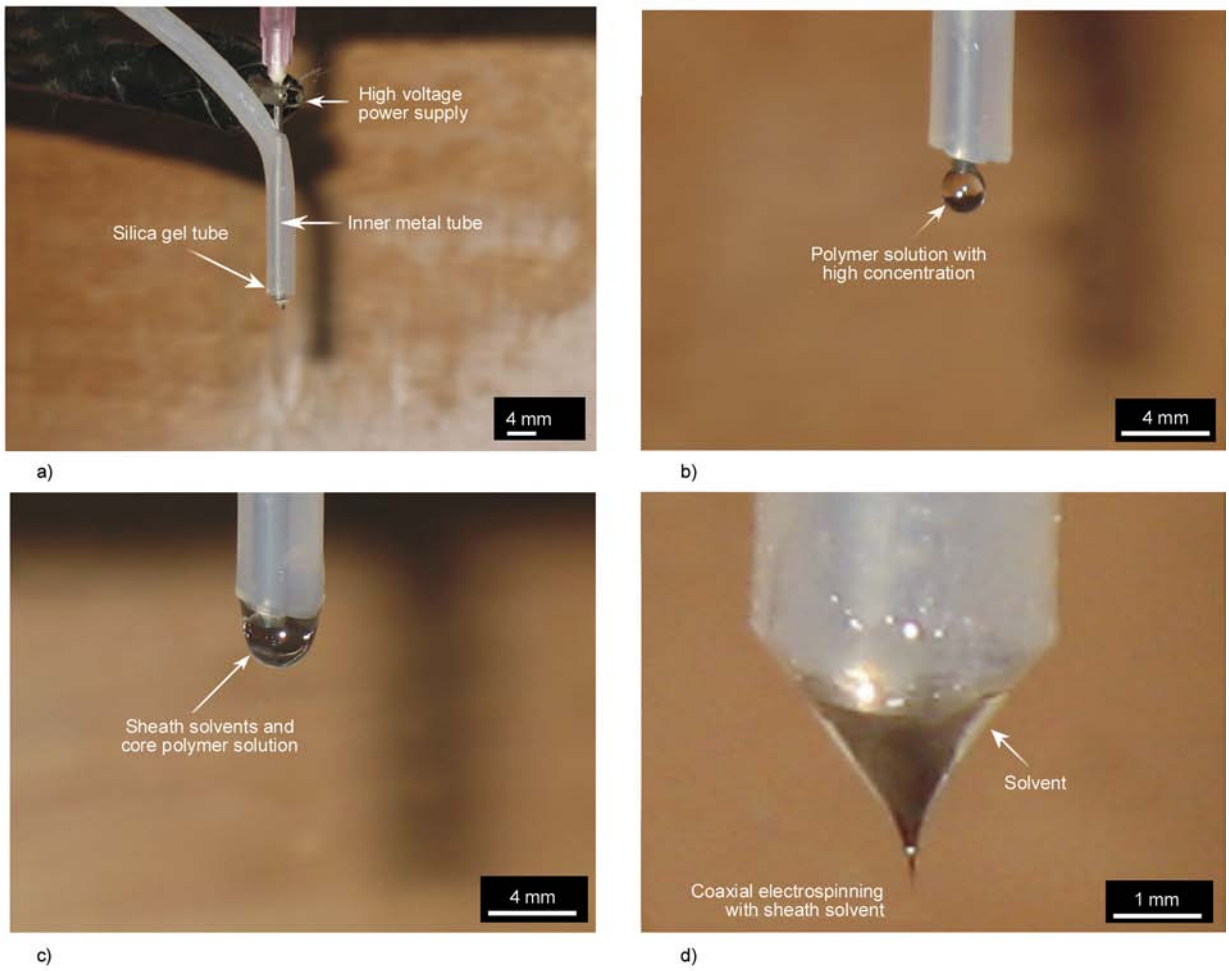

Figure 3. Modified coaxial electrospinning. a) Arrangement of spinneret, b) and c) 35% (w/v) PVP droplets without and with sheath DMAc, respectively, d) morphologies of a Taylor cone and jet formed in the electrical field using a DMAc-to-PVP-solution flow rate ratio of 0.1.

scale fibers from a liquid and the process shares characteristics of both electrospraying and conventional solution dry spinning of fibers. In the present electrospinning process, the formation of the Taylor cone, and the thinning of the jet occurred when they were surrounded by a solvent, instead of the ambient atmosphere in the conventional electrospinning process. The formation of gel-like skin and clogging of the spinning head that results from conventional electrospinning of high concentration polymer solutions could be retarded by preventing the loss of polymer solution solvent at the droplet-air and jet-air interface effectively, using an additional solvent as sheath fluid.

3.3. Fibers collected at different positions from the spinneret

Figure 4a to e shows optical images of electrospun fibers that were prepared from 35% (w/v) PVP solution using the modified coaxial electrospinning process and collected at a distance of 5, 15, 18, 22 and 25 cm from the top of spinning head, respectively. A rule (Figure 1) was used to indicate the sampling place during the electrospinning process. The fibers shown in Figure 4a were collected from the straight thinning jet (5 cm), and had an estimated diameter of about 93 μm. The fibers shown in Figure 4b were collected just before the onset point of the instability regions (15 cm); their diameters were about 72 μm. Although there was a relatively long distance (10 cm) between the two collection points, a thinning effect on the fibers was not obvious. The fibers shown in Figure 4c were collected at on the onset point of whipping and bending (18 cm); they had an estimated diameter of 29 μm. At this point, the jet was subject to a number of electrically driven bending instabilities that caused the fluid path to become a series of coiled

coils [34], resulting in the special fiber morphology observed here.

All the fibers shown in Figure 4a, b and c were still 'wet'. They had a flat morphology and were bonded together at joint points, suggesting that the true fiber diameter is a little smaller than the measured data. In addition, unusual bubbles were observed on the fibers shown in Figure 4b and c (inset). This phenomenon can be attributed to evaporation of the inner solvent during the thinning jet flight and drawing processes. The presence of these bubbles indicate that the surface of the jet fluids was differ-

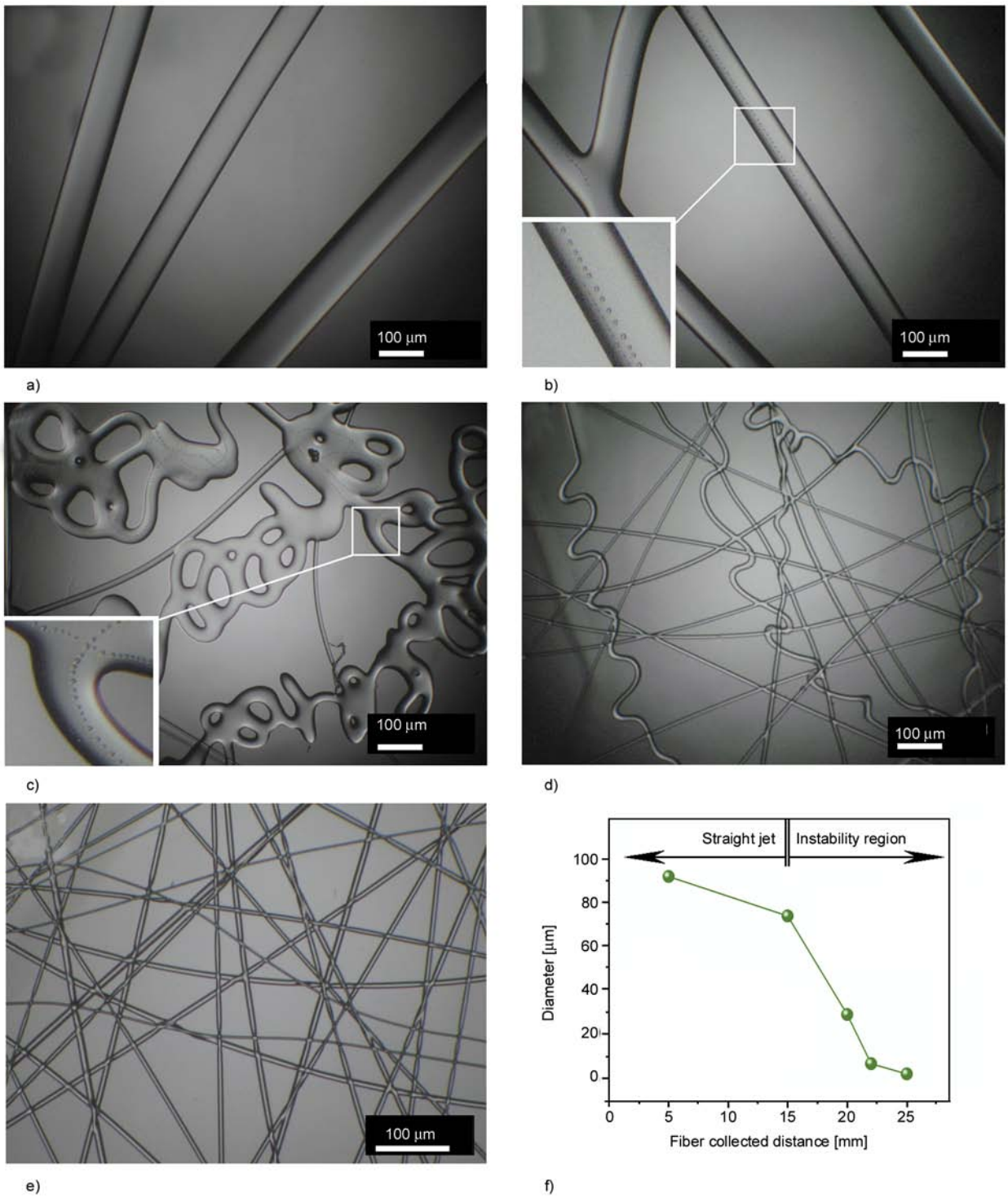

Figure 4. Polarized microscopic images of fibers collected at different positions from the spinning head (a) to e)), and the observed change in fiber diameter with collection distance. a) to e) correspond to a distance of 5, 15, 18, 22 and 25 cm, respectively.

ent from their core, and was still soft enough for the inner solvent to penetrate out and evaporate during the drawing process.

Figure 4f shows how collection distance affects fiber diameter. In the thinning jet region of the plot the fibers' diameter decreased to only a small extent mainly due to the drawing effect of the vertical electric force and to evaporation of the solvents. At longer collection distances, the fiber diameters decreased dramatically to several micrometers after the onset of the instability region. It is the electronic repulsion from Coulombic force occurred on the polymer jet surface that mainly expanded the fiber circular cross-sections and created the significant elongation of straight fibers before homogeneous fiber solidification. The whipping and bending processes were similar to those in the traditional electrospinning process. The surrounding DMAc had kept them at a fluid state for elongation in the instability region. At even longer collection distances, the decrease of fiber diameters would slow down or till stop mainly due to decrease of charge densities, evaporation of most of the solvent and gradual solidification of the fibers [34].

Figure 5a and b show SEM images of fibers collected at a distance of 28 cm from the nozzle of the spinneret. The fibers have a smooth surface, and homogeneous structure with an average diameter of 2.02±0.25 μm (Figure 5c). Figure 5d shows SEM images of fibers from 10% PVP solutions, which has an even wider fiber diameter distribution (140/650·100% = 22%) than fibers from the modified coaxial electrospinning process (250/2020·100% = 12%). Coaxial electrospinning with pure solvent as sheath fluid makes the process, the formation of Taylor cone and the thinning straight jet more stable than a single fluid electrospinning process conducted in an open atmosphere.

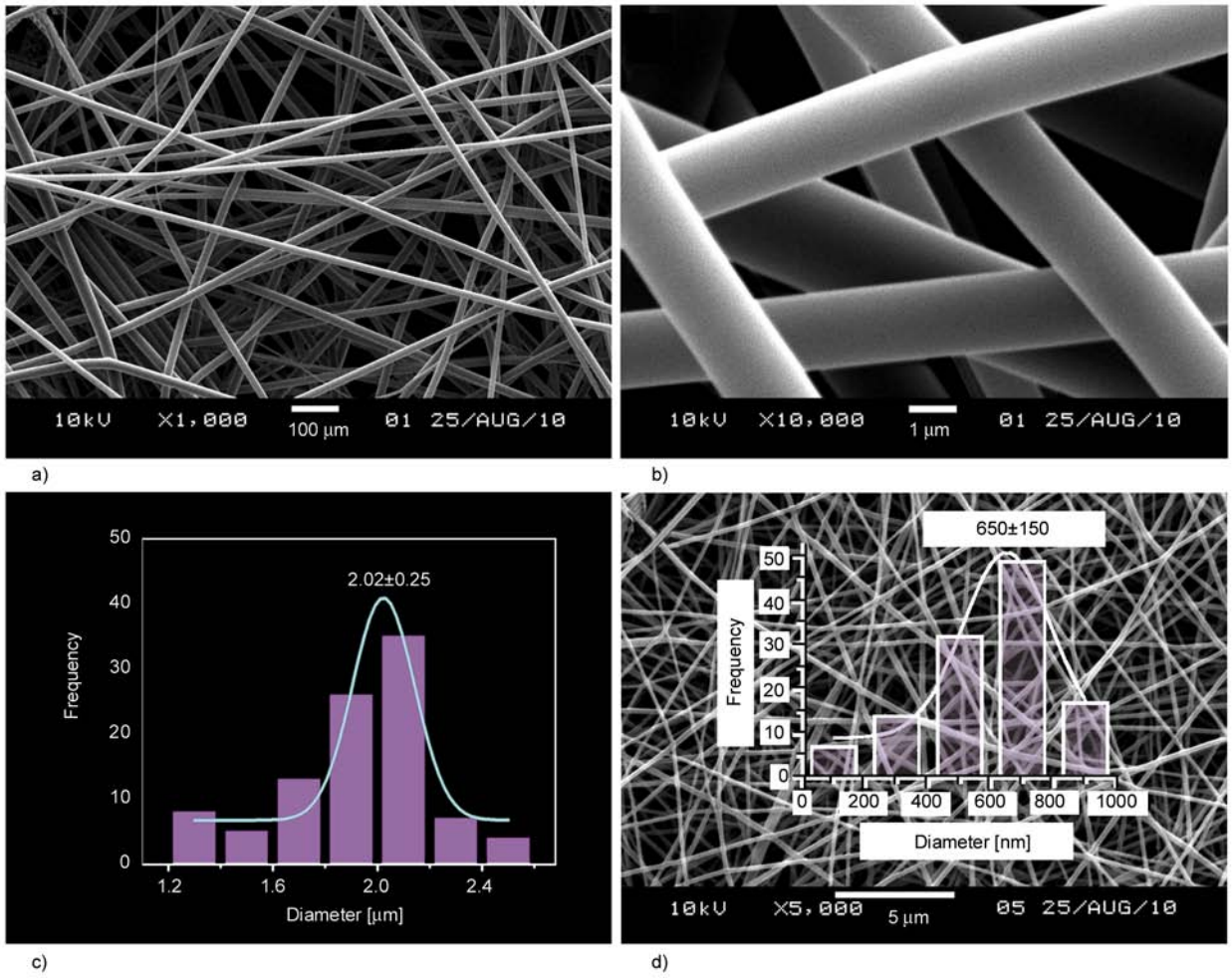

Figure 5. SEM images of the ultra-fine fibers. a) and b) fibers prepared by the modified coaxial electrospinning from 35% (w/v) PVP solutions with DMAc as sheath fluid and a DMAc-to-PVP-solution flow rate ratio of 0.1, under different magnifications, c) fiber diameter distribution, d) fibers prepared from 10% w/v PVP solutions using the traditional single fluid electrospinning.

4. Conclusions and outlooks

This study investigated a new process technology modified from coaxial electrospinning for preparing ultrafine fibers from high concentration polymer solutions. The modified process is characterized by a solvent surrounding a polymer solution in the spinneret, and can be easily assembled by simply using a metal needle to penetrate through an elastic silica gel tube and using two syringe pumps. PVP, which has a normal electrospinnable concentration of 10% in ethanol, was successfully spun into ultrafine fibers from a solution with a concentration of 35% (w/v) using the process developed here with DMAc as the surrounding solvent. Polarized microscopic observations revealed the process of formation of ultrafine fibers. They verified that the surrounding DMAc effectively facilitated the electrospinning process through retarding the fast evaporation of ethanol from the Taylor cone and the straight thinning jet. The SEM results demonstrated that the resultant fibers had smooth surface morphology and high structural uniformity.

The modified coaxial electrospinning process reported here can open a new window to tune the polymer fibers obtained by the electrospinning and improve its capability in processing polymer materials. It is obvious that electrospinning with a surrounding solvent will bring out more and new possibilities than traditional electrospinning process in air. For example, it may: (1) facilitate the electrospinning process through eliminating the clogging of spinneret that is often taken place in the electrospinning of spinning solutions in a low boiling point organic solvent; (2) extend the range of electrospinnable concentrations of polymer solutions; (3) improve the productivity of the electrospinning process; (4) enable to prepare nanofibers from polymers without electrospinnability owing to lack of suitable solvents through coagulating in a surrounding solvent environment; (5) enable to prepare nanofibers from polymers without electrospinnability owing to dilute concentration through extraction of the abundant solvent in the core solution using a poor solvent of the polymer as sheath fluid.

Acknowledgements

We would like to thank the China Postdoctoral Science Foundation (NO. 200902195) and UK-CHINA Joint Laboratory for Therapeutic Textiles for financial supports.

References

[1] Greiner A., Wendorff J. H.: Electrospinning: A fascinating method for the preparation of ultrathin fibers. Angewandte Chemie International Edition, **46**, 5670–5703 (2007).
DOI: 10.1002/anie.200604646

[2] Nagy Zs. K., Nyúl K., Wagner I., Molnár K., Marosi Gy.: Electrospun water soluble polymer mat for ultrafast release of Donepezil HCl. Express Polymer Letters, **4**, 763–772 (2010).
DOI: 10.3144/expresspolymlett.2010.92

[3] Yu D-G., Shen X-X., Branford-White C., White K., Zhu L-M., Bligh S. W. A.: Oral fast-dissolving drug delivery membranes prepared from electrospun PVP ultrafine fibers. Nanotechnology, **20**, 055104/1–055104/9 (2009).
DOI: 10.1088/0957-4484/20/5/055104

[4] Yu D-G., Gao L-D., White K., Branford-White C., Lu W-Y., Zhu L-M.: : Multicomponent amorphous nanofibers electrospun from hot aqueous solutions of a poorly soluble drug. Pharmaceutical Research, **27**, 2466–2477 (2010).
DOI: 10.1007/s11095-010-0239-y

[5] Rutledge G. C., Fridrikh S. V.: Formation of fibers by electrospinning. Advanced Drug Delivery Review, **59**, 1384–1391 (2007).
DOI: 10.1016/j.addr.2007.04.020

[6] Dhanalakshmi M., Jog J. P.: Preparation and characterization of electrospun fibers of Nylon 11. Express Polymer Letters, **2**, 540–545 (2008).
DOI: 10.3144/expresspolymlett.2008.65

[7] Heikkilä P., Harlin A.: Electrospinning of polyacrylonitrile (PAN) solution: Effect of conductive additive and filler on the process. Express Polymer Letters, **3**, 437–445 (2009).
DOI: 10.3144/expresspolymlett.2009.53

[8] Tripatanasuwan S., Zhong Z., Reneker D. H.: Effect of evaporation and solidification of the charged jet in electrospinning of poly(ethylene oxide) aqueous solution. Polymer, **48**, 5742–5746 (2007).
DOI: 10.1016/j.polymer.2007.07.045

[9] Gupta P., Elkins C., Long T. E., Wilkes G. L.: Electrospinning of linear homopolymers of poly(methyl methacrylate): Exploring relationships between fiber formation, viscosity, molecular weight and concentration in a good solvent. Polymer, **46**, 4799–4781 (2005).
DOI: 10.1016/j.polymer.2005.04.021

[10] Cengiz F., Dao T. A., Jirsak O.: Influence of solution properties on the roller electrospinning of poly(vinyl alcohol). Polymer Engineering and Science, **50**, 936–943 (2009).
DOI: 10.1002/pen.21599

[11] Liu Y., He J-H., Yu J-Y., Zeng H-M.: Controlling numbers and sizes of beads in electrospun nanofibers. Polymer International, **57**, 632–636 (2008).
DOI: 10.1002/pi.2387

[12] Wang C., Chien H-S., Hsu C-H., Wang Y-C., Wang C-T., Lu H-A.: Electrospinning of polyacrylonitrile solutions at elevated temperatures. Macromolecules, **40**, 7973–7983 (2007).
DOI: 10.1021/ma070508n

[13] Reneker D. H., Yarin A. L., Fong H., Koombhongse S.: Bending instability of electrically charged liquid jets of polymer solutions in electrospinning. Journal of Applied Physics, **87**, 4531–4547 (2000).
DOI: 10.1063/1.373532

[14] Varesano A., Carletto R. A., Mazzuchetti G.: Experimental investigations on the multi-jet electrospinning process. Journal of Materials Processing Technology, **209**, 5178–5185 (2009).
DOI: 10.1016/j.jmatprotec.2009.03.003

[15] Demir M. M.: Investigation on glassy skin formation of porous polystyrene fibers electrospun from DMF. Express Polymer Letters, **4**, 2–8 (2010).
DOI: 10.3144/expresspolymlett.2010.2

[16] Park S., Park K., Yoon H., Son J. G., Kim G. H.: Apparatus for preparing electrospun nanofibers: Designing an electrospinning process for nanofiber fabrication. Polymer International, **56**, 1361–1366 (2007).
DOI: 10.1002/pi.2345

[17] Wang M., Yu J-H., Kaplan D. L., Rutledge G. C.: Mechanical properties of electrospun silk fibers. Macromolecules, **37**, 6856–6864 (2004).
DOI: 10.1021/ma048988v

[18] Zhang J-F., Yang D-Z., Xu F., Zhang Z-P., Yin R-X., Nie J.: Electrospun core–shell structure nanofibers from homogeneous solution of poly(ethylene oxide)/chitosan. Macromolecules, **42**, 5278–5284 (2009).
DOI: 10.1021/ma900657y

[19] Gupta P., Wilkes G. L.: Some investigations on the fiber formation by utilizing a side-by-side bicomponent electrospinning approach. Polymer, **44**, 6353–6359 (2003).
DOI: 10.1016/S0032-3861(03)00616-5

[20] Chen H-M., Yu D-G.: An elevated temperature electrospinning process for preparing acyclovir-loaded PAN ultrafine fibers. Journal of Materials Processing Technology, **210**, 1551–1555 (2010).
DOI: 10.1016/j.jmatprotec.2010.05.001

[21] Wu Y., Yu J-Y., He J-H., Wan Y-Q.: Controlling stability of the electrospun fiber by magnetic field. Chaos Solitons Fractals, **32**, 5–7 (2007).
DOI: 10.1016/j.chaos.2006.05.023

[22] Liu Y., He J-H.: Bubble electrospinning for mass production of nanofibers. International Journal of Nonlinear Sciences and Numerical Simulation, **8**, 393–396 (2007).

[23] Tripatanasuwan S., Zhong Z., Reneker D. H.: Effect of evaporation and solidification of the charged jet in electrospinning of poly(ethylene oxide) aqueous solution. Polymer, **48**, 5742–5746 (2007).
DOI: 10.1016/j.polymer.2007.07.045

[24] Hsu C-M., Shivkumar S.: Nano-sized beads and porous fiber constructs of poly(ε-caprolactone) produced by electrospinning. Journal of Materials Science, **39**, 3003–3013 (2004).
DOI: 10.1023/B:JMSC.0000025826.36080.cf

[25] Kanjanapongkul K., Wongsasulak S., Yoovidhya T.: Investigation and prevention of clogging during electrospinning of zein solution. Journal of Applied Polymer Science, **118**, 1821–1829 (2010).
DOI: 10.1002/app.32499

[26] Li Y., Lim L-T., Kakuda Y.: Electrospun zein fibers as carriers to stabilize (–)-epigallocatechin gallate. Journal of Food Science, **74**, 233–240 (2009).
DOI: 10.1111/j.1750-3841.2009.01093.x

[27] Yu D-G., Branford-White C., White K., Li X-L., Zhu L-M.: Dissolution improvement of electrospun nanofiber-based solid dispersions for acetaminophen. AAPS PharmSciTech, **22**, 809–817 (2010).
DOI: 10.1208/s12249-010-9438-4

[28] Yu D. G., Yang J. M., Branford-White C., Lu P., Zhang L., Zhu L. M.: Third generation solid dispersions of ferulic acid in electrospun composite nanofibers. International Journal of Pharmaceutics, **400**, 158–164 (2010).
DOI: 10.1016/j.ijpharm.2010.08.010

[29] Yu D-G., Zhang X-F., Shen X-X., Branford-White C., Zhu L-M.: Ultrafine ibuprofen-loaded polyvinylpyrrolidone fiber mats using electrospinning. Polymer International, **58**, 1010–1013 (2009).
DOI: 10.1002/pi.2629

[30] Bühler V.: Polyvinylpyrrolidone excipients for pharmaceuticals: Povidone, crospovidone and copovidone. Springer, Berlin (2005).

[31] Crowley J. M.: Role of Joule heating in the electrostatic spraying of liquids. Journal of Applied Physics, **48**, 145–147 (1977).

[32] Chew S. Y., Hufnagel T. C., Lim C. T., Leong K. W.: Mechanical properties of single electrospun drug-encapsulated nanofibres. Nanotechnology, **17**, 3880–3891 (2006).
DOI: 10.1088/0957-4484/17/15/045

[33] Moon J., Park J-A., Lee S-J., Lim S. C., Zyung T.: Structure and electrical properties of electrospun ZnO–NiO mixed oxide nanofibers. Current Applied Physics, **9**, 213–216 (2009).
DOI: 10.1016/j.cap.2008.12.020

[34] Reneker D. H., Yarin A. L.: Electrospinning jets and polymer nanofibers. Polymer, **49**, 2387–2425 (2008).
DOI: 10.1016/j.polymer.2008.02.002

eXPRESS Polymer Letters Vol.5, No.8 (2011) 742–752
Available online at www.expresspolymlett.com
DOI: 10.3144/expresspolymlett.2011.72

Fabrication and characterization of polycaprolactone/calcium sulfate whisker composites

J. Y. Liu[1,2], *L. Reni*[1], *Q. Wei*[3], *J. L. Wu*[1], *S. Liu*[1], *Y. J. Wang*[1], *G. Y. Li*[2*]

[1]School of Materials Science and Engineering, South China University of Technology, Guangdong, 510640, China
[2]School of Electronic and Information Engineering, South China University of Technology, Guangdong, 510640, China
[3]China National Analytical center, Guangzhou, 510070, China

Received 9 December 2010; accepted in revised form 1 March 2011

Abstract. Polycaprolactone (PCL)/calcium sulfate (CS) whisker composites have been fabricated by melt blending and coprecipitation methods respectively. Scanning electron microscope (SEM) was used to observe the microstructure of the composites. The crystallization and thermal properties were characterized by polarized optical microscope (POM), X-ray diffractometry (XRD), differential scanning calorimetry (DSC), and thermogravimetric analysis (TGA). For composites prepared by melt blending method, experiment results show that average length of the whiskers is shortened. The crystallization perfection of PCL in composites is improved by adding whiskers. The flexural strength increases whereas the impact strength decreases. For composites prepared by coprecipitation method, whisker addition worsens the crystallization perfection of PCL. An improvement of 21% in flexural strength and 22% in impact strength has been achieved for the composite with 15 wt% of whiskers.

Keywords: *biopolymers, biocomposites, polycaprolactone, calcium sulfate whisker, mechanical propertie*

1. Introduction

Polycaprolactone (PCL) is a type of synthetic, biodegradable polymer, applying in food packaging, tissue engineering, dressing for wound, and drug delivery [1–3]. So it becomes one of the most promising biodegradable polymers currently available on the market. However, some shortcomings such as high costs, low melting temperature and low mechanical properties restrict widespread industrial use of PCL [4]. In order to improve the physical properties of polymer, inorganic particles were usually used to improve some properties of the polymer. For instance, Wang *et al.* [5] used titania to enhance the mechanical properties of poly (lactic-co-glycolic acid). Their investigation indicated that the composite microsphere-sintered scaffold is a promising scaffold for bone repair. It is reported that PCL mixed with other biodegradable inorganic materials such as hydroxyapatite (HA) [6–10] and tricalcium phosphate (TCP) [11–13] could improve some properties so that the composites may offer attractive potential for bone tissue replacement and tissue regeneration.

Besides HA and TCP, CS as a biodegradable inorganic material is widely used in bone surgery as well. It was reported that CS was used for treating bone defects as early as 1892. Compared with HA and TCP, CS has a reasonable degradation rate [14–16] and has been widely used in bone treatment. As reported, CS can form calcium phosphate deposits when it is in contact with body fluids, which are finally responsible for conducting and accelerating bone formation [17]. La Gatta *et al.* [18] reported an injectable PCL/CS system for bone regeneration. They mixed calcium sulfate hemi-hydrate (CHS) with a photo-crosslinkable derivative of PCL, and

*Corresponding author, e-mail: phgyli@scut.edu.cn

the composite is proposed to be utilized in hard tissue repair particularly in the dental and orthopaedic field. Gao *et al.* [19] reported a composite fabricated with PLLA and CS power for bone repair. However, the mechanical property of this material, one of basic and important property for materials, has not been reported. Like most other inorganic powders, CS is a kind of brittle filler. It can reinforce polymer but untreated CS powder may damage the toughness of materials.

Being different from inorganic powder, whisker is considered to be an attractive alternative to short glass or carbon fibers for reinforcing and toughening thermoplastics and has attracted considerable interests of scientists and engineers [20]. A lot of work has been focused on the preparation of various polymer/inorganic whiskers composites [14, 21, 22]. It was reported that CS whisker was investigated to reinforce polyurethane elastomer [21], polypropylene [22] and non-metallic friction material [23]. These hybrid composites were generally produced by melt or solution blending method. However, the difference between two blending methods for the same material has not been reported. In addition, whiskers are often used to reinforce polymer, but calcium sulfate whisker is rarely reported to reinforce biopolymer materials.

Since PCL and calcium sulfate are well-known biocompatible and bioactive materials used in bone tissue engineering, the relevant composites with high mechanical properties should be promising materials for application in bone repair. It is also worth to note that all materials used for repairing bone tissue or other application need to have excellent mechanical properties. However, based on the literature review, it can be found that most efforts concentrated on preparation, bioactivity, and biodegradation of the PCL materials, and only a few works focused on the effect of whisker composition and preparation method on the mechanical properties. To improve mechanical properties of PCL and study the influence of blending method and CS whiskers on the crystallization, thermal behavior, and mechanical properties of the composites, PCL/CS whisker composites containing different CS contents (0, 5, 10, 15, and 20 wt %) were prepared by melting and coprecipitation blending methods respectively. The effects of whisker addition and different fabrication processes on the microstructure and properties of the composites such as the morphology, crystallization, thermal behavior, and mechanical properties have been investigated.

2. Experimental details

2.1. Materials and fabrication

Polycaprolactone (PCL) (W_η = 50 000) used in this experiment was purchased from Dow Chemical Co., Ltd, China and calcium sulfate (CS) whisker (length/diameter ratio: 40:1, and diameter: 1~6 μm) was supplied by Jian-kun Chemical Co., Ltd, China. The SEM photographs of the whiskers is shown in Figure 1.

In this research, PCL/calcium sulfate whisker composites were prepared by both melt and coprecipitation blending methods. For melt blending method, the pre-dried CS whiskers were premixed with PCL on a laboratory size two-roll mixing mill (Scientific Laboratory Bench Top Two-Roll Mill, LRM-M-100, China Vision Group CO., Limited) at 58ºC. The premixed composite was extruded using a Haake twin-screw extruder (Mini-lab II, Thermo Electron Corp., Hamburg, Germany) with a speed of 60 rpm at 100ºC. The composite was then injected using a Haake mini injection machine (Mini jet II, Thermo Electron Corp., Hamburg, Germany) under a pressure of 35 MPa. Before injection, the injection cylinder and the mold were preheated to the temperatures of 100 and 40ºC, respectively. The shape of molded samples is in accordance with ASTM D790 and ASTM D256 standards.

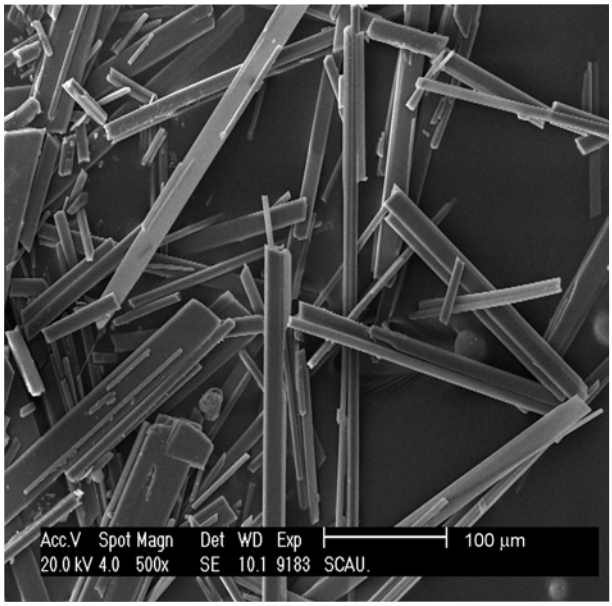

Figure 1. SEM micrograph of CS whiskers

For coprecipitation method, appropriate amount of PCL and CS whiskers were prepared to the desired weight fractions, and then separately, the PCL particles were dissolved in tetrahydrofuran (THF) (AR, Shengqiang Chemical Co., Ltd., Jiangsu, China) solvent and CS whiskers were dispersed in tetrahydrofuran (THF) solvent using a magnetic stirrer for about 120 min. Next, the PCL-THF solution and CS-THF dispersed liquid were mixed together and stirred for another 120 min. The mixture was then poured into ethanol (AR, Fuyu Chemical Co., Ltd., Tianjin, China) as nonsolvent to coprecipitate PCL/CS composite. After filtration, the recovered composite was washed using anhydrous ethanol to remove the residual THF. The flocculent composite was then vacuum-desiccated for about 12 hours at 45ºC, and finally the floc was hot-pressed for 5 min at 70ºC under a pressure of about 15 MPa to get samples.

2.2. Characterization

The flexural property was tested by an electronic universal testing machine (LR5K Plus, Lloyd instruments Ltd., England) according to the standard ASTM D790, and the rate of crosshead motion was set to be 2 mm/min. The notched impact test was performed by a pendulum-type impact test machine (Shenzhen Sans testing machine Co., Ltd., China) according to the standard ASTM D 256. Five samples were tested for each composition. The microstructure of the composites was observed by an environmental scanning electron microscopy (SEM, XL30, Phillips, Netherlands). Prior to the observation by SEM, the impact fractured cross-section of specimens was coated with Au by sputtering deposition. SEM micrographs were dealt with Image-Pro Plus software to measure the length of the whiskers in the composites. X-ray diffraction spectra were obtained by an X' Pert Pro diffractometer (PA Nalytical, Netherlands) with a Cu target and K_α radiation at a scanning rate of 2°C/min to study the changes of the crystal structure of PCL.

The thermal behavior and crystallization of the composites were examined by a differential scanning calorimeter (DSC, Netzsch 204, Germany) under N_2 flow (70 ml/min) and liquid nitrogen controlled cooling. In this study, the samples were firstly heated from room temperature to 100ºC, equilibrated for 2 min to eliminate thermal history, and then cooled at 10ºC/min to –120ºC, equilibrated at –120ºC for 2 min, and finally heated up again to 100ºC at 10ºC/min. Thermal decomposition studies were carried out using a thermogravimetric analysis (TGA, Netzsch TG 209, Germany) under inert flowing nitrogen (40 ml/min) from 50 to 700ºC at a heating rate of 10ºC/min.

The spherulite structure of PCL/CS whisker composites was studied by a polarized optical microscope (POM, BX51-P, Linkamthms600, Japan) equipped with a Linkam hot stage (THMS600/HFS91, Japan). In this experiment, the samples placed between two glass slides were heated up to 100°C, and then equilibrated at this temperature for 5 min to eliminate any residual PCL crystallization seeds, and finally crystallized for 30 min at room temperature. PCL spherulites were examined by POM and recorded by an attached digital camera.

3. Results and discussion

3.1. Morphology of fracture surfaces

To study the dispersion of fillers and fracture surface, the impact-fractured cross-section of specimen was observed by SEM and the micrographs of the fracture surface of PCL/CS whisker composites are shown in Figure 2. The length of the whiskers in composites calculated by Image-Pro Plus software is listed in Table 1. For composites prepared by melting method, no obvious agglomeration of CS whiskers was observed. However, some whiskers were broken down so that the average length of whiskers become shorter, which could make the mechanical properties deteriorate [24]. For composites prepared by coprecipitation method, it could also be found that no obvious agglomeration of CS whiskers was observed. Figure 2d reveals that some of the whiskers were pulled out and broken down during impact test (X point), and the surfaces of CS whiskers and matrix do not closely adhere together (Y point), which indicates that the interfacial debonding between whiskers and matrix took place during the test. Additionally, plastic deformation of PCL at interface is observed clearly, which indicates the processes of pull-out and debonding dissipate a part of impact energy. The data in Table 1 show that the average length of the whisker for the composites prepared by melting method is shorter than that prepared by coprecipitation method. The possible reason is that, compared to the magnetic stirrer, the

Table 1. Length of CS whiskers in composites prepared by melting and coprecipitation methods

Fabrication method	Content of CS whisker [%]	Length [μm]			Standard deviation
		Min	Max	Mean	
Melting method	5	2.00	30.83	7.79	6.30
	15	5.99	55.69	17.00	12.96
	20	1.00	17.14	6.55	3.30
Coprecipitation method	5	16.84	43.46	32.64	10.81
	15	10.33	87.13	36.66	21.82
	20	5.78	91.89	26.01	20.30

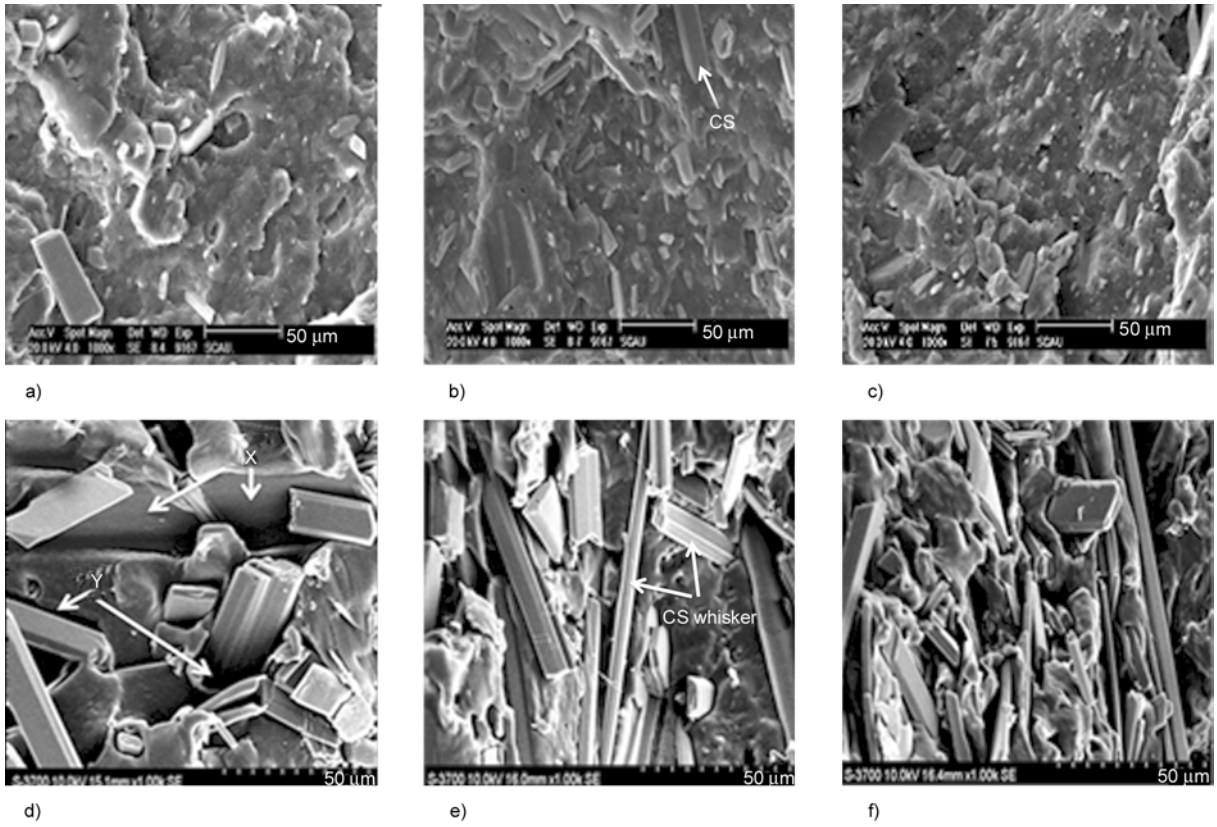

Figure 2. SEM micrographs of fracture surfaces for PCL/CS whisker composites prepared by melting method containing (a) 5 wt%, (b) 15 wt%, and (c) 20 wt% whisker, and prepared by coprecipitation method containing (d) 5 wt%, (e) 15 wt%, and (f) 20 wt% whisker.

shear stress of the screws in the extruder is so large for the CS whiskers that some of the whiskers are easily broken down during the process.

3.2. Crystallization

Figure 3 shows the XRD spectra of CS whisker, pure PCL and the composites prepared by two methods. Results show that PCL contains three strong reflections at the angles (2θ) of about 21.4, 22.0 and 23.7°, corresponding to the (110), (111) and (200) planes of the orthorhombic crystal structure respectively [25]. XRD pattern of pure CS whisker indicates that the CS whisker in this experiment is $CaSO_4 \cdot 2H_2O$ [26]. Comparing the XRD pattern of the pure PCL with composite, it can be found that the strong reflections observed from PCL are also present in PCL/CS whisker composites. This indicates that the basic crystal structure of the PCL matrix in composites is still orthorhombic. For the composites, the reflection peaks at the angle of 20.8 and 11.5° are the characteristic peaks of $CaSO_4 \cdot 2H_2O$ whiskers [26]. Results also show that the reflection peaks of the composites at the angle of 21.4° move slightly to the larger angles compared to the pure PCL. It demonstrates that the d spacing of PCL in the composites decreases. This phenomenon may be caused by the fact that the whisker hampers the growth of the crystal grain, which would compress the cell. However, for the composites with 5 wt% whiskers prepared by melting method, the number

Table 2. Thermal and crystallization properties of PCL/CS whisker composites prepared by melting and coprecipitation methods

Crystallization and thermal parameters	Fabrication method	Content of CS whisker [%]			
		0	5	15	20
Crystallizaion temperature (T_c [ºC])	Coprecipitation	27.6	31.5	30.7	30.5
	Melting		30.4	33.0	33.1
Melting temperature (T_m [ºC])	Coprecipitation	57.9	58.7	58.3	58.5
	Melting		58	59	58.4
Glass transition temperature (T_g [ºC])	Coprecipitation	–62.0	–62.4	–61.5	–61.1
	Melting		–62.5	–63.2	–62.8
Undercooling (ΔT [ºC])	Coprecipitation	30.3	27.2	27.6	27.0
	Melting		27.6	26.0	25.3
Half peak width {$(\Delta T)_p$ [ºC]}	Coprecipitation	12.0	8.0	7.0	7.0
	Melting		5.0	5.5	5.0
Crystallinity (Cr [%])	Coprecipitation	54.6	46.1	47.4	54.6
	Melting		52.7	54.4	54.9

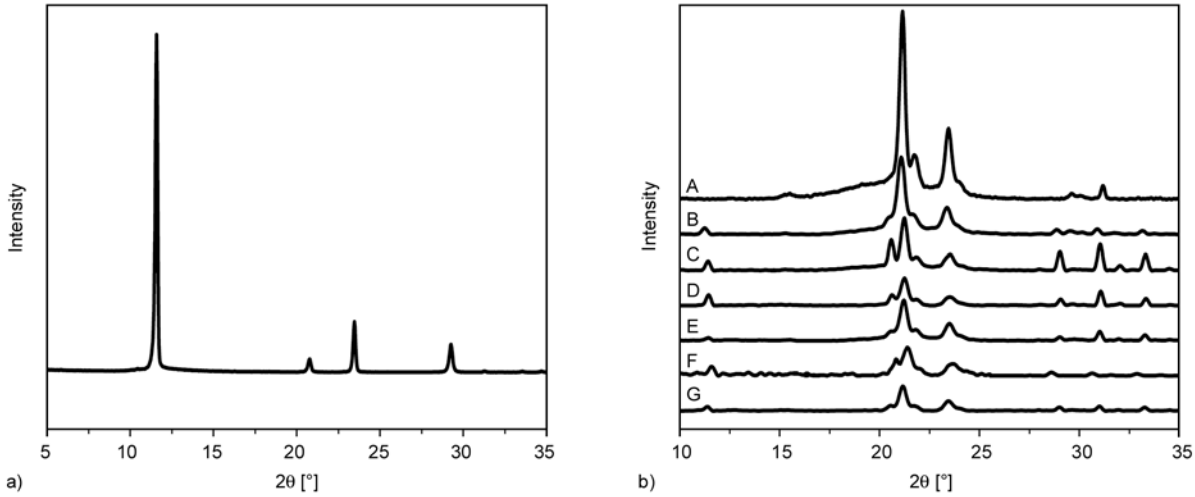

Figure 3. X-Ray spectra for (a) whiskers, (b) (A) pure PCL and composites prepared by melting method containing (B) 5 wt%, (C) 15 wt%, and (D) 20 wt% whisker, and prepared by coprecipitation method containing (E) 5% wt%, (F) 15 wt%, and (G) 20 wt% whisker

and scale of whiskers for the composites prepared by melt blending method are less than that of other composites, therefore the whiskers weakly hamper the growth of the grain and the d spacing and reflection peaks almost do not change.

Table 2 shows the thermal and crystallization properties parameters of pure PCL and PCL/CS whisker composites determined by DSC measurement. The undercooling ΔT in Table 2 is defined using Equation (1) [27]:

$$\Delta T = T_m - T_c \quad (1)$$

where T_m and T_c are the melting temperature and crystallization temperature determined by DSC respectively. It can be observed from Table 2 that the T_c of the PCL in composites gradually goes up with the increase in weight fraction of the CS whisker, which indicates that the whisker has an excellent nucleating effect on the crystallization of PCL [28]. Results also show that the crystallization temperature of the composites prepared by melt blending method is higher than that prepared by coprecipitation method. This phenomenon might be caused by the change in size and number of the whiskers. As discussed above, some of the whiskers were broken down by shear stress of the screw during processing for melt blending method and the number of the whisker increased. This change could lead to the increase in the nucleation rate and hence enhance the crystallization rate. Additionally, a part of the molecular chain of PCL could be also broken down and became shorter during processing. The short molecular chain also has a nucleation effect, resulting in the increase of the nucleation rate of composites.

Undercooling can be used to characterize the crystallization rate of the polymer in the non-isothermal process. Generally, it is inversely proportional to the crystallization rate [29]. Results in Table 2 show that the undercooling ΔT of the composites decreases from 30.3 to 25.3ºC with increase in whisker composition by 20 wt%, and the ΔT of the composites prepared by melt blending method is lower than that prepared by coprecipitation method. These results further illustrate that whiskers have nucleation effect to PCL and the effect is relevant to the size of the whiskers. Although the number of the whiskers for the composites with 5% CS whiskers is less, it is enough to influence the nucleation of PCL so that ΔT is also lower than that of the pure PCL.

Generally, the crystallization perfection can be characterized by half peak width $(\Delta T)_p$ of the crystallization curve [29]. It can be seen from Table 2 that the half peak width $(\Delta T)_p$ of composites prepared by melt blending method is narrower about 7ºC than that of the pure PCL, and narrower about 2ºC than the composites prepared by coprecipitation method, which demonstrates that the crystallization perfection of the composites prepared by melt blending method is superior to that of both the pure PCL and the composites prepared by coprecipitation method. This phenomenon is associated to the shape of fillers. The fillers restrain the mobility of grain boundaries and eventually inhibit gain growth. It can be inferred from this result that the fillers with higher aspect ratio have a stronger restraining effect. The similar phenomenon was also reported by Vanherpe *et al.* [30] but the fillers were fibers. In this experiment, the aspect ratio of whiskers in composites prepared by coprecipitation method is higher than melt blending method, which leads to the stronger inhibiting effect. Therefore, the crystallization perfection of the composites prepared by melt blending method is better than that prepared by coprecipitation method.

To further illuminate the changes of crystallization properties, the crystallinity is calculated by using Equation (2) [31] and also listed in Table 2:

$$C_r = \frac{\Delta H_m}{\Delta H_m^0 \cdot X_n} \cdot 100\% \quad (2)$$

where ΔH_m is the melting enthalpy for composite samples, ΔH_m^0 is the melting enthalpy of the matrix when it infinitely crystallizes and it is 136.08 J/g for PCL [32], and X_n is the weight percentage of PCL in composites. Results show that the crystallinity of composites almost remains constant compared to pure PCL. However, the crystallinity of composites prepared by melting method is slightly higher than that prepared by coprecipitation method. This is accordance with the conclusion that the nucleation effect of the whisker for the composites prepared by melting method is stronger than that prepared by coprecipitation method.

3.3. Thermal behavior

The test data listed in Table 2 show that the melting temperature (T_m) and the glass transition temperature (T_g) of the samples exhibit a small change by adding CS whisker. To find the relationship among the thermal degradation property, composition of the CS whisker and preparing method, thermogravimetric analysis was conducted. Figure 4 illustrates TGA curves for pure PCL and its composites prepared by both methods with different compositions of CS whiskers. Thermal degradation parameters obtained from TGA curves are listed in Table 3. When 50% weight loss is selected as the point of comparison, the thermal decomposition temperature ($T_{0.5}$) for the pure PCL is 423ºC, and the $T_{0.5}$ for composites prepared by both methods changes slightly compared to the pure PCL. The mass loss at 150–200ºC for the composites is due to the loss of the crystal water in $CaSO_4 \cdot 2H_2O$ whiskers at low temperature. Previous studies found that there are different changes of the thermal decomposition for PCL/inorganic filler composites [33, 34]. For this experiment, the $T_{0.5}$ of composites is slightly lower

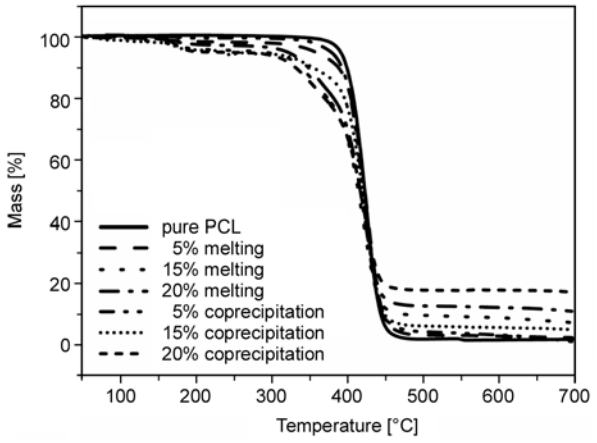

Figure 4. Thermogravimetric cureves for the pure PCL and composites prepared by both of melting and coprecipitation methods

Table 3. Thermal degradation properties of PCL/CS whisker composites prepared by melting and coprecipitation methods

Fabrication method		Melting				Coprecipitation		
Content of CS whisker [%]		0	5	15	20	5	15	20
Thermal degradation parameters	$T_{0.5}$ [ºC]	423	421	415	413	419	417	417
	Loss at 150–200ºC [%]	–	1.2	3.1	4.2	0.7	3.0	5.5

about 2–6ºC than that of the pure PCL. This may be due to the loss of the crystal water as well. The loss of the crystal water at low temperature may induce the decomposition of the PCL for the composites easily. As the PCL is decomposed, the residue should be the CS and a little chars of PCL, and the mass of residue is approximately equal to the mass of CS.

3.4. Spherulite morphology

The spherulite morphology of the pure PCL and the composites prepared by both methods is shown in Figure 5. It can be seen that the spherulite structure of pure PCL is imperfect, and there are some clear grain boundaries among the spherulites. Compared with the pure PCL, the spherulite size of all com-

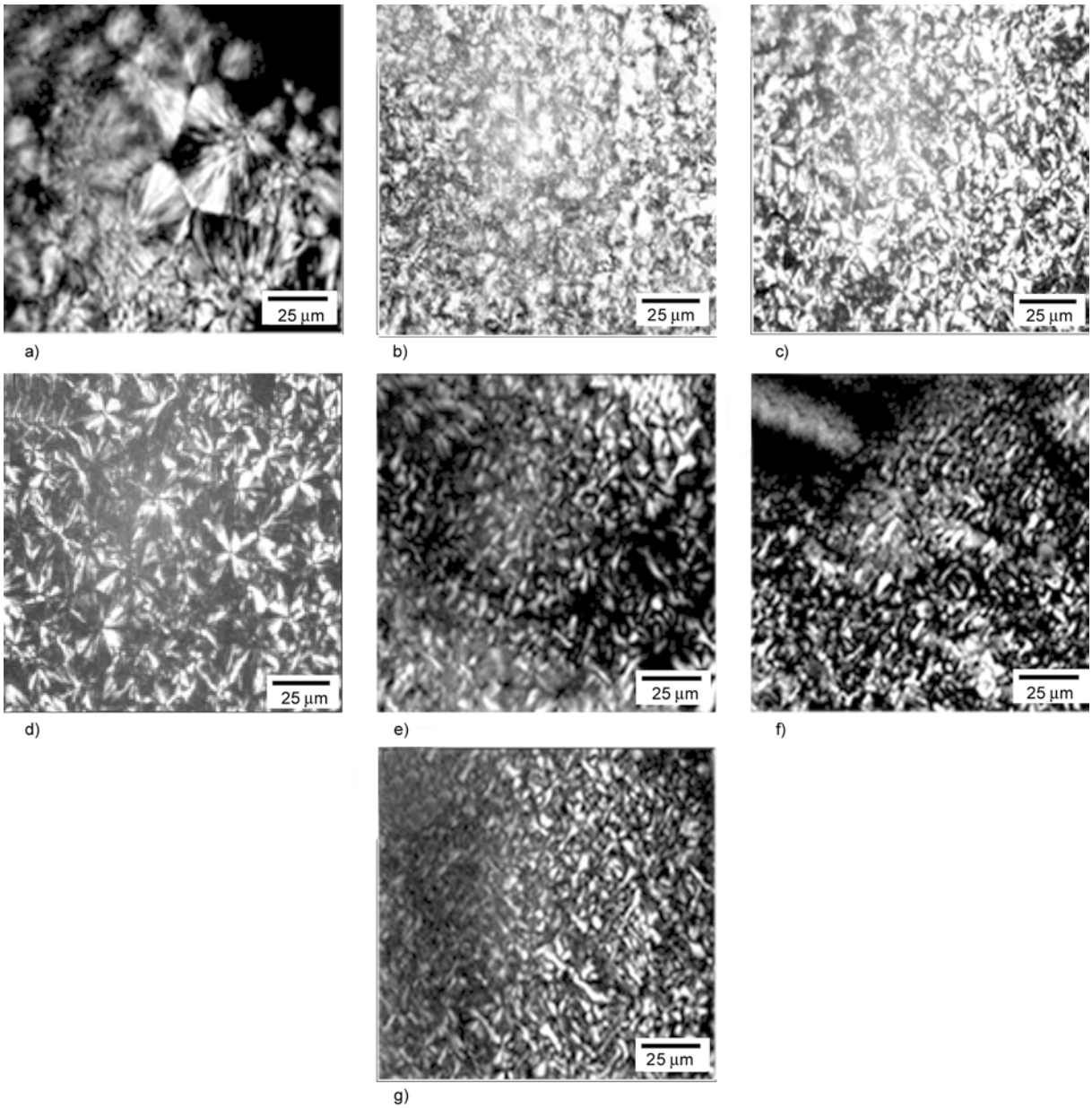

Figure 5. Spherulitic morphology (400×): (a) the pure PCL and composites prepared by melting method containing (b) 5 wt%, (c) 15 wt%, and (d) 20 wt% whisker, and by coprecipitation method containing (e) 5 wt%, (f) 15 wt%, and (g) 20 wt% whisker

posites significantly reduces, which illustrates that CS whiskers have grain refining effect to PCL. POM pictures in Figure 5 also reveal that the crystallization perfection of the composites prepared by melt blending method is better than that of the composites prepared by coprecipitation method, which is consistent with the result of DSC. However, it can be seen from Figure 5b–g that the spherulite size of the composites prepared by coprecipitation method is smaller than that of the composites prepared by melting method. It indicates that the grain refining effect of the long whiskers is stronger than that of the short whiskers.

3.5. Mechanical properties

Figure 6 and Figure 7 show the relationship between the composition of CS whisker and the flexural strength and modulus of composites. Results show

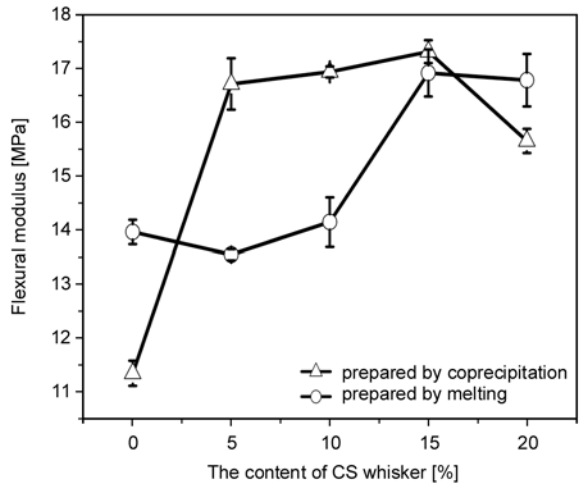

Figure 6. Relationship between the composition of CS whisker and the flexural strength of the composites

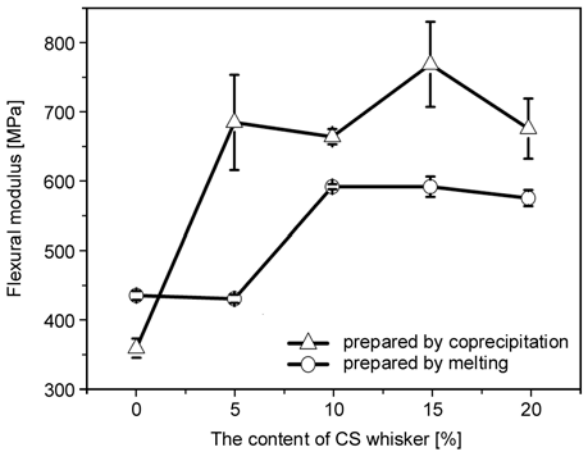

Figure 7. Relationship between the composition of CS whisker and flexural modulus of the composites

that for the pure PCL sample prepared by melting method, the flexural strength and modulus are 22 and 30% higher than that prepared by coprecipitation method. A lot of researchers reported that for pure polymer, mechanical properties were improved by different fabrication method, such as solid extrusion, hydrostatic extrusion, and hot tension-drawing, which aimed at the orientation of the molecular chain or structure of polymer to reinforce the polymer [35]. In this experiment, the orientation of molecular chain for PCL may occur in the mold during injection process and not happen during the coprecipitation mold-pressure process. Consequently, the flexural strength and modulus of pure PCL sample prepared by melting injection are higher than those prepared by coprecipitation method.

For composites prepared by coprecipitation method, the flexural strength and modulus of the samples containing 15 wt% CS whiskers are higher about 21% and 75% respectively than that of the pure PCL samples prepared by melting method. However, further increase in the composition of CS to 20 wt% leads to decrease of the flexural strength and modulus of the composites. Results also show that for the CS whiskers less than 20 wt%, the flexural strength and modulus of the composites prepared by melting method are lower than that of the composites prepared by coprecipitation method. This result can be explained by load-transfer theory [24]. Classical load-transfer theory suggests that the stress can transfer from polymer matrix to whiskers through the interfacial layer. Whiskers have higher modulus than the polymer matrix so that they can afford parts of stress to disperse the load in the matrix. Therefore, the strength of the whisker composites is improved by whisker addition. The load-transfer theory also suggests that the strength of the composites filled with long whisker should be higher than short whisker, which can explain why the flexural strength of CS whisker composites prepared by melt blending method is lower than that prepared by coprecipitation method.

Besides the length of whiskers, the dispersion of the whiskers in the matrix is also one of the important factors affecting the strength of the composites. It is well known that the agglomeration of the fillers can deteriorate the mechanical properties of the composites [22]. In this experiment, the decrease of the strength for the composite with higher CS whisker

composition of 20 wt% prepared by coprecipitation method may be mainly influenced by the agglomeration of the whiskers. For composites with 20 wt% CS whiskers prepared by melting method, the strength increases continually because of the better dispersion of CS whiskers. It reveals that, for composites with less than 15 wt% CS whisker, the length of the whiskers is the main factor to affect the flexural strength. For composites with 20 wt% CS whiskers, the dispersion of the whiskers becomes a main factor to affect the flexural strength.

Our results also show that the change trend of flexural modulus for composites is similar to the change of flexural strength. It indicates that although CS whisker belongs to the rigid filler which can improve the rigidity of materials [19], but the rigidity will not be improved infinitely with the addition of whiskers. The effect of the whiskers on the flexural modulus is similar to the flexural strength.

Figure 8 shows the relationship between the composition of CS whisker and notched impact strength of the composites. It can be seen that for the pure PCL, the impact strength of the sample prepared by melt blending method is about 3 times higher than that prepared by coprecipitation method. For composites prepared by melt blending method, the impact strength decreases gradually with the increase in CS whiskers. For composites prepared by coprecipitation method, the impact strength increases when the composition of CS whisker is less than 15 wt%, and then decreases when more than 15 wt%. However, it is still higher than that prepared by melt blending method.

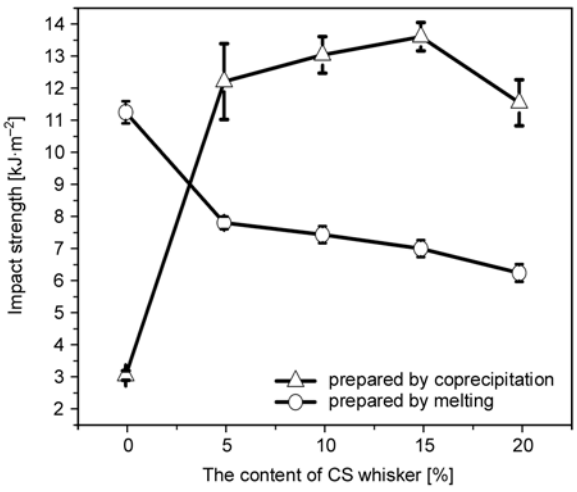

Figure 8. Relationship between the composition of CS whisker and notched impact strength of the composites

Generally, impact strength is sensitive to the defects of materials. In this study, defects such as small cavities could take place in the pure PCL samples prepared by coprecipitation method during the molding, whereas the small cavities rarely occur in pure PCL samples prepared by melt blending method. Therefore, the impact strength of the PCL samples prepared by melt blending method is higher than that prepared by coprecipitation method. The difference in impact strength between the composites prepared by two methods should be ascribed to several factors such as spherulite size, whisker debonding during impact test and whisker length. It is reported that the decrease of spherulite size will benefit the improvement of impact strength [27]. POM observation shows that the composites prepared by coprecipitation have smaller spherulite size. SEM pictures show that some CS whiskers debonded with PCL and were pulled out for the samples prepared by coprecipitation method, which could absorb a part of impact energy. Composites prepared by coprecipitation blend method have longer CS whiskers in average, which could absorb more impact energy and improve toughness of composites [24]. Therefore, the impact strength of whisker composites prepared by coprecipitation method is higher than that of both the pure PCL and the composites produced by melting method.

4. Conclusions

PCL/CS whisker composites have been prepared by both the melt blending and coprecipitation methods. Our experiment results have justified that the melting method benefits the crystallization of PCL and the flexural properties, but deteriorates the toughness of the PCL/CS whisker composites. Coprecipitation method harms the crystallization of the composites, but can improve mechanical properties. The thermal properties of PCL for composites are nearly unaffected by the presence of whiskers for two methods. For composites prepared by coprecipitation method, the spherulite size of the PCL is reduced by CS whisker addition, and the flexural and impact strength of composites with 15 wt% CS whisker are highest. Investigation shows that longer whiskers benefit the mechanical property of the composites. It is worth to mention that the biocompatibility of composites is important for the bone

repair, and the biocompatibility for the composite system is under our investigation.

Acknowledgements

This research was supported by National Natural Science Foundation of China (Grant No.50732003, 50803018 and U0834003) and National Science and Technology Support Programme of China (Grant No. 2006BAI16B06).

Reference

[1] Khatiwala V. K., Shekhar N., Aggarwal S., Mandal U. K.: Biodegradation of poly(ε-caprolactone) (PCL) film by alcaligenes faecalis. Journal of Polymers and the Environment, **16**, 61–67 (2008).
DOI: 10.1007/s10924-008-0104-9

[2] Lei Y., Rai B., Ho K. H., Teoh S. H.: *In vitro* degradation of novel bioactive polycaprolactone–20% tricalcium phosphate composite scaffolds for bone engineering. Materials Science and Engineering: C, **27**, 293–298 (2007).
DOI: 10.1016/j.msec.2006.05.006

[3] Rai B., Teoh S. H., Ho K. H.: An in vitro evaluation of PCL–TCP composites as delivery systems for platelet-rich plasma. Journal of Controlled Release, **107**, 330–342 (2005).
DOI: 10.1016/j.jconrel.2005.07.002

[4] Huang Y., Liu H., He P., Yuan L., Xiong H., Xu Y. M., Yu Y.: Nonisothermal crystallization kinetics of modified bamboo fiber/PCL composites. Journal of Applied Polymer Science, **116**, 2119–2125 (2010).
DOI: 10.1002/app.31772

[5] Wang Y., Shi X., Ren L., Yao Y., Zhang F., Wang D-A.: Poly(lactide-co-glycolide)/titania composite microsphere-sintered scaffolds for bone tissue engineering applications. Journal of Biomedical Materials Research Part B: Applied Biomaterials, **93**, 84–92 (2010).
DOI: 10.1002/jbm.b.31561

[6] Dunn A. S., Campbell P. G., Marra K. G.: The influence of polymer blend composition on the degradation of polymer/hydroxyapatite biomaterials. Journal of Materials Science: Materials in Medicine, **12**, 673–677 (2001).
DOI: 10.1023/A:1011204106373

[7] Wong S-C., Baji A.: Fracture strength and adhesive strength of hydroxyapatite-filled polycaprolactone. Journal of Material Science: Materials in Medicine, **19**, 929–936 (2008).
DOI: 10.1007/s10856-007-3016-7

[8] Li L. H., Kommareddy K. P., Pilz C., Zhou C. R., Fratz P., Manjubala I.: In vitro bioactivity of bioresorbable porous polymeric scaffolds incorporating hydroxyapatite microspheres. Acta Biomaterialia, **6**, 2525–2531 (2010).
DOI: 10.1016/j.actbio.2009.03.028

[9] Lebourg M., Suay Antón J., Ribelles J. L. G.: Hybrid structure in PCL-HAp scaffold resulting from biomimetic apatite growth. Journal of Materials Science: Materials in Medicine, **21**, 33–44 (2010).
DOI: 10.1007/s10856-009-3838-6

[10] Huang J., Lin Y. W., Fu X. W., Best S. M., Brooks R. A., Rushton N., Bonfield W.: Development of nano-sized hydroxyapatite reinforced composites for tissue engineering scaffolds. Journal of Materials Science: Materials in Medicine, **18**, 2151–2157 (2007).
DOI: 10.1007/s10856-007-3201-8

[11] Yefang Z., Hutmacher D. W., Varawan S-L., Meng L. T.: Comparison of human alveolar osteoblasts cultured on polymer-ceramic composite scaffolds and tissue culture plates. International Journal of Oral and Maxillofacial Surgery, **36**, 137–145 (2007).
DOI: 10.1016/j.ijom.2006.08.012

[12] Zhang Z-Y., Teoh S. H., Chong W-S., Foo T-T., Chong Y-C., Choolani M., Chan J.: A biaxial rotating bioreactor for the culture of fetal mesenchymal stem cells for bone tissue engineering. Biomaterials, **30**, 2694–2704 (2009).
DOI: 10.1016/j.biomaterials.2009.01.028

[13] Abbah S. A., Lam C. X. L., Hutmacher D. W., Goh J. C. H., Wong H-K.: Biological performance of a polycaprolactone-based scaffold used as fusion cage device in a large animal model of spinal reconstructive surgery. Biomaterials, **30**, 5086–5093 (2009).
DOI: 10.1016/j.biomaterials.2009.05.067

[14] Su R., Wang K., Ning N., Chen F., Zhang Q., Wang C., Fu Q., Na B.: Orientation in high-density polyethylene/inorganic whisker composite fibers as studied via polarized Fourier transform infrared spectroscopy. Composites Science and Technology, **70**, 685–691 (2010).
DOI: 10.1016/j.compscitech.2010.01.001

[15] Cao Y., Feng J., Wu P.: Simultaneously improving the toughness, flexural modulus and thermal performance of isotactic polypropylene by α-β crystalline transition and inorganic whisker reinforcement. Polymer Engineering and Science, **50**, 222–231 (2010).
DOI: 10.1002/pen.21521

[16] Converse G. L., Conrad T. L., Roeder R. K.: Mechanical properties of hydroxyapatite whisker reinforced polyetherketoneketone composite scaffolds. Journal of the Mechanical Behavior of Biomedical Materials, **2**, 627–635 (2009).
DOI: 10.1016/j.jmbbm.2009.07.002

[17] Thomas M. V., Puleo D. A.: Calcium sulfate: Properties and clinical applications. Journal of Biomedical Material Research Part B: Applied Biomaterials, **88**, 597–610 (2009).
DOI: 10.1002/jbm.b.31269

[18] La Gatta A., De Rosa A., Laurienzo P., Malinconico M., De Rosa M., Schiraldi C.: A novel injectable poly (ε-caprolactone)/calcium sulfate system for bone regeneration: Synthesis and characterization. Macromolecular Bioscience, **5**, 1108–1117 (2005).
DOI: 10.1002/mabi.200500114

[19] Gao C., Gao J., You X., Huo S., Li X., Zhang Y., Zhang W.: Fabrication of calcium sulfate/PLLA composites for bone repair. Journal of Biomedical Material Research Part A, **73**, 244–253 (2005).
DOI: 10.1002/jbm.a.30283

[20] Ten E., Turtle J., Bahr D., Jiang L., Wolcott M.: Thermal and mechanical properties of poly(3-hydroxybutyrate-*co*-3-hydroxyvalerate)/cellulose nanowhiskers composites. Polymer, **51**, 2652–2660 (2010).
DOI: 10.1016/j.polymer.2010.04.007

[21] Liu L., Kang M-Q., Zhang Z-X., Wang X-K.: The mechanical properties of polyurethane elastomer reinforced and toughened by $CaSO_4$-whisker. Journal of Wuhan University of Technology-Materials Science Edition, **17**, 50–53 (2002).
DOI: 10.1007/BF02838539

[22] Zhou J., Tang J., Meng H., Yu J.: Study on PP/calcium sulfate whisker composite. Engineering Plastics Application, **36**, 19–22 (2008).

[23] Zhu Z., Xu L., Chen G., Li Y.: Optimization on tribological properties of aramid fibre and $CaSO_4$ whisker reinforced non-metallic friction material with analytic hierarchy process and preference ranking organization method for enrichment evaluations. Materials and Design, **31**, 551–555 (2010).
DOI: 10.1016/j.matdes.2009.07.015

[24] Thomason J. L.: The influence of fibre length, diameter and concentration on the strength and strain to failure of glass fibre-reinforced polyamide 6,6. Composites Part A: Applied Science and Manufacturing, **40**, 114–124 (2009).
DOI: 10.1016/j.compositesa.2008.07.002

[25] Chen E-C., Wu T-M.: Isothermal crystallization kinetics and thermal behavior of poly(ε-caprolactone)/multi-walled carbon nanotube composites. Polymer Degradation and Stability, **92**, 1009–1015 (2007).
DOI: 10.1016/j.polymdegradstab.2007.02.019

[26] Yang D., Yang Z., Li X., Di L-Z., Zhao H.: A study of hydroxyapatite/calcium sulphate bioceramics. Ceramics International, **31**, 1021–1023 (2005).
DOI: 10.1016/j.ceramint.2004.10.016

[27] Berlanga R., Suñol J. J., Saurina J.: Polymer crystallization: A DSC approach to building the T-CR-T diagram. Macromolecular Theory and Simulations, **17**, 103–108 (2008).
DOI: 10.1002/MATS.200700063

[28] Hua L., Kai W. H., Inoue Y.: Crystallization behavior of poly(ε-caprolactone)/graphite oxide composites. Journal of Applied Polymer Science, **106**, 4225–4232 (2007).
DOI: 10.1002/app.26976

[29] Li X., Cao Y., Du Q., Yin Y., Tu D.: Charge distribution and crystalline structure in polyethylene nucleated with sorbitol. Journal of Applied Polymer Science, **82**, 611–619 (2001).
DOI: 10.1002/app.1889

[30] Vanherpe L., Moelans N., Blanpain B., Vandewalle S.: Pinning effect of spheroid second-phase particles on grain growth studied by three-dimensional phase-field simulations. Computational Materials Science, **49**, 340–350 (2010).
DOI: 10.1016/j.commatsci.2010.05.020

[31] Jiang S., Ji X., An L., Jiang B.: Confined crystallization behavior of PCL in organic-inorganic hybrid system. Acta Polymerica Sinica, **4**, 452–456 (2000).

[32] Nojima S., Nakano H., Takahashi Y., Ashida T.: Crystallization of block copolymers: 3. Crystallization behaviour of an ε-caprolactone-butadiene diblock copolymer. Polymer, **35**, 3479–3486 (1994).
DOI: 10.1016/0032-3861(94)90912-1

[33] Lepoittevin B., Devalckenaere M., Pantoustier N., Alexandre M., Kudies D., Calberg C., Jérôme R., Dubois P.: Poly(ε-caprolactone)/clay nanocomposites prepared by melt intercalation: Mechanical, thermal and rheological properties. Polymer, **43**, 4017–4023 (2002).
DOI: 10.1016/S0032-3861(02)00229-X

[34] Peng H., Han Y., Liu T., Tjiu W. C., He C.: Morphology and thermal degradation behavior of highly exfoliated CoAl-layered double hydroxide/polycaprolactone nanocomposites prepared by simple solution intercalation. Thermochimica Acta, **502**, 1– 7 (2010).
DOI: 10.1016/j.tca.2010.01.009

[35] Nakamura S., Hata M., Yoshioka T., Takeuchi H., Yamamoto T., Kishida Y., Arima T.: Bone connecting device and method of manufacturing the same. U.S. Patent 6905501B2, USA (2005).